Synthesis and Characterization of Kx:p-Terphenyl Materials for Superconductivity and the Ultrafast Dynamics of the Photocycloaddition of an Orthocyclophane

by

ANDREW JOSEPH CHOMAS

B.S., Case Western Reserve University, 2012

A thesis submitted to the

Faculty of the Graduate School of the

University of Colorado in partial fulfillment of

Doctor of Philosophy

Department of Chemistry

2024

Committee Members:

Niels H. Damrauer

Daniel S. Dessau

Jihye Park

Oana R. Luca

Sean E. Shaheen

Chomas, Andrew Joseph (Ph.D., Chemistry)

Synthesis and Characterization of Kx:p-Terphenyl Materials for Superconductivity and the Ultrafast Dynamics of the Photocycloaddition of an Orthocyclophane

Thesis directed by Professor Niels Damrauer

Alkali metal doped polycyclic aromatic hydrocarbons (PAH) are an exciting material platform for organic based superconductors with relatively high critical temperatures. In the case of potassium doped *para*-terphenyl, some studies have reported signs of superconducting transitions as high as120 K. However, these studies are controversial because of issues with reproducibility. Additionally, the extreme air sensitivity of K_x:*p*-terphenyl makes it challenging to synthesize and characterize with conventional methods. This thesis presents a new method of solution phase deposition of alkali doped PAHs and apply it to synthesize K_x:*p*-terphenyl materials for superconductivity using liquid ammonia as a solvent. It will explore the structure of these materials with Fourier transform infrared spectroscopy and x-ray diffraction, which demonstrate charge transfer from potassium to *p*-terphenyl coincident with the formation of new material phases. It will also show initial conductivity measurements that have an atypical linear temperature dependence. Reproducibility of the synthesis will be discussed as well as the future directions of this work. Additionally, it will also explore the ultrafast dynamics of a [2 + 2] photocycloaddition. When exciting to the first excited state, the cycloaddition occurs with the typical mechanism with an excimer intermediate.

However, when exciting to the second singlet excited state, the cycloaddition happens on a subpicosecond timescale with a process that resembles singlet fission.

In memory of Josef Michl

"Only in silence the word, only in dark the light, only in dying life:

bright the hawk's flight on the empty sky."

-Ursula K. Le Guin

Acknowledgements

Josef Michl

Niels Damrauer

Dan Dessau

Sean Shaheen

Jihye Park

Oana Luca

Eric Buchanan

Igor Roncevik

Saghar Razaie

Santosh Shelar

Jacek Pecyne

Paul Dron

Thomas Magnera

Hope Whitelock

Spencer Hall

Nicholas Weadock

Alex Fix

Bryan Berggren

Ethan Miller

Alexander Gilligan

Nicholas Pompetti

Ryan Dill

Izzy Lamb

Jenny Lin

Sam Shepard

Orion Pierce

Raythe Owens

Arindam Sau

Kajal

Roberto Cardenas

Casey Zigman

Justin Griffith

Peipei Hao

Aritra Mazumder

Zack Sierzega

Thomas Stewart

Robert Smith

Alex Ball

Eberhard Riedle

Roland Wickland

Matthias Block

Henrieta Volfova

Emanuel Wittmann

Bastian Baudisch

Qi Hu

Richard Ciesielski

Molly Larsen

Jacqueline Richardson

Don David

Yehor Novikov

Paul Thompson

Allan Maple Oliveira

Kerry Hill

Dale and Tamela Chomas

CONTENTS

TABLES

Table

FIGURES

Figure

SCHEMES

Scheme

CHAPTER 1

Introduction

1.1 Conduction in Metals

The conductivity, σ, of a material is the proportionality constant that relates the current density j in a material induced by an electric field E

$$j = \sigma E \tag{1}$$

and is typically in units Siemens (S) per cm and is an intrinsic quantity. It is the inverse of the resistivity, ρ, typically in units of Ohms (Ω) cm. By applying a current through a material and measuring the voltage drop, the resistance R can be calculated using Ohm's law. This measured resistance can be converted to resistivity by multiplying it by the cross-sectional area A of the material and dividing by the length l between the voltage measurement.

$$\rho = R\frac{A}{l} \tag{2}$$

The current density in metals depends on the number density, N, of free electrons and the average velocity, v, of the electrons, shown in Equation 3,

$$j = Nve \tag{3}$$

where e is the fundamental charge of an electron. The electron mobility, μ, is the proportionality constant between velocity of an electron with an applied electric field

$$v = \mu E \tag{4}$$

and describes the drag felt by the electron from collisions with the atoms in the lattice. This lets us express the conductivity in terms of mobility and number density

$$\sigma = N\mu e \tag{5}$$

This means the effects of electron-phonon scattering from the lattice is contained in the mobility, and the statistical effects from the population of carriers is contained in the carrier number density.[1]

The conductivity of metals increases (decreasing resistivity) with decreasing temperature. For simple metals at high temperature, the conductivity is proportional T^{-1}, while at low temperatures it is proportional to T^{-5}.[2] The conductivity of semiconductors and insulators decreases (increasing resistivity) with decreasing temperature.

1.2 Conduction in Semiconductors

In contrast to metals, semiconductors have a much lower conductivity at room temperature and their conductivity decreases with temperature. The conductivity of an amorphous solid can be modelled using variable-range hopping.[3] In this model,

$$\sigma(T) = \sigma_0 exp\left[-\left(\frac{T_0}{T}\right)^{\alpha}\right] \tag{6}$$

where σ_0 and T_0 are parameters and α is related to the dimensionality D of the charge carrier hopping

$$\alpha = \frac{1}{1+D} \tag{7}$$

Therefore, $\alpha = 1/2$ indicates carrier hopping in one dimension, $\alpha = 1/3$ indicates carrier hopping in two dimensions, and $\alpha = 1/4$ indicates carrier hopping in three dimensions.[4] Thus, plots of $-\ln(\sigma)$ vs $T^{-\alpha}$ for a material will be linear for the dimensions that hopping occurs in.

The conductivity of a material may also be limited by inaccessibility of the conduction band at low temperatures. This manifests as a thermal barrier in the conductivity that can be expressed with an Arrhenius equation of the conductivity[5]

$$\sigma(T) = \sigma_0 exp\left[-\left(\frac{E_A}{kT}\right)\right] \tag{8}$$

where E_A is the activation energy of conduction and k is the Boltzmann constant. Therefore, plots of $-\ln(\sigma)$ vs $1/T$ will be linear with a slope of E_A.

1.3 Superconductivity

A superconductor is a material that at a critical temperature T_c, undergoes phase transition to a superconducting state where the resistivity drops to exactly zero, meaning the conductivity becomes infinite. This means that the electric field inside the superconductor is zero and that currents can persist indefinitely.[6] Superconductors are also perfectly diamagnetic. In the superconducting state, they will exclude weak magnetic fields. The Maxwell equation

$$\nabla \times E = \frac{\partial B}{\partial t} \tag{9}$$

relates the electric field E with the magnetic induction B. If E is zero in the superconducting state, this means that the change in the B field inside the material is zero as well, and an applied B field will be excluded from the superconductor.

Additionally, if a B field is applied to the normal state of the material, and the material is brought below T_c into the superconducting state, the applied field will be expelled by the material. This is called the Meissner effect, and is unique to the superconducting state.[7]

However, the superconducting state will be lost when a critical magnetic field is reached. In Type I superconductors, the magnetization M = -H, the applied magnetic field, in the superconducting state. When the critical magnetic field is reached the superconducting state is lost immediately. Type II superconductors have two critical fields, H_{c1} and H_{c2}. Below H_{c1}, the superconductor obeys the Meissner effect and M = -H. Between H_{c1} and H_{c2}, the superconductor still has zero resistivity, however the magnetization no longer fully follows the Meissner effect and magnetic flux density increases in the material. Above H_{c2} the material returns to the normal state.[8]

Mercury was the first superconductor discovered with a T_c of 4.1 K in 1911.[9] Many other elemental metals are superconductors with critical temperatures in the single digit Kelvin range, and several alloys with the highest critical temperatures ~ 20 K. In the late 1980s high temperature copper oxide superconductors were discovered.[10] Now the highest T_c of any superconductor at atmospheric pressure is 135 K, above the boiling point of liquid nitrogen. Numerous technologies utilize the zero resistivity, including magnetic resonance spectroscopy and imaging.[6]

1.4 Organic Superconductors

The possibility of superconductivity in organic based materials has been explored since at least the 1960s.[11] Superconductivity in organic materials was first observed in a material of this type in di-(tetramethyltetraselenafulvene)-hexafluorophosphate, $(TMTSF)_2PF_6$, with critical temperatures around 1 K and pressures of 12 kbar.[12] Here the TMTSF units are stacked in quasi one-dimensional arrays. This created interest in exploring the possibility of superconductivity in other conducting organic materials.

In 1992, superconductivity was observed in potassium doped carbon fullerene, K_3C_{60}.[13] Here, the potassium atoms intercalate between the spherical C_{60} molecules which cause the fullerenes to pack less tightly. The potassium atoms also reduce the C_{60}, injecting electrons into the conduction band.[14] This causes the conduction band to become partially filled and the material to become conducting with a superconducting transition at 19 K. Continued doping with potassium changes the band structure from a face centered cubic phase of K_3C_{60} to a body centered tetragonal phase of K_4C_{60}, then body centered cubic phase of K_6C_{60}. The change in symmetry returns the material to an insulating state. This phenomenon has also been observed when doping with other alkali metals. The highest critical temperature was observed with Rb_2CsC_{60} at 30 K. Superconductivity has since been observed in alkali and alkali earth metal doped graphite with a T_c of 11.5 K.[15] In 2010, superconductivity of potassium doped picene with critical temperatures between 6.5 K and 18 K, depending on the potassium doping between $K_{2.6}$ and

$K_{3.3}$.[16] This motivated investigating the superconducting properties of other small aromatic hydrocarbons.

1.5 *p*-Terphenyl Superconductivity

In 2017, it was reported that K_3:*p*-terphenyl was superconducting with a critical temperature of 120 K.[17] Figure 1.1 A shows the molecular structure of p-terphenyl. This material was grown by sealing potassium metal and neat *p*-terphenyl in a 3 to 1 molar ratio in a glass tube under vacuum and heating at 500 K for 24 to 168 hours, producing a black material. Magnetic susceptibility measurements showed a steep decrease in the susceptibility at 120 K. These results were controversial since papers from the same group reported lower critical temperatures.[18,19] Additionally, the conductivities and diamagnetism did not unambiguously show a superconducting state, and these papers were never published with peer-review. However, angle resolved photo-electron spectroscopy (ARPES) performed on *p*-terphenyl crystals surface doped with potassium metal found a low temperature gap in the fermi level that persists to 120 K.[20] The existence of this gap suggests the formation of electron pairs in the superconducting state.

Zhong *et al*[21] performed density functional theory calculations to predict the crystal structure of K_x:*p*-terphenyl with multiple doping levels x = 1, 1.5, 2, 2.5, and 3. Neat p-terphenyl has a herringbone structure with the center phenyl ring twisted out of plane. They found that as the doping level increases, the crystal structure distorts to incorporate the potassium atoms between the planes of terphenyl

molecules. At the x = 3 doping, the terphenyl molecules flatten and rotate from a herringbone structure to a two-dimensional layered lattice, shown in Figure 1.1 B. They also found that increasing doping increases charge transfer between the potassium atoms and the *p*-terphenyl, which would increase the conductivity of the material, with x = 2.5 and higher yielding a metallic material, with x = 2 and lower being semiconducting. Additionally, they found that of these phases, x = 2.5 is thermodynamically the most stable. Similar calculations were also performed by Yan *et al*,[22] who also found that K_2:*p*-terphenyl phase is also semiconducting.

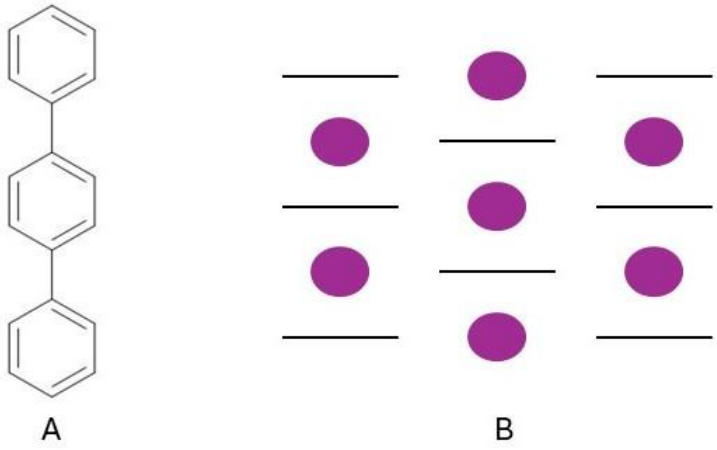

Figure 1.1: A) Structure of *p*-terphenyl. B) Proposed crystal structure of K_3:*p*-terphenyl. Potassium atoms are violet, black lines are *p*-terphenyl molecules looking along the long axis.

A few other experimental papers have reported spectroscopic and physical properties of K_x:*p*-terphenyl.[23-25] They all prepare K_x:*p*-terphenyl by mixing known quantities of potassium and *p*-terphenyl and annealing under vacuum and annealing at high temperatures. Carrera *et al*[23] and Pinto *et al*[24] report electrical transport measurements that, while some samples of K_x:*p*-terphenyl have metallic

conductivity, they do not show any superconducting transitions. That said, neither were able to produce samples above x=2 levels of doping. Carrera *et al* also reports the potential polymerization of *p*-terphenyl when reacting with potassium at high temperatures. To our knowledge, a solved experimental crystal structure has never been reported for any doping of this material.

1.6 Cycloadditions

A cycloaddition is a concerted reaction where two π bonds are converted to two σ bonds to form a ring.[26] A [m + n] cycloaddition is when a molecule with m pi electrons reacts with another molecule with n pi electrons to form the ring. For instance, a [2 + 2] cycloaddition reaction is between a molecule with 2 π electrons reacting with second molecule with 2 π electrons. The classic example of a [2 + 2] cycloaddition is the dimerization of ethylene to cyclobutane, shown in Scheme 1.1.

Scheme 1.1: [2 + 2] cycloaddition of ethylene to cyclobutene.

The Woodward-Hoffmann rules provide a valuable method for understanding the allowedness and stereochemistry of cycloadditions.[27] From these rules, it is found that cycloadditions where m + n = 4q +2 are thermally allowed and photochemically disallowed, while m + n = 4q are photochemically allowed and thermally disallowed.[28] Therefore, [2 + 2] cycloadditions are formally only allowed from photoexcited states.

To illustrate this, Figure 1.2 A shows the molecular orbital correlation diagram of a [2 + 2] photocycloaddition,[29] with the relevant orbitals shown in Figure

1.2 B. Woodward and Hoffmann showed that the transformation of π orbitals to σ orbitals in a concerted reaction conserves orbital symmetry. Therefore, orbitals with a specific symmetry will retain that symmetry over the reaction progress. In the ground state of ethylene, the two π orbitals are filled initially. After cycloaddition, this would result in a product with the SS σ and AS σ* orbitals filled. Since this is a high energy state, the reaction is not thermally allowed. However, if one of the ethylene molecules is photoexcited, such that the SA π* orbital is filled, the reaction results in a ground state product, and is thus photochemically allowed.

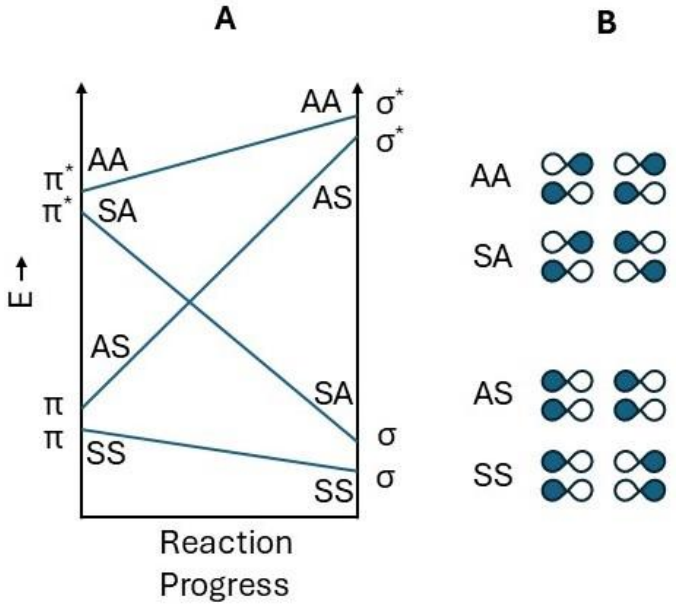

Figure 1.2: A) Molecular Orbital correlation diagram for a [2 + 2] photocycloaddition. B) The molecular orbitals of each symmetry type.

This process is illustrated more clearly in the state correlation diagram shown in Figure 1.3. The dotted lines show the correlation between the ground state (G) and the doubly excited state (D). In a potential energy surface, this crossing is

avoided and creates a barrier in the G surface and a conical intersection between all three surfaces called the pericyclic minimum.[29]

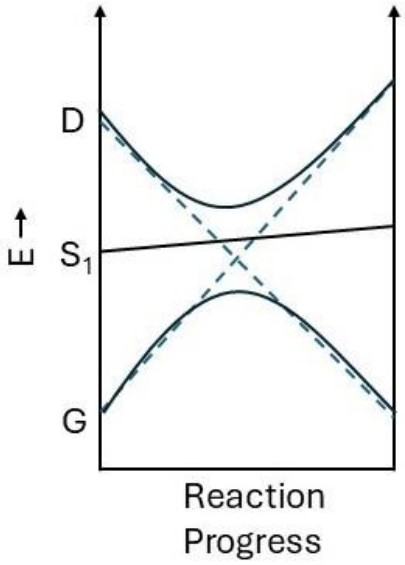

Figure 1.3: State correlation diagram of ethylene cycloaddition to cyclobutane. State G is the ground state, S_1 is the first excited state of ethylene, and D is the doubly excited state of ethylene.

1.7 Transient Absorption Spectroscopy

Femtosecond transient absorption (TA) spectroscopy is a powerful tool for studying the kinetics of light driven processes. It is a pump-probe spectroscopy, where a sample is first pumped by an ultrafast laser pulse to excite the sample resonantly into an electronic excited state and initiate a photochemical process. After a specified time, a broadband probe pulse probes the sample and measures the spectrum of the probe. A schematic of this is shown in Figure 1.4. The TA signal is generated by dividing the probe spectrum of the sample after excitation with the pump with the probe spectrum without excitation by the pump, and then taking the negative logarithm. This results in a unitless difference spectrum of optical density

that measures the change in the sample spectrum after excitation by the pump. Dynamics are measured by systematically increasing the time between pump and probe pulses and measuring spectra at each time step.

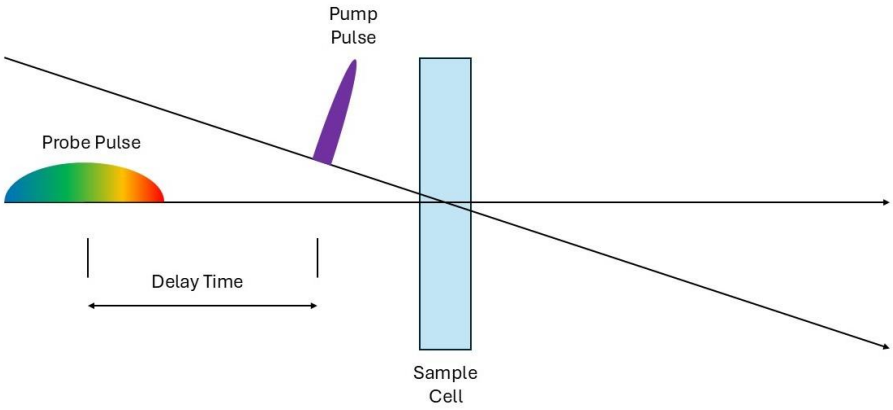

Figure 1.4: Schematic of the pump and probe pulses passing through a sample cell, with a time delay between pulses.

The sign of the change in optical density has different physical meanings. A negative ΔOD means that less probe light is absorbed by the sample after excitation by the pump. This typically measures the decrease of absorbance of the ground state, called the ground state bleach, and shows the kinetics of the excited state population returns to the ground state. Positive ΔOD means that more light is absorbed by the sample after excitation of the pump. This typically indicates that there are new, excited state absorption features after excitation. The spectrum of these features can indicate the nature of the state the excited population is in, and the kinetics of these features can indicate the timescales that excited state intermediates form.

1.8 Global Analysis

Well separated spectral bands in TA measurements can often be fit to exponential decays at single wavelengths. However, when bands overlap, a single wavelength fit can be inadequate to describe the observed kinetics. This is particularly challenging when two bands of different signs overlap. In such situations, global analysis can be used to simultaneously fit multiple wavelengths of the spectrum.[30] This is done by creating matrix *A*, where columns are spectra at specific time delays, and rows are the kinetic trace at each wavelength. This matrix can be written as

$$A = FD^T \tag{10}$$

where *D* is a matrix of elements $\exp(-t_i/\tau_i)$. Each column is a specific time delay t_i in the experiment, and τ_i is the fit parameter. D^T is the transpose of *D*. *F* is a matrix of $\underline{i}$ rows where each row is spectrum called a decay associated difference spectrum (DADS). *F* can be solved by multiplying each side of equation 1 by *D* and inverting D^TD.

$$F_\tau = AD_\tau(D_\tau^T D_\tau)^{-1} \tag{11}$$

A_τ can then be reconstructed from F_τ and $D_\tau{}^T$ as in Equation 10.

The global fit is performed by choosing i parameters of τ. These will generate i DADS, with each spectrum corresponding to the TA spectrum of the species that exponentially decay with time constant τ_i. A least squares fitting is then performed on matrix *A*, containing the experimental TA spectrum, and A_τ, the generated TA spectrum from F_τ and D_τ. Once the fit has converged, each DADS and time constant can be interpreted in terms of the molecular species that are present.

The above method can be used to generate a parallel kinetic model of the TA experiment. That is, starting at the initial time, the model shows the spectral components that decay simultaneously with their corresponding time constant. Sometimes it is useful to perform global analysis with a sequential kinetic model. This generates evolution associated difference spectra (EADS), which corresponds to the spectra of species that sequentially form and decay with their corresponding time constants. The fit procedure is similar to what is described above, with minor changes in how the exponential functions are arranged in the D_τ matrix.[31]

References

1. Castellan, G. W. *Physical Chemistry,* 3rd Ed.; Addison-Wesley Publishing Company: Reading, MA, 1983.

2. Madelung, O. *Introduction to Solid-State Theory*, Cardona, M.; Fulde, P.; Queisser, H.-J. Eds.; Springer Series in Solid-State Sciences; Springer-Verlag: New York, 1981.

3. Hill, R. M. Variable-Range Hopping. *Phys. Stat. Sol.* **1976,** *34,* 601-613.

4. Nardes, A. M.; Kemerink, M.; Janssen, R. A. J.; Anisotropic Hopping Conduction in Spin-Coated PEDOT:PSS Thin Films. *Phys. Rev. B* **2007,** *76,* 085208.

5. Lin, T. T.; Young, S. L.; Kung, C. Y.; Chen, H. Z.; Kao, M. C.; Chang, M. C.; Ou, C. R. Variable-Range Hopping and Thermal Activation Conduction of Y-Doped ZnO Nanocrystalline Films. *IEEE TNANO.* **2014,** *13,* 425-430.

6. Annett, J. F. *Superconductivity, Superfluids, and Condensates*, Oxford Master Series in Condensed Matter Physics; Oxford University Press: New York, 2004.

7. Tinkham, M. *Introduction to Superconductivity,* 2nd Ed.; International Series in Pure and Applied Physics; McGraw-Hill, Inc.: New York, 1996.

8. Kittel, C. *Introduction to Solid State Physics*, 5th Ed. John Wiley & Sons, Inc.: New York, 1976.

9. Onnes, H. K. Further Experiments with Liquid Helium C. On the Change of Electric Resistance of Pure Metals at Very Low Temperatures etc. IV. The Resistance of Pure Mercury at Helium Temperatures. *Proceedings,* **1911,** *13,* 1274-1276.

10. Bednorz, J. G.; Muller, K. A. Possible High T_c Superconductivity in the Ba-La-Cu-O System. *Z. Phys. B – Condensed Matter* **1986,** *64,* 189-193.

11. Little, W. A. Possibility of Synthesizing an Organic Superconductor. *Phys. Rev.* **1964,** *134,* A1416-A1424.

12. Jerome, D.; Mazaud, A.; Ribault, M. Superconductivity in a Synthetic Organic Conductor $(TMTSF)_2PF_6$. *J. Physique – LETTRES* **1980,** *41,* L-95-L-98.

13. Xiang, X.-D.; Hou, J. G.; Briceno, G.; Vareka, W. A.; Mostovoy, R.; Zettl, A.; Crespi, V. H.; Cohen, M. L. Synthesis and Electrical Transport of Sing Crystal K_3C_{60}. *Science* **1992,** *256,* 1190-1191.

14. Hebard, A. F. Superconductivity in Doped Fullerenes. *Phys. Today* **1992,** *45,* 26-32.

15. Emery, N.; Herold, C.; d'Astuto, M.; Garcia, V.;Bellin, Ch.; Mareche, J. F.; Lagrange, P.; Loupias, G. Superconductivity in Bulk CaC_6. *Phys. Rev. Lett.* **2005,** *95,* 087003.

16. Mitsuhashi, R.; Suzuki, Y.; Yamanari, Y.; Mitamura, H.; Kambe, T.; Ikeda, N.; Okamoto, H.; Fujiwara, A.; Yamaji, M.; Kawasaki, N.; Maniwa, Y.; Kubozono, Y. Superconductivity in Alkali-Metal-Doped Picene. *Nat. Lett.* **2010,** *464,* 76-79.

17. Wang, R.-S.; Gao, Y.; Huang, Z.-B.; Chen, X.-J. Superconductivity Above 120 Kelvin in a Chain Link Molecule. arXiv:1703.06641, **2017.**

18. Wang, R.-S.; Gao, Y.; Huang, Z.-B.; Chen, X.-J. Superconductivity in *p*-Terphenyl. arXiv:1703.05803, **2017.**

19. Wang, R.-S.; Gao, Y.; Huang, Z.-B.; Chen, X.-J. Superconductivity at 43 K in a Single C-C Bond Linked Terphenyl. arXiv:1703.05804, **2017.**

20. Li, H.; Zhou, X.; Parham, S.; Nummy, T.; Griffith, J.; Gordon, K. N.; Chronister, E. L.; Dessau, D. S. Spectroscopic Evidence of Low-Energy Gaps Persisting Up To 120 K in Surface-Doped *p*-Terphenyl Crystals. *Phys. Rev. B* **2019,** *100,* 064511.

21. Zhong, G.-H.; Wang, X.-H.; Wang, R.-S.; Han, J.-X.; Zhang, C.; Chen, X.-J.; Lin, H.-Q. Structural and Bonding Characteristics of Potassium-Doped *p*-Terphenyl Superconductors. *J. Phys. Chem. C* **2018,** *122,* 3801-3808.

22. Yan, X.-W.; Huang, Z.; Gao, M.; Zhang, C. Stable Structural Phase of Potassium-Doped *p*-Terphenyl and Its Semiconducting State. *J. Phys. Chem. C* **2018,** *122,* 27648-27655.

23. Carrera, M.; McDonald, J. L.; Untiedt, C.; Garcia-Hernandez, F. M.; Verges, J. A.; Guijarra, A. Characterization of Main Phase in K_x*p*-Terphenyl and Its Largest Congener $K_x$poly(*p*-phenylene): A Report of Their Magnetic and Electric Properties. *J. Chem. Phys. C* **2019,** *123,* 5264-5272.

24. Pinto, N.; Di Nicola, C.; Trapananti, A.; Minicucci, M.; Di Cicco, A.; Marcelli, A.; Bianconi, A.; Marchetti, F.; Pettinari, C.; Perali, A. Potassium-Doped Para-Terphenyl: Structure, Electrical Transport Properties and Possible Signatures of a Superconducting Transition. *Condens. Matter* **2020,** *5,* 78.

25. He, Q.; Marsik, P.; Le Mardele, F.; Xu, B.; Sharma, M.; Pinto, N.; Perali, A.; Di Nicola, C.; Pettinari, C.; Baeriswyl, D.; Bernhard, C. Infrared Ellipsometry Study of the Charge Dynamics in K_3*p*-Terphenyl. *Phys. Rev. B* **2023,** *107,* 094520.

26. Anslyn, E. V.; Dougherty, D. A. *Modern Physical Organic Chemistry,* University Science Books: Sausalito, CA, 2006.

27. Hoffmann, R.; Woodward, R. B. The Conservation of Orbital Symmetry. *Acc. Chem Res.* **1968,** *1,* 17-22.

28. Vollmer, J. J.; Servis, K. L. Woodward-Hoffmann Rules: Cycloaddition Reactions. *J. Chem. Ed.* **1970,** *47,* 491-500.

29. Michl, J.; Bonacic-Koutecky, V. *Electronic Aspects of Organic Photochemistry;* John Wiley & Sons, Inc.: New York, 1990.

30. Fita, P.; Luzina, E.; Dziembowska, T.; Radzewicz, Cz.; Grabowska, A. Chemistry, Photophysics, and Ultrafast Kinetics of Two Structurally Related Schiff Bases Containing the Naphthalene and Quinoline Ring. *J. Chem. Phys.* **2006,** *125,* 184508.

31. Snellenburg, J. J.; Laptenok, S. P.; Seger, R.; Mullen, K. M.; van Stokkum, I. H. M. Glotoran: A Java-Based Graphical User Interface for the R Package TIMP. *J. Stat. Soft.* **2012,** *49,* 1-22.

CHAPTER 2

K_2:*p*-Terphenyl Using Tetrahydrofuran

2.1 Introduction

This chapter assesses the potential of solution phase synthesis of K_x:*p*-terphenyl films. We follow the work of Sakamoto *et al*[1] to prepare anions of *p*-terphenyl by reduction with alkali metals in tetrahydrofuran (THF), shown in Scheme 2.1.

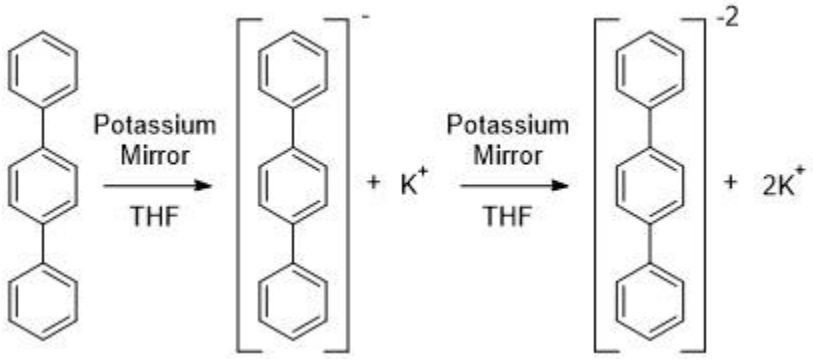

Scheme 2.1: *p*-Terphenyl and it's reduction in THF by potassium.

This procedure was first developed as a general method to prepare and study the anions of aromatic hydrocarbons in solution with spectroscopic methods. An aromatic hydrocarbon, in this case *p*-terphenyl, is dissolved in an ethereal solvent such as THF, and the solution is then passed over an alkali metal mirror. The metal slowly reduces the *p*-terphenyl, first to the anion and then the dianion.

Here, we apply this method to prepare solutions of *p*-terphenyl anions with potassium counter ions. We then deposit films of this material and characterize it with UV-Visible spectroscopy. It provides valuable insight into other methods of deposition with other solvent systems.

2.2 Materials and Methods

2.2.1 General

Unless otherwise stated, reagents and solvents were obtained from Sigma Aldrich and used as received. Potassium (ThermoFisher Scientific, 99.95% metals basis) was received sealed in an ampule that was opened in a glovebox. *p*-Terphenyl was from Alfa Aesar (>99% purity). UV-Vis spectroscopy was undertaken using a Varian Cary 5000 in dual beam mode. When possible, blank spectra of either empty cuvettes or those filled with solvent were used for background subtraction, otherwise the cell in the second beam path was left empty. The custom apparatus and reactor were made in the CIRES Integrated Instrument Development Facility by Yehor Novikov. Other custom glassware and adapters were made by the author.

2.2.2 Potassium Capillary Tubes

Glass capillary tubes were filled with potassium metal to improve handling of the material. Using tubes minimizes the surface area of the exposed metal to just the open end of the tube, allowing the potassium to be safely handled in air for short times with a minimal amount of oxidation of the metal. Tubes can also be calibrated so to know the amount of potassium per length of filled tube. The tubes were filled with potassium using a custom glass pressure reactor. The reactor, shown in Figure 2.1, has an aluminum base that seals with silicon o-rings onto a wide glass tube. The lid screws on and is sealed with a silicon o-ring. The lid of the reactor has three ports: a valve with a hose barb, a pressure gauge, and a pressure release valve.

Figure 2.1: Custom reactor for filling capillary tubes with potassium.

In a glovebox, a small beaker was placed in the bottom of the pressure reactor. To it, a lump of potassium metal was added. Divots were made in the metal with the closed end of a melting point capillary tube (Kimble), then the open end of a tube was inserted into each divot. Once an adequate number of tubes were added, the reactor lid was closed and brought out of the glovebox and attached to a Schlenk line with the barbed valve. The reactor was evacuated for at least half an hour to remove any gas contained in the capillary tubes. Then, the reactor was slowly heated above the melting point of potassium, to about 120 ^{o}C. Failure to adequately evacuate the tubes before melting the potassium could cause the remaining gas to bubble through the molten potassium and spray metal into the reactor. Once the

potassium melted, the Schlenk line was switched to high pressure (about 1 atmosphere) argon, which forced the potassium metal to flow up the empty capillary tubes. Afterwards the potassium was allowed to cool to room temperature. The reactor was then returned to the glovebox, where the tube could be removed and stored in a jar in the glovebox. The procedure could then be repeated until most of the potassium had been consumed. Excess potassium in the beaker was quenched under inert atmosphere with *tert*-butanol, followed by isopropanol, methanol, and finally water.

The tubes produced in this way consistently were filled with one to two inches of uninterrupted potassium metal. To use a tube, a section of tube filled with metal was scored with a carbide knife and broken. The tube was then measured with a metal ruler and scored at the wanted length. After breaking the tube, a set of calipers was used to confirm the length of tube. Typically, once the length was known, tubes were then broken into smaller pieces for ease of use.

2.2.3 Titration of Potassium in Capillary Tubes

Sections of capillary tubes filled with potassium were titrated to measure the amount of potassium per length of tube. In a glovebox, about 20 mm of tube was cut and the length was accurately measured. The tube was broken into smaller pieces and placed in a small round bottom flask sealed with a septum. The flask with the inserted tube pieces was then brought out of the glovebox to a Schlenk line. Argon that was first bubbled through distilled water was flown through the round bottom flask until all the potassium was quenched. This ensured that the potassium did not

react with oxygen or carbon dioxide in the air and was completely converted to potassium hydroxide.

The potassium hydroxide was then rinsed into a 50 ml volumetric flask, and the diluted solution was then used to rinse and fill a buret. The buret was then used to titrate a known mass of potassium hydrogen phthalate (KHP) dissolved in water, with phenolphthalein as an indicator of the end point. Each filled buret could titrate three KHP samples. From the volume of the end point and the mass of KHP, the mass of potassium in the section of tube can be calculated. This procedure was performed for 9 capillary sections of potassium, for a total of 27 titrations. A t-test was used to remove 3 outliers from the 2nd round of titrations.[2] The remaining titrations yielded an average 9.5 mg/cm of potassium tube with a standard deviation of 0.3 mg/cm and standard deviation of the mean of 0.06 mg/cm. This data is summarized in Table 2.1.

Table 2.1: Data from titrations of capillary tubes filled with potassium.

Trial Number	Length K tube (mm)	Mass KHP (mg)	Volume KOH Added (mL)	Mass of K per length (mg/cm)
1	19.5	20.7	10.60	9.59
		20.1	10.50	9.40
		19.2	9.75	9.67
2	31.0	21.7	8.60	7.79
		20.3	7.60	8.25
		22.3	8.40	8.20
3	29.5	19.8	6.60	9.73
		25.5	8.90	9.30
		22.5	7.55	9.67
4	29.5	19.6	6.00	9.77
		23.0	7.20	9.56
		20.7	6.20	9.99
5	30.5	21.6	7.00	9.68
		21.8	7.20	9.50
		20.5	6.35	10.13
6	30.5	20.1	6.80	9.28
		22.3	7.55	9.27
		20.5	6.95	9.26

7	30.0	19.0	6.80	8.92
		19.2	6.75	9.08
		22.0	7.80	9.00
8	29.0	19.7	6.55	9.93
		22.5	7.55	9.84
		18.4	6.50	9.34
9	27.5	15.5	5.60	9.63
		16.8	6.10	9.59
		18.1	6.70	9.40

For convenience for making potassium doped *p*-terphenyl with K_x:*p*-terphenyl stoichiometry, the average mass per length of tube was transformed into Equation 1. The factor of 0.179 accounts for the mass of potassium per cm tube, the molar mass of potassium, and the molar mass of *p*-terphenyl.

$$0.179Mx = l \quad (1)$$

where M is the mass of *p*-terphenyl used in milligrams, x is the desired mole ratio of potassium to *p*-terphenyl, giving l, the necessary length of capillary tube.

2.2.4 General Procedure for Sealing K_x:*p*-Terphenyl Samples with THF

THF was first pre-dried with potassium sulfate overnight, then refluxed in the presence of sodium metal and benzophenone until the solution turned a persistent dark blue. The THF was distilled and placed over activated 3 Å molecular sieves (20 % m/v) for greater than 48 hours. It was then distilled over the sieves and

used immediately. This procedure is known to produce THF dried to a low single digit ppm of water.[3]

The custom-made glass apparatus used for this experiment is shown in Figure 2.2. It consisted of two parallel, bridged tubes and an elbowed side arm coming off the right tube. Each tube had an opening at the top with a constriction near the opening to facilitate flame sealing. The opening of the right tube was sized with half inch tubing so that it could be attached to vacuum lines with ultratorr fittings. An arm extended horizontally out of the bridge connecting the tubes, and two cuvettes extended from the horizontal arm. One cuvette was glass and had a 1 mm path length for *in situ* spectroscopic measurements of the solution, the other was fused silica and had a 1 cm path length, and was intended for solution deposition of the K_2:*p*-terphenyl film. Each cuvette had a constriction in the tube leading to it to facilitate flame sealing from the larger apparatus.

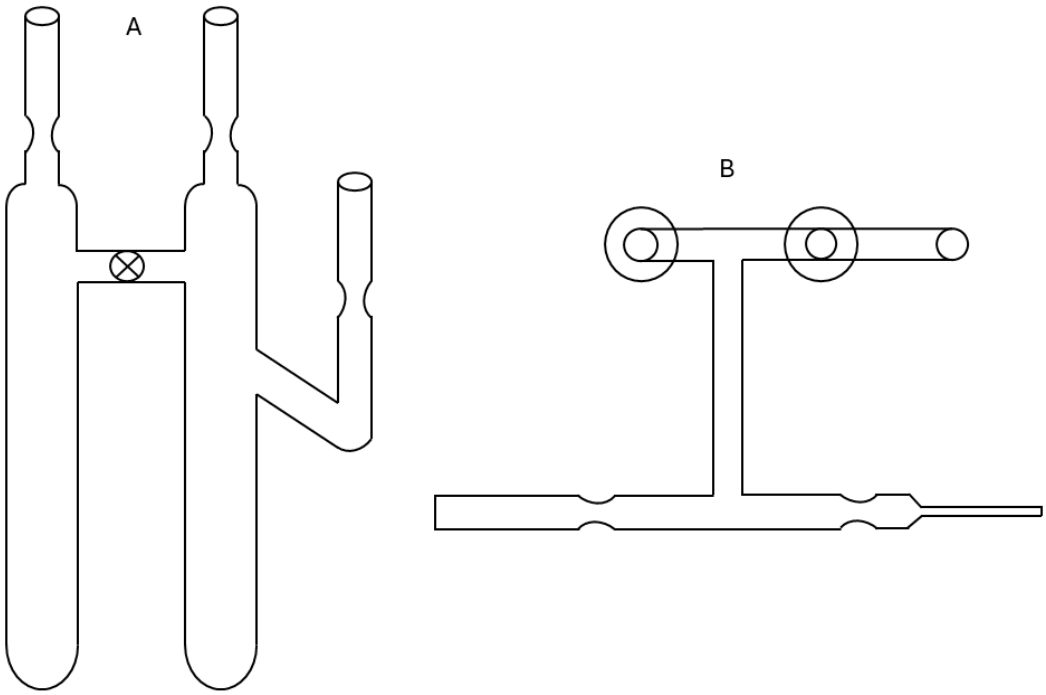

Figure 2.2: A) Side view of glass apparatus, showing the two vertical tubes and side arm. B) Top view showing the horizontal arm and attached cuvettes. Not drawn to scale.

After the apparatus was flame dried, 3.5 mg of *p*-terphenyl was added to the left tube of the manifold. The amount of *p*-terphenyl was chosen to allow for optical spectroscopy to be performed on the film and solution. A length of potassium capillary tube was added to the right most arm. The openings above *p*-terphenyl and potassium tubes were flame sealed, and the apparatus was attached to a high vacuum manifold, pumped by cold trap, diffusion pump, and two stage backing pump. The apparatus was pumped until the pressure reached below 10^{-6} torr to ensure there were no leaks, monitored by a hot-cathode ion gauge. Rapidly, the apparatus was vented to air and 13 ml of prepared THF was added to the middle tube via syringe and frozen with liquid nitrogen before reconnecting to the vacuum

line. Five freeze-pump-thaw cycles were performed on the THF to degas the solvent, allowing the pressure to decrease to 10^{-5} torr for each cycle, well below the vapor pressure of THF. With the THF frozen, the apparatus was then pumped for 7 hours to a pressure of 4×10^{-6} torr, when it was flame sealed off the vacuum manifold.

A potassium mirror was used to further dry and remove reactive gases from the THF. The side arm with potassium capillary tube was wrapped in heating tape followed by glass fiber tape. A thermocouple heating probe was inserted into the tape to monitor the temperature. After freezing the THF in liquid nitrogen, the tape was heated with a variac to 200 ^{o}C. While heating, a sponge that had been soaked in salted ice water was clamped around the other side of the tube containing THF. For best results, the sponge was resubmerged in ice water every few minutes. After about half an hour, a thin, violet film of potassium metal formed on the inside of the tube. The variac was then turned off and the THF was allowed to warm to room temperature. The mirror slowly turned white as it was consumed by reactive species in the tube. It was remade twice a day for the next few days until it persisted indefinitely.

2.2.5 Reduction of *p*-Terphenyl and Film Deposition

The THF was mixed with the *p*-terphenyl in the tube and repeatedly passed over the potassium mirror, reducing the *p*-terphenyl. The reaction progress was monitored with UV-Vis spectroscopy by inverting the filling the 1 mm pathlength cuvette, which was then inserted into the spectrometer. After the reduction was complete, the apparatus was inverted to fill the 1 cm pathlength cuvette. The right

tube of the apparatus was cooled in liquid nitrogen, allowing a vacuum transfer of THF from the arm with the cuvette to the cooled tube of the apparatus. Heating tape was wrapped around the 1 cm cuvette and used to keep the solution from being evaporatively cooled and slowing deposition. At the same time, care was taken to minimize bumping of the THF. After complete evaporation of the THF, the interior of the cuvette is left coated with a film of potassium and reduced *p*-terphenyl. The cuvette was then flame sealed from the rest of the apparatus. The 1 mm cuvette was filled with some of the remaining solution and, after carefully cooling the cuvette and freezing the remaining THF in the apparatus, the cuvette was quickly flame sealed from the apparatus. Both cuvettes of the film and solution were further studied with UV-Vis spectroscopy.

2.2.6 Preparation of Potassium Thin Film for Spectroscopy

To study the UV-Visible spectroscopy of pure potassium metal phases, a thin film of potassium metal with gradient thickness was prepared. This was done using a 1 cm path length quartz cuvette with a quartz to glass gradient and a glass tube with constriction. A small section of potassium capillary tube was added to the cuvette and the cuvette was added to the high vacuum manifold. After pumping to 10^{-6} torr, the cuvette was sealed off from the manifold. Heating tape was wrapped around the glass end of the tube and heated with the tube inverted such that the potassium capillary tube was in the hot end of the tube. After 12 hours of heating at 200 ^{o}C, a mirror of potassium had deposited onto the cuvette, decreasing in thickness as it extended to the bottom of the cuvette. UV-Vis spectroscopy was

performed on the cuvette as a function of relative film thickness by progressively raising the cuvette in the spectrometer by inserting shims into the cuvette holder between successive measurements. The shims were made of cardstock and were approximately 0.5 mm thick.

2.3 Results and Discussion

2.3.1 UV-Vis Spectroscopy of Reduced *p*-Terphenyl Solutions

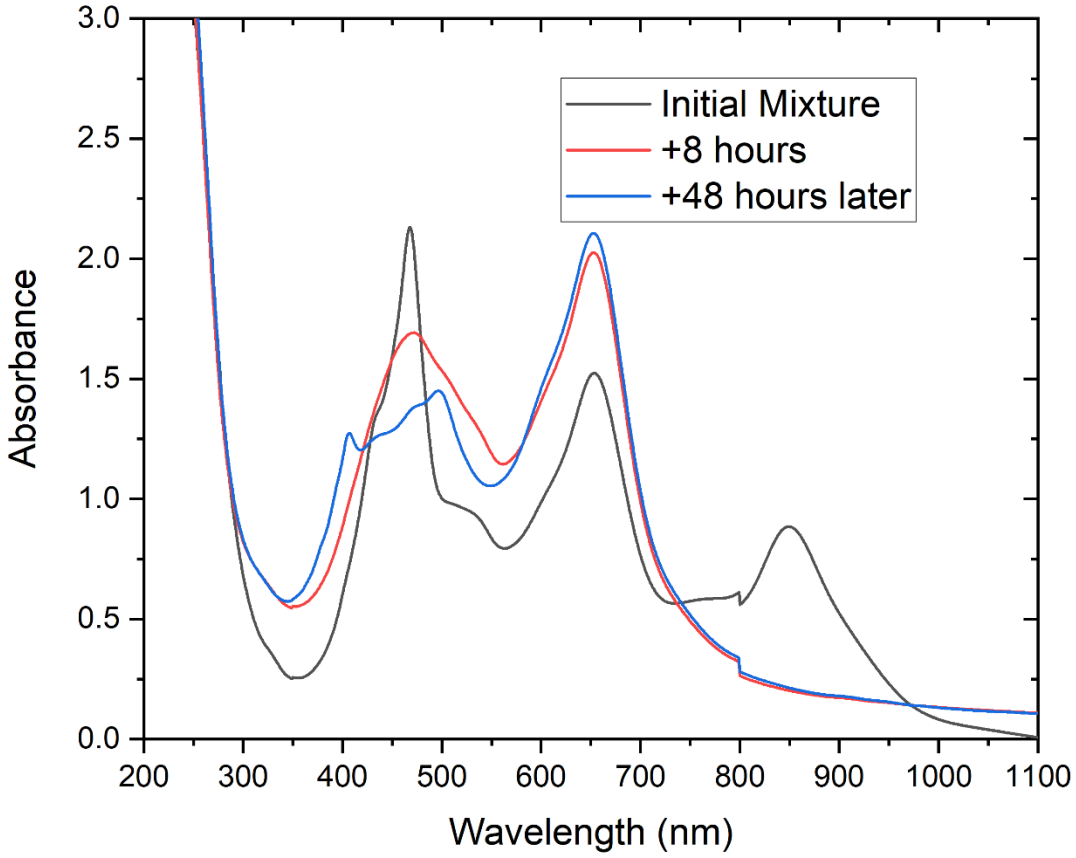

Figure 2.3: UV-Vis absorption spectrum of *p*-terphenyl solution in THF with repeated exposure to potassium mirror of various lengths of time, as indicated in the legend.

The UV-Vis spectra of the solution after continued exposure to the potassium mirror are shown in Figure 2.3. The initial green-blue solution showed three peaks

at 468 nm, 654 nm, and 850 nm. The discontinuity at 800 nm is an artifact where the spectrometer switched detectors. After 8 hours exposure to the potassium mirror, the solution turned a deeper blue. The peak at 468 broadened and decreased in intensity and the peak at 654 nm increased in intensity. The peak at 850 nm completely disappeared. After prolonged (48 hour) exposure to the mirror, the peak at 468 nm became considerably distorted, while the peak at 654 nm was only slightly decreased in intensity.

Sakamoto *et al*[1] report the anion of p-terphenyl in THF to an intense narrow peak at 462 nm, and two broad NIR peaks at 830 nm and 912 nm and that the dianion has a single peak at 648 nm. The three peaks in the initial mixture indicate the solution is a mixture of the mono- and dianion. The peak in our spectrum at 654 nm is very similarly structured to what they report. However, we see no evidence of a second NIR peak around 912 nm. After continuing exposure to the mirror, we interpret the disappearance of the 850 nm peak as complete conversion of the anion to the dianion. The persistent broad peak around 450 nm is also in disagreement with their spectrum of the dianion. However, Figure 4 shows the absorbance of the solution after deposition of the dianion film, a process which serves to dilute the solution. The solution spectrum within this plot (red trace) shows that the 450 nm feature disappears completely after the concentration of the solution has been decreased. This suggests that the 450 nm peak is a result of aggregation of the dianion solution.

2.3.2 UV-Vis Spectroscopy of the K_2:*p*-Terphenyl Film

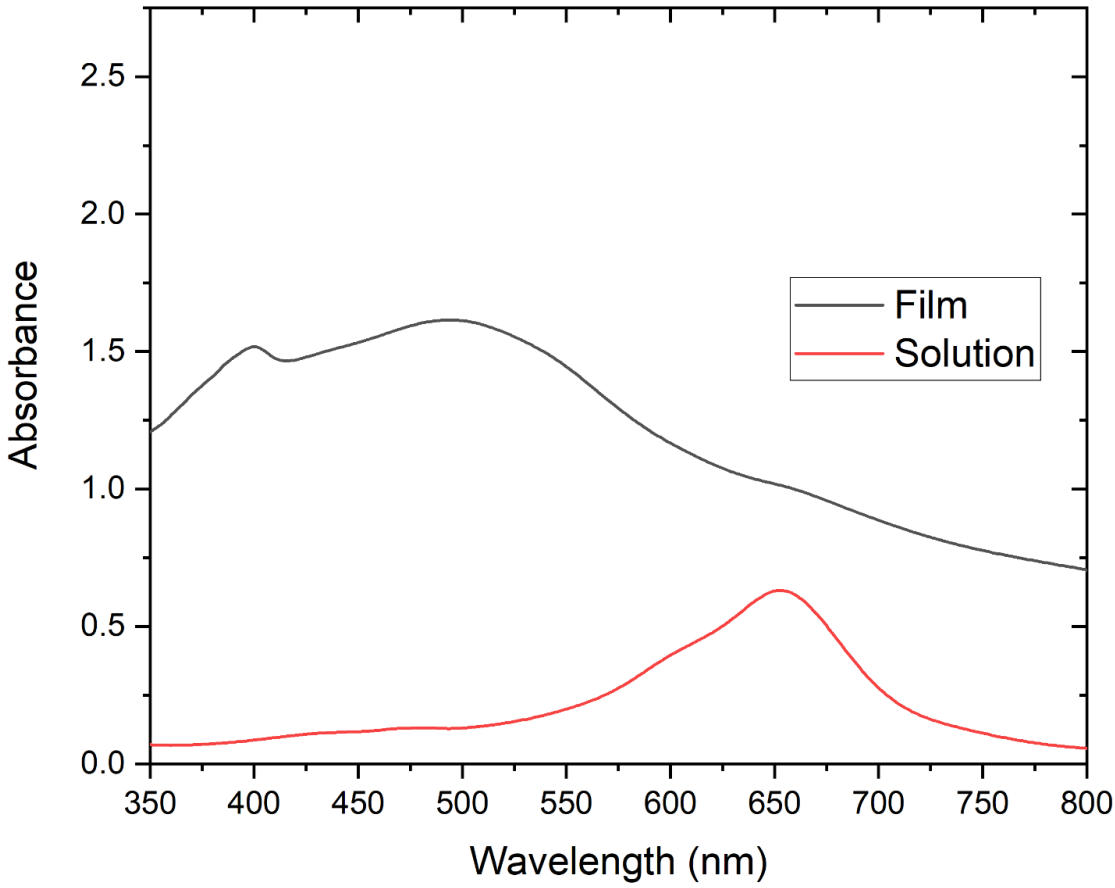

Figure 2.4: UV-Vis spectra of the solution deposited film of K_2:*p*-terphenyl and remaining dianion solution after deposition.

Figure 2.4 shows the UV-Vis spectra of the solution deposited K_2:*p*-terphenyl film and the remaining dianion solution after deposition. The solution shows a decrease in absorbance corresponding to the dianion, and as discussed above, the complete disappearance of any additional peaks. Four years after sealing the cuvette, the solution is still a bright vibrant blue.

The spectrum of the film is dramatically different from the solution. This is not so surprising, since the electronic states of a solid can be dramatically different

from the molecule in solution. There is a slight feature at 654 nm, exactly where the peak of the dianion in solution is. This possibly indicates that the film is not completely dry and still contains some small amount of material interacting with THF molecules. There are two other peaks in the UV-Vis spectrum: one relatively narrow one at 400 nm and a broad one at 500 nm. Two distinct peaks could indicate a mixture of phases or materials in the film.

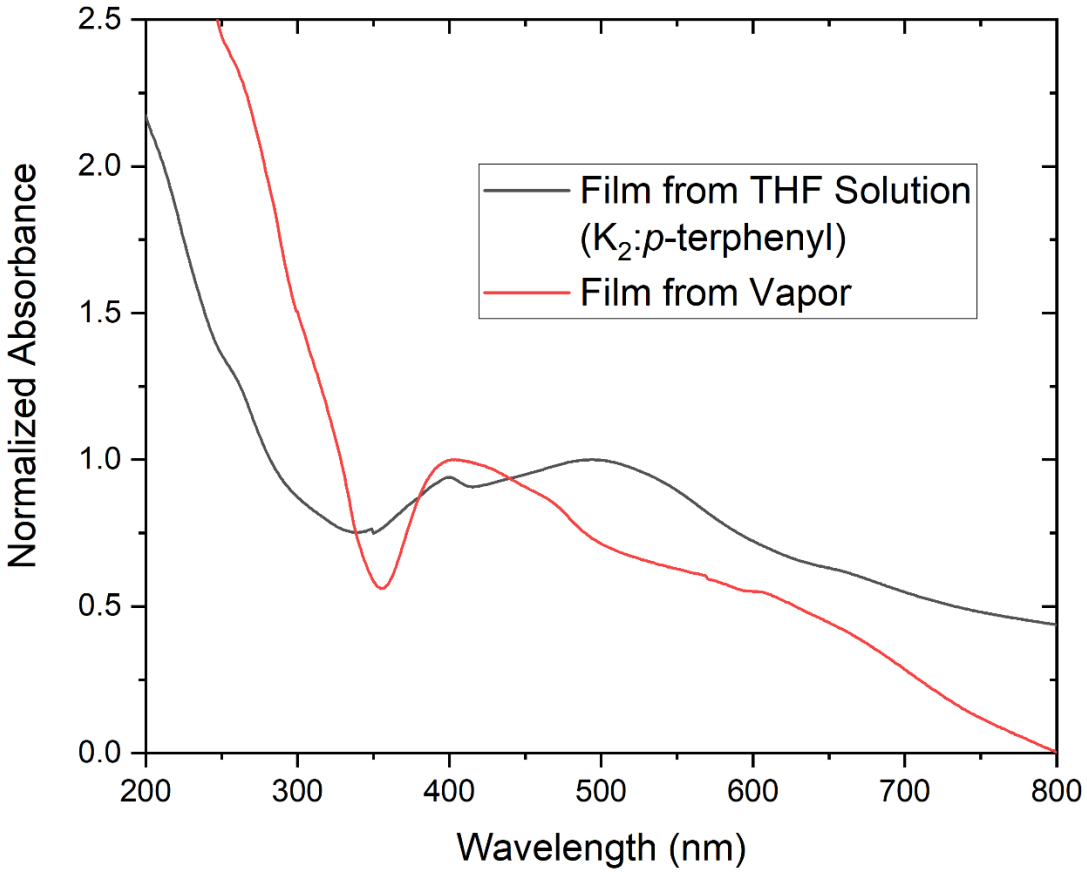

Figure 2.5: UV-Vis spectra of the K_2:*p*-terphenyl film deposited from solution with a vapor phase deposited film of potassium and terphenyl.

Figure 2.5 compares the UV-Vis of the solution deposited film with that of a vapor deposited K_x:*p*-terphenyl film produced by the Dessau group by heating

crystals of *p*-terphenyl with excess potassium metal. This method produces a brown to black powder with an unknown molar ratio of potassium to *p*-terphenyl. Both spectra show an absorbance peak at 400 nm. This suggests the vapor deposited film also contains K_2:*p*-terphenyl, which is consistent with the literature, where attempts were made to quantify the potassium doping in vapor deposited films of potassium doped *p*-terphenyl.[4,5] However, this does not explain the second absorbance peak centered at 500 nm that is seen in the spectrum of the solution deposited film.

2.3.3 UV-Vis Spectroscopy of Potassium Mirror

We hypothesized that absorbance band centered at 500 nm in the UV-Vis could be caused by scattering from a pure potassium phase in the material. A potassium mirror, shown in Figure 2.6, appears blue to violet to the human eye. This color could easily be explained by a broad absorbance peak in the middle of the visible spectrum, passing blue and red light that is interpreted by our eyes as purple. The color could originate from thin film interferences in the mirror. Alternatively, since the color persists when the mirror is thin enough to appear to be composed of individual particles of potassium, the color could originate from scattering from surface plasmon resonances on the particles of potassium. Regardless of the origin, we decided it was prudent to study the absorbance spectrum of a potassium mirror to gain insight into the spectroscopic properties of a potential potassium phase.

Figure 2.6: Potassium mirror deposited on the inside of cuvette with gradient of potassium metal thickness. The thinnest part of the mirror shows individual particles of potassium.

Figure 2.7 A shows the UV-Vis absorbance spectra of the potassium mirror as the cuvette is raised in the spectrometer with an increasing number of shims. Figure 7b shows the peak wavelength of the absorbance band as a function of number of shims. As more shims are added, the cuvette was raised higher and higher in the sample holder, allowing the spectrometer to probe thinner and thinner sections of the mirror.

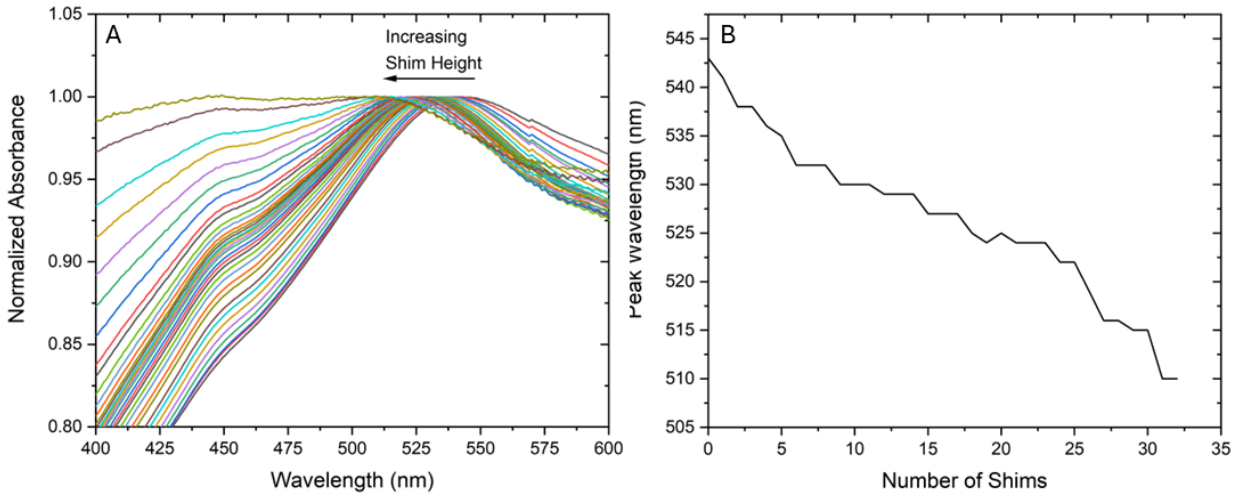

Figure 2.7: A) UV-Vis spectra of potassium mirror as the mirror is raised in the spectrometer by shims. B) Absorbance peak as a function of the number of shims.

Generally, the potassium mirror has a broad band centered between 500 nm and 550 nm, with a steep decrease on the blue side of the band. As the mirror gets thinner, the peak blue shifts and broadens. The spectra also flatten as the mirror scatters less and less light. There is a slight shoulder at 450 nm that does not shift with the thickness of the mirror. The location of the main band of the potassium mirror qualitatively agrees with the broad absorbance centered at 495 nm in the solution deposited film. The thinnest sections of the mirror are still red of the peak in the solution deposited film. However, if surface plasmons are contributing to the spectrum of the mirror, as the particles get smaller, their resonance is likely to continue to blue shift. This would be undetectable with the current mirror because the density of particles is too low, so the scattering is below the detection limit of the spectrometer.

To attempt to quantify how the spectral bands of vapor deposited films are related to the bands seen in the solution deposited film, Figure 8 shows the normalized UV-Vis spectra of the solution deposited film compared to the vapor deposited film and a spectrum of the potassium mirror. Additionally, it shows the sum of the spectra of the vapor deposited film and the potassium mirror. The spectrum of the mirror was chosen because of the proximity of its peak to that seen in the solution deposited film, while still not being too flat blue of 500 nm.

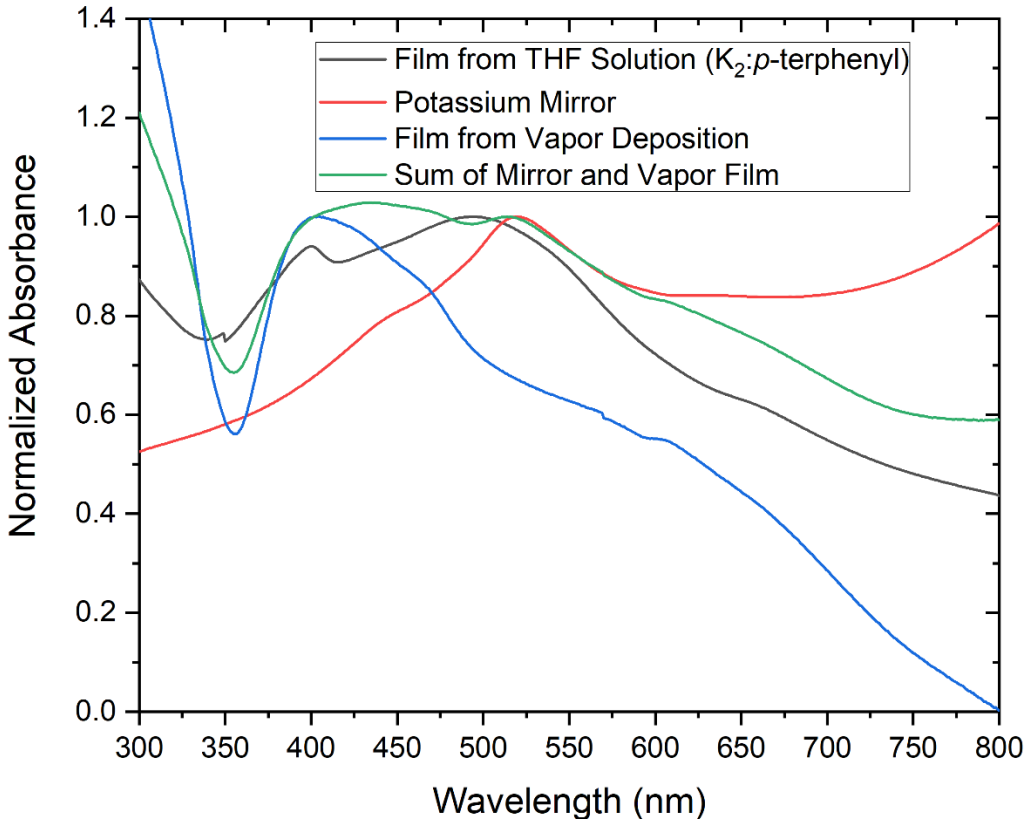

Figure 2.8: Normalized UV-Vis spectra of the vapor deposited K_2:*p*-terphenyl film, vapor deposited K_x:*p*-terphenyl film, and potassium mirror, as well as the normalized sum of the vapor deposited film and potassium mirror.

The sum spectrum in Figure 2.8 has two peaks at 435 nm and 515 nm, which are both red of peaks seen in the K_2:*p*-terphenyl film. The spectra are otherwise reasonably similar in structure, so the contribution of a potassium phase cannot be ruled out. This implies that even when a sufficient amount of potassium is present in solution, the dianion of *p*-terphenyl does not become more reduced. Alternatively, the excess potassium in solution was not in suitable form to reduce the dianion further, or deposit in the same phase as the dianion in the film, possibly because it already existed as a metallic cluster or nanoparticle. More work will need to be performed to understand this further.

2.4 Conclusion

Magnetometry and contactless conductivity measurements were performed on the K_2:*p*-terphenyl film in the Dessau and Shaheen labs. The measurements did not find any diamagnetic or metallic behavior in the film. It is possible that measuring these properties through the windows of a cuvette, along with the relatively small amount of material in the film, limited the effectiveness of these measurements.

This method of production of K_2:*p*-terphenyl is intrinsically limited in how much material can be made at one time because of the need to use optical spectroscopy to assess the progress of the reduction. Additionally, finer control over the conditions of the deposition of the film is desired to make more uniform materials to facilitate further characterization. In particular, the K_2:*p*-terphenyl film did not show any visible sign of crystallinity, limiting what potential structural

characterization could be performed. Most importantly, theoretical results indicate that higher levels of doping are necessary to achieve metallic and superconductive properties.[6,7] A different solvent system will be necessary to achieve these requirements.

References

1. Sakamoto, A.; Harada, T.; Tonegawa, N. A New Approach to the Spectral Study of Unstable Radicals and Ions in Solution by the Use of an Inert Gas Glovebox System: Observation and Analysis of the Infrared Spectra of the Radical Anion and Dianion of *p*-Terphneyl. *J. Am. Chem. Soc.* **2008,** *112,* 1180-1187.

2. Harris, D. C.; *Quantitative Chemical Analysis,* 7th Ed.; W. H. Freeman and Company: New York, 2007.

3. Williams, D. B. G.; Lawton, M. Drying of Organic Solvents: Quantitative Evaluation of the Efficiency of Several Desiccants. *J. Org. Chem.* **2010,** *75,* 8351-8354.

4. Carrera, M.; McDonald, J. L.; Untiedt, C.; Garcia-Hernandez, F. M.; Verges, J. A.; Guijarra, A. Characterization of Main Phase in K_x*p*-Terphenyl and Its Largest Congener $K_x$poly(*p*-phenylene): A Report of Their Magnetic and Electric Properties. *J. Chem. Phys. C* **2019,** *123,* 5264-5272.

5. Pinto, N.; Di Nicola, C.; Trapananti, A.; Minicucci, M.; Di Cicco, A.; Marcelli, A.; Bianconi, A.; Marchetti, F.; Pettinari, C.; Perali, A. Potassium-Doped Para-Terphenyl: Structure, Electrical Transport Properties and Possible Signatures of a Superconducting Transition. *Condens. Matter* **2020,** *5,* 78.

6. Zhong, G.-H.; Wang, X.-H.; Wang, R.-S.; Han, J.-X.; Zhang, C.; Chen, X.-J.; Lin, H.-Q. Structural and Bonding Characteristics of Potassium-Doped *p*-Terphenyl Superconductors. *J. Phys. Chem. C* **2018,** *122,* 3801-3808.

7. Yan, X.-W.; Huang, Z.; Gao, M.; Zhang, C. Stable Structural Phase of Potassium-Doped *p*-Terphenyl and Its Semiconducting State. *J. Phys. Chem. C* **2018,** *122,* 27648-27655.

CHAPTER 3

Synthesis of K_x:*p*-Terphenyl Using Liquid Ammonia

3.1 Introduction

This chapter explores liquid ammonia as a solvent for preparing and depositing films of K_x:*p*-terphenyl. The immediate goal is to have fine control over the level of potassium doping in the material, and to make large enough quantities for physical and structural characterization, namely conductivity measurements and x-ray crystallography. To this end, we also developed methods to measure the conductivity of air sensitive materials as a function of temperature. Secondarily, we used Fourier transform infrared spectroscopy which, supported with computational chemistry, allowed us to characterize the effect of potassium doping in the material and how the material degrades in air. We also discuss initial conductivity and powder x-ray diffraction experiments.

Ammonia readily dissolves alkali metals, where when dilute they form blue solutions caused by the solvated electron.[1] However, ammonia is a toxic gas at room temperature and must be condensed below -33 ^{o}C to use as a solvent. An additional hazard to this occurs when dissolving potassium metal, which is extremely pyrophoric. The technical challenges posed by condensing gases for this purpose motivated us to explore using ethylenediamine (EDA) as an alternative solvent. This proved fruitless. EDA is very difficult to rigorously dry and degas, and it is sufficiently hygroscopic that it cannot be exposed to air after drying. Because of its high boiling point and heat capacity, vacuum transfers are difficult, if not

impossible. Additionally, the dissolution of potassium in EDA is slow at room temperature. When heated, the dissolved potassium metal readily forms an orange potassium amide. All these reasons make it an impractical solvent for this application.

Reduction of aromatic compounds with solvated alkali metals in liquid ammonia are commonly called Birch reductions.[2] Scheme 3.1 shows the mechanism for the reduction of benzene. The solvated electron first adds to a carbon in the aromatic ring, causing a radical to form *para* to the carbanion. The carbanion then reacts with an acid, usually the acidic proton on an alcohol. Afterwords, a second solvated electron reduces the radical to a carbanion, which again reacts with an acidic proton. For benzene, this forms 1,3-cyclohexadiene. The hydrogenated carbons are always *para* to each other, however the regiochemistry of these carbons relative to other substituents depends on whether the substituent is electron withdrawing and electron donating.

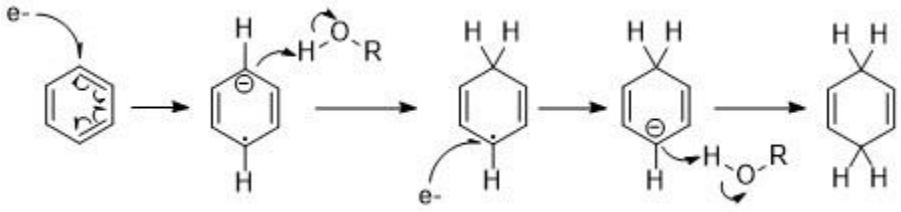

Scheme 3.1: Mechanism of the Birch reduction of benzene using alkali metals dissolved in liquid ammonia.

For *p*-terphenyl, it is known that the carbanion after the first reduction forms on one of the peripheral phenyl groups in the para position.[3] In an excess of potassium and the absence of a proton source, a second reduction should result in

symmetric *para* positions of the carbanions, shown in Scheme 3.2, which would minimize electrostatic repulsion. This is consistent with computational results on the gas phase structure of the dianion, which shows the conversion of the benzoidal structure of *p*-terphenyl to a more quinoidal structure upon sequential reduction.[4] Our own computational results confirm this.

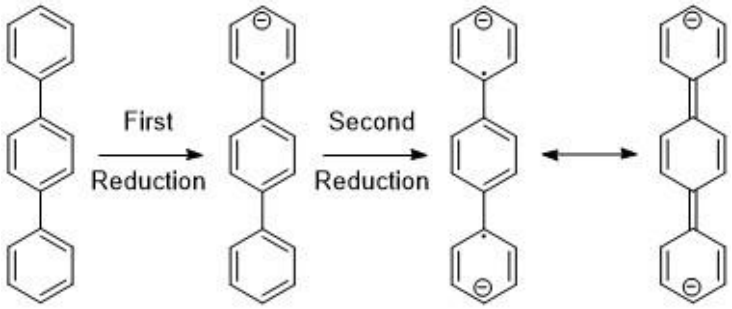

Scheme 3.2: Lewis structures of the anion and dianion of *p*-terphenyl, showing the increasing quinoidal character with increased reduction.

The literature claims that exposure of K_x:*p*-terphenyl to air produces *p*-terphenyl with no degradation of the material.[5,6] As can be seen in the Birch reduction mechanism, it is likely that the moisture in air will facilitate (via proton transfer) irreversible reduction of the aromatic rings to cycloalkenes. In liquid ammonia, quenching of the *p*-terphenyl radical anion with water produces a dihydro product with the cyclodiene on the side central phenyl.[3] It is unclear how the regioselectivity of the reaction will be affected by quenching in the solid state.

We are not the first group to explore using liquid ammonia as a means to produce alkali metal doped organic materials. Peres *et al*[7] used a similar procedure to produce phenylene oligomers reduced by sodium and potassium. However, they used a very small ratio of 0.4 moles alkali metal to phenylene and did nothing to

explore precise doping levels of the metal. Also, their characterization with x-ray photoelectron spectroscopy and Raman spectroscopy produced contradictory results that were not interpreted.

3.2 Materials and Methods

3.2.1 General

Potassium capillary tubes were produced and calibrated as described in the previous chapter. *p*-Terphenyl (Alfa Aesar, 99+%) was used as is. For samples produced for conductivity measurements, potassium tubes were made from ultrahigh purity potassium (ThermoFisher Scientific, 99.95%) and *p*-terphenyl was further purified by sublimation. Anhydrous ammonia was from Airgas. Hexanes used in the glovebox was first dried over activated sieves for 2 days, then pushed through plug of dried silica and degassed by bubbling argon through the solvent for 3 hours. Unless otherwise stated, all custom glassware was made by the author.

3.2.2 General Procedure of Producing K_x:*p*-terphenyl

A homemade reaction vessel was used for the *p*-terphenyl reduction. It consisted of a 19 mm diameter pyrex tube 3-4 inches long with rounded bottom on one end, attached to a half inch open ended tube on the other. The vessel was loaded with a homemade glass stir bar, made by sealing the core of a Teflon coated stirbar in a 3 mm diameter tube, and constriction was added to facilitate flame sealing after the reaction. The open end of the vessel was connected to a Schlenk line with an ultratorr fitting and braiding reinforced flexible PVC tubing. The plastic tubing had one fork that led to a glass oil bubbler with Teflon valve, and another fork that

led to a glass dry ice condenser with round bottom flask and Teflon stirbar. The dry ice condenser was attached directly to the ammonia cylinder. Flow from the cylinder was controlled by a valve.

The reaction vessel was flame dried, sealed with a rubber septum, and allowed to cool before loading with 100 mg of *p*-terphenyl. The vessel was then loaded into the glovebox, where a measured length of potassium capillary tube was added to reach the desired doping level. The quantification of the amount of potassium per length of capillary tube is described in the previous chapter.

Meanwhile, the dry ice condenser and round bottom flask were flame dried under vacuum from the Schlenk line. After cooling, two small lumps of sodium metal were added to the round bottom flask and the reaction vessel was attached to the tubing with the ultratorr fitting. The entire setup was then evacuated and purged with argon, cycling a total of 5 times. After the final evacuation, the Schlenk line was closed, and the ammonia cylinder was opened and allowed to fill the setup and flow through the attached bubbler. This was necessary because the presence of large quantity argon in the setup inhibits condensation and distillation of the ammonia. After the flow of ammonia was established, the round bottom flask was submerged in a dry ice and hexanes bath, and dry ice and hexanes were added to the condenser. Simultaneously, the valve on the bubbler was closed. Ammonia was allowed to condense and stirred in the round bottom flask until around 30 to 50 ml accumulated. The valve on the cylinder was then closed, and the flask was raised out of the dry ice bath, keeping dry ice in the condenser, and the ammonia was

allowed to reflux for 15 minutes. Refluxing the liquid ammonia with sodium metal dries the ammonia and removes iron impurities.[8]

After refluxing, the reaction vessel was submerged in a -50 ^{o}C bath of methylcyclohexane, cooled by an immersion cooler (SP Industries FC100), placed on a magnetic stirring plate. The dry ice and hexanes were then removed from the condenser, and the ammonia was distilled into cooled reaction vessel. After enough ammonia condensed in the reaction vessel, the setup was opened to the Schlenk line and put under argon, allowing the remaining ammonia in the round bottom flask to evaporate. The reaction vessel was stirred for 1 hour, after which the magnetic stirrer and immersion cooler were turned off while the reaction vessel remained submerged in the solvent bath. This allowed the vessel to slowly warm up and the ammonia to evaporate, leaving behind the K_x:*p*-terphenyl solid, a dark blue-gray to black crystalline material.

After all the ammonia in the vessel evaporated, the vessel was removed from the solvent bath and allowed to warm to room temperature, then evacuated and briefly heated with a heat gun to remove any residual ammonia. The vessel was then purged with argon and evacuated, cycling 5 times, and flame sealed under vacuum. Once sealed, the vessel could seemingly be stored indefinitely with no visible degradation of the material. The vessel could be opened in a glovebox and the material scraped out for characterization. When placed in a vial which was stored in a mason jar, the black color of the material could persist for several months, depending on the condition of the glovebox environment.

3.2.3 Intentional Quenching K_3:*p*-terphenyl

A sample of K_3:*p*-terphenyl was prepared as described above. The sample was then opened in the glovebox and divided into three portions. One portion was used for FTIR and XRD as is. The other portions were put in vials sealed with rubber septa. To one, gas from a Breathing Quality Air cylinder (Airgas) was flowed through it. To the second, argon that was bubbled through distilled water was flowed through it. After sufficient time, both samples were then purged with dry argon and cycled back into the glovebox, where FTIR was performed. They were later further characterized with XRD.

3.2.4 FTIR Spectroscopy

Fourier Transform Infrared Spectroscopy was performed with a Cary 630 FTIR Spectrometer (Agilent) with attenuated total reflectance (ATR) sampling module. The spectrometer was equipped with a diamond ATR crystal. The spectrometer is small enough that it and a laptop could be cycled into the glovebox for air-free measurements. The sample was ground in a mortar and pestle before loading onto the ATR crystal and pressing with the built-in sample press. The ATR crystal and press were thoroughly cleaned with hexanes before and after each measurement. The measured spectra were used without any processing.

3.2.5 Preparation of Samples for Conductivity Measurements

KBr powder was dried in a vacuum oven at 350 ^{o}C overnight and then transferred into the glovebox. Double sided Kapton tape was applied to the anvil of a lever-style KBr pellet press for FTIR sample preparation. Four tin strips, cut from

tin foil (Sigma Aldrich), were then stuck to the tape in 4 parallel lines, with part of each tin strip sticking up, making an L shape for each strip. The anvil was then covered in KBr powder, and the protruding ends of the leads were folded over the powder. This was then pressed into a pellet with the pellet press. Removing the anvils and double-sided tape left a KBr pellet with 4 equally spaced leads on one side that were flush with the surface of the KBr. A photograph of the pellet beside a ruler was taken to quantify the distance between the leads. The KBr on the other side of the pellet could be scraped to reveal the other end of each tin lead.

To the side with flush tin leads, a small amount of K_x:*p*-terphenyl powder was added, followed by more KBr powder on top. This was then pressed again to form a sandwich of KBr, K_x:*p*-terphenyl, tin leads, and KBr again. The pellet was attached to a custom printed circuit board (PCB) for conductivity measurements using double sided tape. The tin leads on the pellet were then soldered to copper wire leads using indium wire as a solder. The copper wire connected to the PCB for a four-contact conductivity measurement with an inline electrode geometry.

Conductivity measurements were taken with a Dynacool Physical Properties Measurement System (PPMS). The PCB with the sample was inserted into sample holder, shown in Figure 3.1, and inserted into the PPMS. The PPMS was purged with argon and evacuated three times before measurements began. A current of 1 mA was applied to the sample through the two exterior tin leads, and the voltage drop was measured across the two interior leads. The resistance was measured as a function of temperature from 300 K to 1.8 K. The sample was then held at 1.8 K for

20 minutes, the resistance was measured while heating the sample back to 300 K. A 3 T magnetic field was then applied to the sample, and the resistance was measured again as a function of temperature from 300 K to 63 K. After measurement, the sample was exposed to air for two days and the room temperature resistance was measured again.

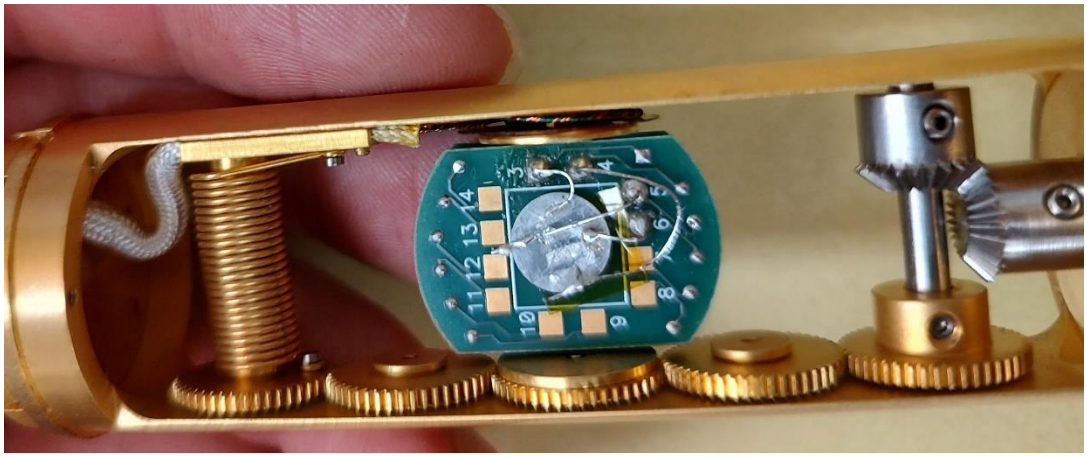

Figure 3.5: $K_{2.5}$:*p*-terphenyl sample for four contact conductivity measurements. The KBr pellet with tin electrodes is taped to the PCB, and copper wire leads connect the electrodes to the PCB. The black $K_{2.5}$:*p*-terphenyl material is faintly visible in the KBr pellet.

3.2.6 Computational Methods

Density functional theory (DFT) calculations were performed on neutral *p*-terphenyl, the anion, dianion, and trianion in the gas phase using Orca 5.0.[9] The M06-2X functional was chosen for its high accuracy with organic molecules.[10] The D3zero dispersion correction and the cc-pvtz basis set were used. The anion and trianion were chosen to have doublet spin multiplicity, and the dianion singlet spin multiplicity. For each species, geometry optimizations were done on both

unconstrained and constrained geometries. The unconstrained optimization started with an initial geometry with the central phenyl ring twisted out of plane. The constrained optimization started with a completely flat initial geometry and constrained all the dihedral angles at zero degrees. Analytical frequency calculations were performed on each set of optimized geometries without imposed geometric constraints. Avogadro and Chemcraft were used to visualize geometries and vibrations.

3.2.7 Powder X-Ray Diffraction

Powder x-ray diffraction (XRD) was performed using a Rigaku SmartLab diffractometer using a Cu K-α source with 1.5404 Å x-rays and a Bragg-Brentano focusing geometry. A Cu filter was used to suppress the K-α2 line. An air-free sample with Kapton windows was used with sample well made of a Si zero order diffraction plate. Samples were either powder or pressed into a pellet. Pellets were held in the sample holder with a piece of double sided Kapton tape. All samples were loaded into the sample holder in a glovebox.

All samples had a low angle amorphous background from the Kapton windows of the air-free sample holder. This was subtracted by measuring the diffraction of the empty sample holder, scaling the signal to the sample diffraction pattern and subtracting. Any additional amorphous background from the sample was fitted with a polynomial function and subtracted.

3.3 Results and Discussion

3.3.1 Initial Methods with Liquid Ammonia

An extensive amount of work was done to improve the synthetic methods needed to produce K_x:*p*-terphenyl. Initially ammonia was condensed directly from the cylinder and the reaction was performed entirely in standard glassware with fritted fittings, silicone tubing, and Teflon stopcock valves. Potassium and terphenyl were added to condensed ammonia by rotating Schlenk tubes around the fritted joints. The material was isolated for deposition by rotating the entire vessel to pour the ammonia into a side arm. Stirbars were not used to stir the reaction vessel because only Teflon coated ones were available, and they degrade in alkali metal-ammonia solutions. Lastly, thin films of the material were deposited onto silicon substrates for characterization.

Initially ammonia was condensed using 3-necked round bottom flasks. A dry flask was loaded with potassium capillary tubes, the condenser was attached to the center flask, *p*-terphenyl was held in a Schlenk flask on one side, and the cylinder was attached directly to the other side with flexible tubing. After condensation of the ammonia, the Schlenk flask was rotated, and the entire setup was shaken to add terphenyl into the liquid ammonia. After reacting for some time, the setup was again tilted and shaken to fill the Schlenk tube with liquid ammonia K_x:*p*-terphenyl solution. After the ammonia evaporated the Schlenk tube could be flame sealed from the apparatus. While inelegant, this procedure produced a black powder consistent with our expectations of the material. Additionally, the shape of the Schlenk tube could be changed to facilitate measurements, for instance using a precision NMR tube for microwave conductivity measurements. However, working

at scales necessary for extensive characterization was not feasible. Moreover, the material degraded rapidly, forming white islands in the powder within 12 hours. It was discovered that anhydrous ammonia contains a considerable quantity of water, oxygen, and iron containing salts. These can be removed by first distilling the liquid ammonia over sodium before use.[8] Additionally, we speculated that the setup was too leaky, and minimizing the number of valves, tubing, and fritted fittings, as well as changing the vacuum pump would improve the stability of the product.

Making such changes resulted in an experimental setup similar to what is used in the final procedure. Using the custom reaction vessel, it could produce a black powder that persisted indefinitely. To characterize the material with XRD and conductivity measurements, silicon substrates could be added to the vessel before the reaction, with the material deposited on them during the liquid ammonia evaporation. XRD could then be performed on the substrate after the vessel had been opened in a glovebox. For conductivity measurements, the substrate could have gold electrodes deposited on it before the reaction as well. However, initial XRD measurements showed the presence of a neat *p*-terphenyl phase in the material even for samples with high doping levels of potassium. It was determined that, since *p*-terphenyl is not readily soluble in ammonia on its own, stirring would facilitate its reduction by potassium, dissolution, and eventual deposition into a single phase.

Therefore, custom glass stirbars were made and added to the reaction vessel. This removed the *p*-terphenyl phase in highly doped samples, however stirring

substrates with gold electrodes was enough physical agitation to remove the electrodes from the substrate, even when adhesion layers were used to help adhere to the gold. To prevent this, a sidearm was added to the reaction vessel where the substrate could be stored during the reaction, and at the end, during the evaporation of liquid ammonia, the vessel would be carefully tilted and shaken to submerge the substrate in the solution. However, K_x:*p*-terphenyl was fragile and prone to flaking, making it difficult to measure the conductivity at room temperature. Several efforts were made to produce glass and quartz vessels with electrical feed throughs, where the material could be deposited and directly measured without ever opening the vessel or manipulating a substrate. These efforts were in vain since K_x:*p*-terphenyl material did not adhere well to any surface.

We observed, though, that it could be pressed into robust pellets using a pellet press for traditional FTIR spectroscopy samples. This led to the procedure described in the methods section, where flame sealed vessels of the material were opened in the glovebox, the sample was scraped out of the vessel and used as a powder or pressed into pellets for characterization.

3.3.2 Description of the K_x:*p*-Terphenyl Material

Figure 3,2 shows a K_3:*p*-terphenyl sample. In the tube, the bottom of the vessel contains the bulk of the material, and is composed of a gray-blue, sparkly powder, indicative of formation of crystallite domains. The inhomogeneities in the middle of the vessel appear to be a result of the liquid-gas interface of the ammonia

solution. The top of the vessel is spotted from the splatter of the boiling liquid ammonia solution. Scraping material from any section of the tube results in a fine, uniform black powder. No large crystallites are ever seen.

Figure 3.6: Typical K_3:*p*-terphenyl sample in flame sealed reaction vessel.

So far, three other doping levels were also produced and studied: K_1:*p*-terphenyl, K_2:*p*-terphenyl, $K_{2.5}$:*p*-terphenyl. The K_2:*p*-terphenyl and $K_{2.5}$:*p*-terphenyl materials visibly look very similar to K_3:*p*-terphenyl. However, K_1:*p*-terphenyl samples often have white powdery sections in the material, shown in Figure 3.3. This indicates that a significant amount of unreduced *p*-terphenyl remains in the powder and that at such low doping levels, there is not enough potassium in solution to fully reduce the terphenyl and dissolve it. This suggests that the liquid ammonia synthesis is unsuitable for low doping levels of potassium.

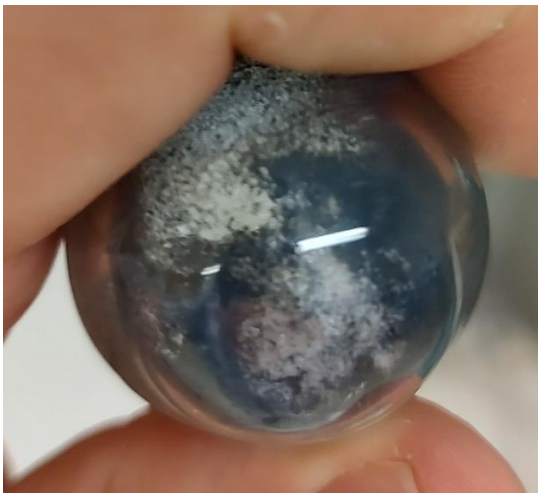

Figure 3.7: K_1:*p*-terphenyl, showing islands of unreduced *p*-terphenyl.

3.3.3 Computational Results

Our computational results are mostly in line with published results.[4] Unconstrained geometries of *p*-terphenyl and its first two anions optimize to a twisted geometry, where the center phenyl ring is twisted out of plane from the other two phenyl rings. The dihedral angle of the twisted ring for neutral *p*-terphenyl was 37.8°, while the twist of the anion was 17.5° and dianion was 3.04°. Notably, the dianion did not optimize to a flat geometry with the phenyl rings in the same plane. The trianion breaks this trend. The phenyl rings in the trianion are no longer flat and pucker out of plane. This also breaks the symmetry of the molecule as on one side the ring is puckered by about 11° while the other ring is puckered only by about 0.5°. The middle ring puckers by about 4°.

Constraining the dihedral angles of each species to force the atoms to remain in plane typically causes the energies of each species to increase. For *p*-terphenyl, the difference in energy between the constrained and unconstrained geometries was 0.183 eV. For the anion it was 0.011 eV, however for the dianion the constrained

energy was actually 0.001 eV lower than the unconstrained. The trianion breaks the trend of decreasing energy difference between the constrained and unconstrained geometries, with an energy difference 0.043 eV.

The bond lengths of each species did not measurably change between the constrained and unconstrained geometries. They are summarized in Table 3.1 for *p*-terphenyl and the anion and dianion, using the standard bond numbering convention for substituted benzenes. The trianion breaks symmetry and no longer has consistent bond lengths between each ring.

Table 3.1: Bond lengths of *p*-terphenyl and its first two anions

Species	Middle Ring 2-3 Bond Length (Å)	Middle Ring 1-2 Bond Length (Å)	Inter-Ring Bond Length (Å)	End Ring 1-2 Bond Length (Å)	End Ring 2-3 Bond Length (Å)	End Ring 3-4 Bond Length (Å)
p-Terphenyl	1.38	1.40	1.49	1.40	1.39	1.39
Anion	1.37	1.42	1.44	1.42	1.38	1.39
Dianion	1.36	1.45	1.40	1.45	1.37	1.40

All of this is consistent with *p*-terphenyl becoming more benzoidal as it is reduced to the dianion. *p*-Terphenyl has rings of mostly uniform bond length. The central ring is twisted out of plane to minimize steric hinderance between the

hydrogens on the phenyl rings. Upon reduction, the bond between phenyl rings becomes shorter and the dihedral angle decreases, twisting the rings in plane. Additionally, the 1-2 and 3-4 bonds of each ring lengthen, and the 2-3 bonds shorten. This is exactly as expected from the reduction shown in Scheme 2.

Additional reduction of the dianion to triple anion does not continue to follow the trend to benzoidal geometry. For instance, while one of the inter-phenyl bonds shortens further to 1.38 Å, the second lengthens to 1.46 Å. Similarly, the puckered end phenyl ring has a lengthening of the 1-2 bonds (1.47 Å) and 3-4 bonds (1.42) and a shortening of the 2-3 bonds (1.37 Å), the other end ring shows the opposite trend. The 1-2 bonds (1.42 Å) and 3-4 bonds (1.39 Å) shorten, and the 2-3 bonds (1.45 Å) lengthen.

Moreover, the five highest occupied orbitals of the trianion have positive energies, compared to just the singly occupied orbital of the anion and HOMO and HOMO – 1 of the dianion. This indicates that reducing the dianion to trianion significantly increases the antibonding character in the molecule. The previous chapter showed that even when excess potassium metal was in solution, an additional reduction of the dianion did not occur. It will also be shown below that no new spectral features appear in the FTIR of the solid that would indicate additional reduction of the dianion. As such, our discussion of the potential trianion will end here.

Vibrational spectra of both the constrained and unconstrained optimized geometries of the *p*-terphenyl and its anions were calculated using analytical

gradients. The constrained geometries of *p*-terphenyl, the anion, and dianion all had imaginary frequencies that twisted the center ring out of plane. But the vibrational spectrum of each species did not appreciably change from the constrained to unconstrained geometries. Since the solids of *p*-terphenyl and K_x:*p*-terphenyl are all expected to have planer geometries of the phenyl rings, we will limit our analysis of the calculated vibrational spectra to the constrained geometries.

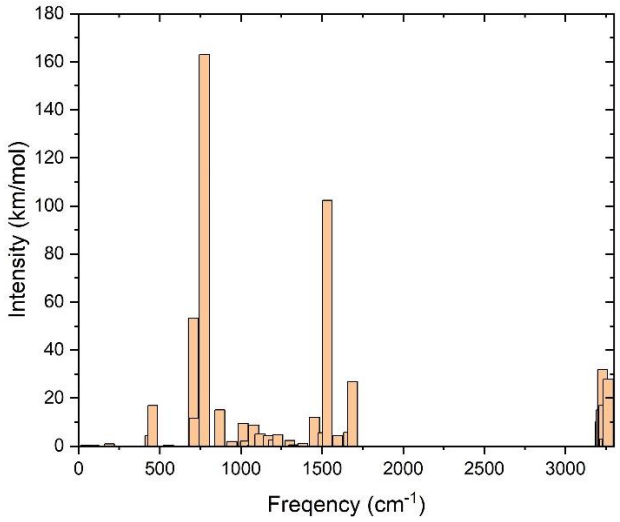

Figure 3.8: Calculated IR spectrum of *p*-terphenyl.

Figure 3.4 shows the calculated IR spectrum of *p*-terphenyl. There are several features typical of aromatic hydrocarbons. The bands below 3200 cm^{-1} are all in plane C-H stretches. Similar IR active vibrations appear in the anion and dianion spectra, making them difficult to differentiate experimentally. As such, we will focus on the spectral features seen below 1800 cm^{-1}, shown in Figure 3.5 for *p*-terphenyl.

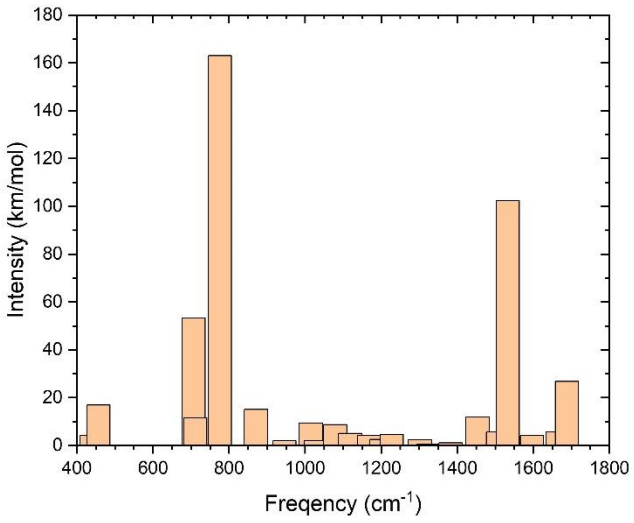

Figure 3.9: Calculated IR Spectrum of *p*-terphenyl between 400 cm^{-1} and 1800 cm^{-1}.

The intense IR active vibrations below 1000 cm^{-1} are caused by out of plane C-H bending of the phenyl rings. Of note, there are two intense bands at 707 cm^{-1} and 776 cm^{-1} that are asymmetric and symmetric bends of this type. Additionally, we will highlight the band at 872 cm^{-1}, a symmetric C-H bend where the end phenyl rings bend in opposite directions to the center phenyl ring, almost like the flapping of a bird. Two other intense bands that we'll highlight are at 1532 cm^{-1} and 1683 cm^{-1}, which are in plane symmetric and asymmetric CC stretches in the phenyl rings.

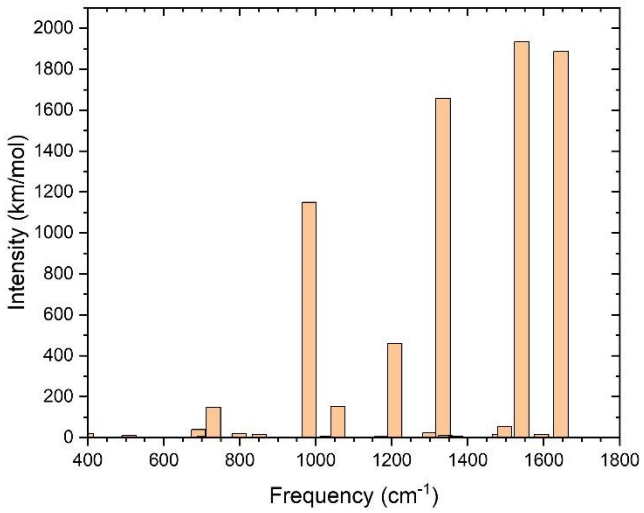

Figure 3.10: Calculated IR Spectrum of the *p*-terphenyl anion.

Figure 3.6 shows the calculated IR spectrum of the anion of terphenyl, which is markedly different from the neutral *p*-terphenyl spectrum. The most intense bands are between 900 cm^{-1} and 1700 cm^{-1}. Figure 3.7 shows the IR spectrum of the dianion. Aside from differences in intensity of specific peaks, the anion and dianion spectra show very similar bands. Table 3.2 summarizes the high intensity bands of each spectrum. Notably, neither the anion nor dianion have a vibrational band around 870 cm^{-1}.

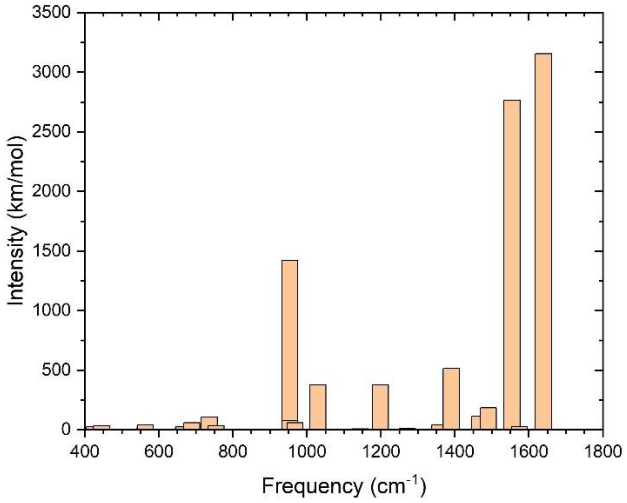

Figure 3.11: Calculated IR Spectrum of the *p*-terphenyl dianion.

Table 3.2: Summary of Anion and Dianion IR Spectral Bands.

Vibrational Mode	Anion Frequency (cm^{-1})	Dianion Frequency (cm^{-1})
Asymmetric C-C Stretch	983	957
Asymmetric C-C Stretch	1056	1031
Asymmetric In-Plane C-H Bend	1207	1201
Asymmetric C-C Stretch	1342	1391
Asymmetric C-C Stretch	1547	1555
Symmetric C-C Stretch	1639	1639

The asymmetric vibrations at 983 (957) cm^{-1} and 1056 (1031) cm^{-1} for the anion (dianion) correspond to in plane C-C stretches that primarily stretch the 1-2 and 3-4 C-C bonds. As the *p*-terphenyl becomes reduced and more quinoidal, those bonds lengthen, which would decrease the vibrational frequency of that bond

stretch. Additionally, the asymmetric C-C stretch at 1342 (1391) cm^{-1} for the anion (dianion) corresponds to a C-C stretch primarily between the inter-phenyl carbon atoms. Again, as the molecule is reduced and becomes more quinoidal, these bonds decrease in length, making their stretching frequency higher. The asymmetric C-H bend at 1207 (1201) cm^{-1} for the anion (dianion) is a C-H scissoring between the hydrogens bonded to the 2-3 carbon atoms. The bend does not appreciably change the 2-3 C-C bond length during the vibration, so its frequency should not be affected by the length of the 2-3 C-C bond.

The asymmetric C-C stretch at 1547 (1555) cm^{-1} of the anion (dianion) involves stretching of both the inter-phenyl carbons and the 1-2 carbon stretches. Similarly, the symmetric C-C stretch at 1639 (1639) cm^{-1} primarily involves stretching of the 1-2, 2-3, and 3-4 C-C bonds. For both of these vibrations, we postulate that the lengthening of the 1-2 and 3-4 C-C bonds cancels out the shortening of the 2-3 C-C bond, minimally changing the frequency of each vibration.

3.3.4 FTIR Spectroscopy of K_x:*p*-Terphenyl

The attenuated total reflectance (ATR) FTIR spectrometer was used because the instrument neatly fit within the antechamber of our glovebox, so air-free sample measurement was straightforward. It also facilitates ease of measurement of solid samples. A small quantity of sample could be scooped onto the ATR crystal and pressed against it with the built-in anvil. This is considerably easier than using a transmission spectrometer, which requires the sample to be diluted by grinding it into a transparent medium, such as KBr powder, which has the potential to quench

the material. Still, the ATR geometry causes significant complications to the measured spectra. The depth the evanescent wave penetrates the sample depends strongly on both the real and imaginary refractive indices of the material. Because of this, the position of bands shift and their intensity changes when they are in proximity of other resonances.[11] The lineshape of peaks can also change, causing them to look negative or dispersive. Without a detailed understanding of the optical constants of the material, the reflectivity cannot be converted to absorbance. This means that quantitative assignment of the ATR-FTIR reflectivity data is not possible. Here, we focus on the qualitative analysis of the ATR-FTIR spectra of K_x:*p*-terphenyl materials, added by the calculated spectra described in the previous section.

The ATR-FTIR spectra of neat *p*-terphenyl is shown in Figure 3.8. Similarly to the computational frequency analysis, we will focus on the low energy side of the spectrum. Additionally, he bands between 2000 cm^{-1} and 2500 cm^{-1} are artifacts of the instrument and appear in all measured spectra. Figure 3.9 shows the ATR-FTIR spectrum of *p*-terphenyl between 400 and 2000 cm^{-1}.

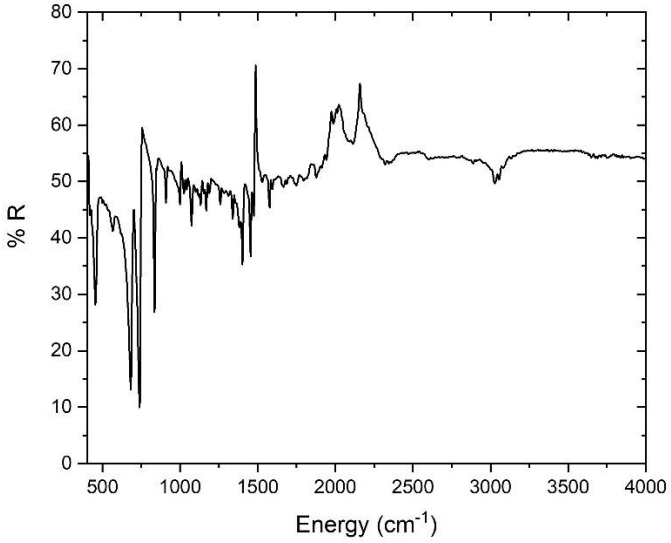

Figure 3.12: ATR-FTIR spectrum of *p*-terphenyl.

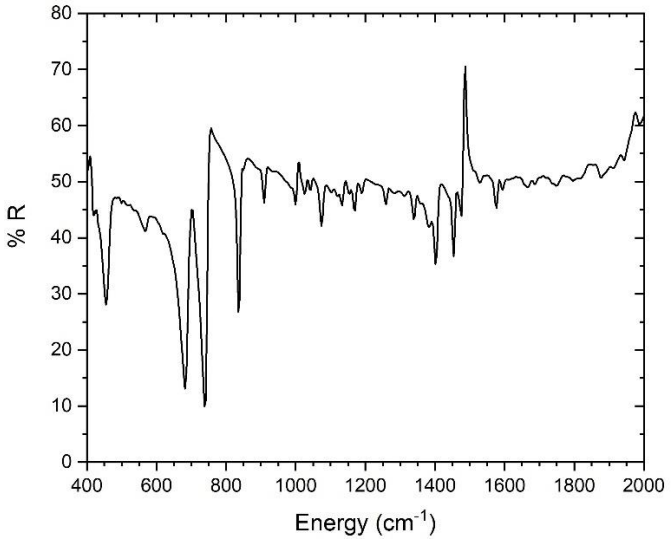

Figure 3.13: ATR-FTIR spectrum of *p*-terphenyl from 400 cm^{-1} to 2000 cm^{-1}.

In Figure 3.9, several of the bands described found in the computational spectra are present, notably the bands at 454 cm^{-1}, 682 cm^{-1}, 742 cm^{-1}, and 840 cm^{-1} correspond well to the computed 455 cm^{-1}, 707 cm^{-1}, 776 cm^{-1}, and 872 cm^{-1}. Other band assignments are more challenging since the density of vibrational bands

causes shifts of their positions, intensities, and lineshapes. The high intensity of the negative band (that increases in a % reflectivity plot) at 1490 cm^{-1} likely corresponds to the computed 1532 cm^{-1} band, which had the high intensity of the vibrations in that region.

Figure 3.10 shows the ATR-FTIR spectrum of neat p-terphenyl compared to that of K_1:*p*-terphenyl. As can be seen, while there are distinct differences between these spectra, several bands in the K_1:*p*-terphenyl spectrum are also seen in the neat *p*-terphenyl spectrum. This can be seen most strikingly in the band at 840 cm^{-1}, which is both intense in *p*-terphenyl and well separated from other peaks to minimize distortions. This indicates that a significant amount of the K_1:*p*-terphenyl sample is still unreduced *p*-terphenyl, which is consistent with the observations made of the visible appearance of the K_1:*p*-terphenyl sample.

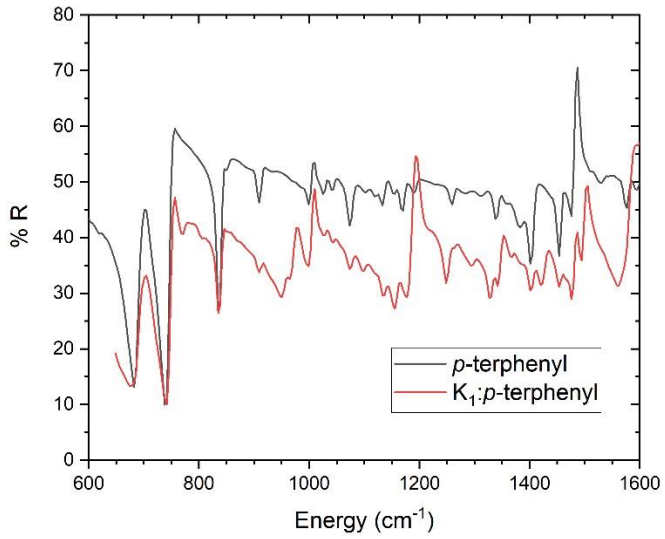

Figure 3.14: ATR-FTIR spectra of *p*-terphenyl and K_1:*p*-terphenyl.

Figure 3.11 shows the ATR-FTIR spectra of K_1:*p*-terphenyl, K_2:*p*-terphenyl, $K_{2.5}$:*p*-terphenyl, and K_3:*p*-terphenyl. There are bands at 948 cm^{-1}, 1010 cm^{-1}, 1194 cm^{-1}, 1326 cm^{-1}, and 1558 cm^{-1} that could correspond to those predicted in Table 2. However, as seen in the figure, these bands do not shift with higher doping of potassium metal, which would be expected if the *p*-terphenyl sample was progressively reduced with more doping. This suggests that the K_1:*p*-terphenyl material actually contains a significant amount of both *p*-terphenyl and the dianion, and a minimal amount of the anion. This makes sense from the molar proportions used to make this material. If equal parts potassium and *p*-terphenyl are mixed, and a significant amount of *p*-terphenyl remains, then what *p*-terphenyl did react must have reacted twice with the potassium.

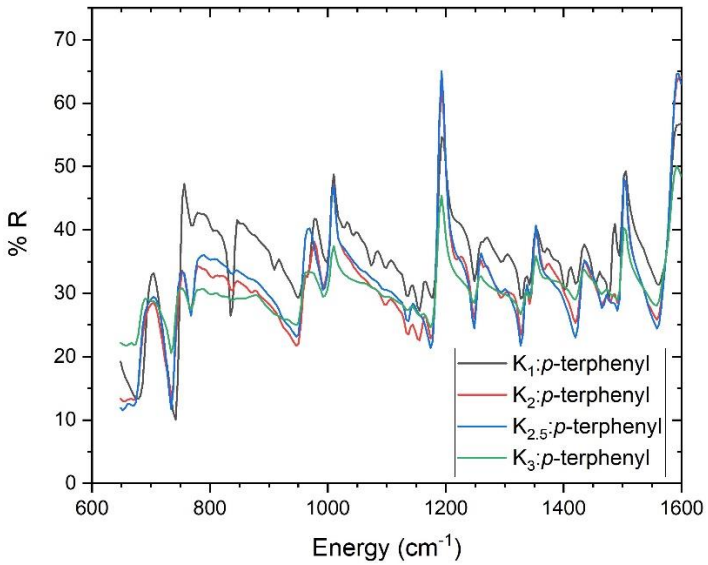

Figure 3.15: ATR-FTIR spectra of potassium doped *p*-terphenyl samples.

Additionally, we see that bands like the one at 840 cm^{-1}, which correspond to vibration in neutral *p*-terphenyl, persist even with a significant amount of potassium doping. Figure 3.12 shows this band for all four materials. We can see

that a slight dip at this frequency is seen even in the $K_{2.5}$:*p*-terphenyl material, indicating that unreduced *p*-terphenyl persists even when 2.5 molar equivalents of potassium are used in the solution. Initial XRD results show that the K_2:*p*-terphenyl and $K_{2.5}$:*p*-terphenyl samples do not contain a distinct *p*-terphenyl phase consistent with the neutral species. This means that the K_2:*p*-terphenyl and greater doping levels of potassium contain mixed oxidation states of *p*-terphenyl throughout the material. The implications of this to a superconducting state are not clear.

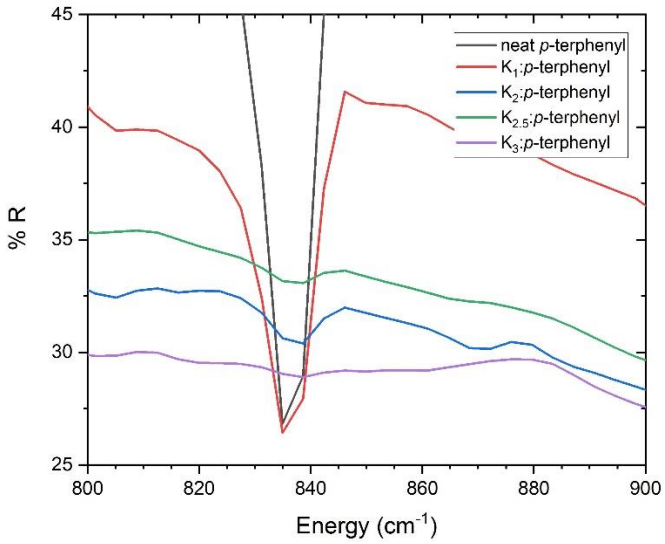

Figure 3.16: Close up of the 836 cm^{-1} band.

Figure 3.13 shows the ATR-FTIR spectra of the K_2:*p*-terphenyl, $K_{2.5}$:*p*-terphenyl, and K_3:*p*-terphenyl materials. Notably, no new bands form as doping increases in the material. This indicates that further reduction of the *p*-terphenyl from the dianion to a trianion does not occur, consistent with the energic arguments made in the previous section. Also, the relative intensity of bands diminishes as doping levels increase. This could be interpreted as a manifestation of the skin effect.[12] As the sample becomes more conducting and metallic, free electrons on the

surface prevent the evanescent field from penetrating deeply into the material. This would cause small intensity absorption bands to diminish in intensity and disappear in the spectrum.

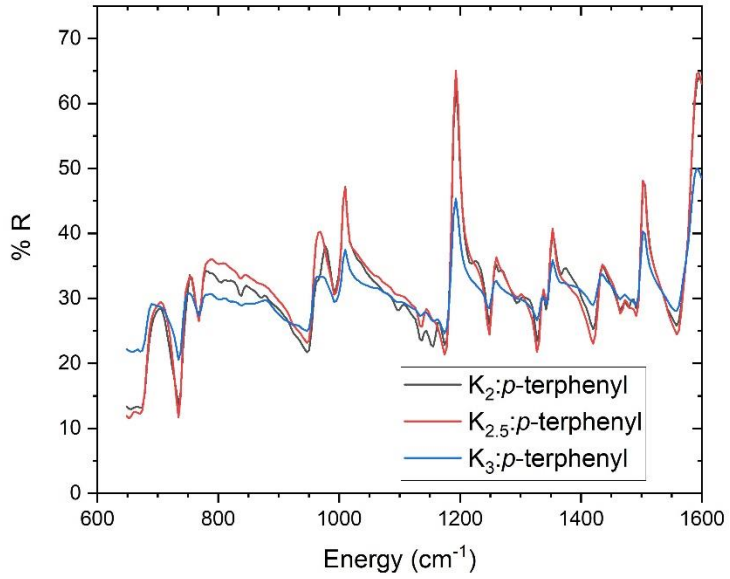

Figure 3.17: ATR-FTIR of K_2:*p*-terphenyl, $K_{2.5}$:*p*-terphenyl, and K_3:*p*-terphenyl.

Lastly, Figure 3.14 shows the ATR-FTIR spectra for four K_3:*p*-terphenyl prepared on different dates. The spectra are not offset, changes in reflectivity are a result of using different instruments. However, all the bands in each sample appear in each spectrum without any spectral shifts. This indicates this reaction reproducibly synthesizes the same K_3:*p*-terphenyl material each time.

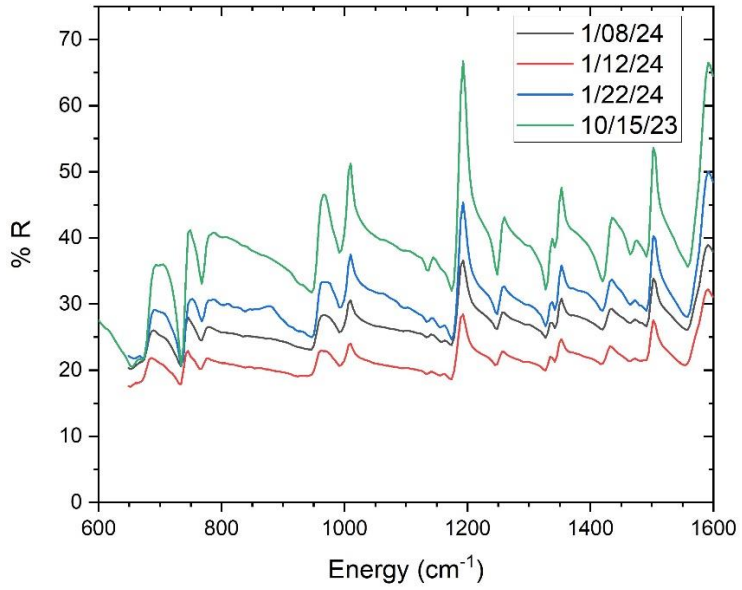

Figure 3.18: ATR-FTIR of multiple K_3:*p*-terphenyl samples prepared on the given dates.

3.3.5 FTIR Spectroscopy of Quenching Products of K_x:*p*-Terphenyl

The literature reports that while K_x:*p*-terphenyl degrades in the presence of moisture, the material turns into KOH and neat *p*-terphenyl (cite those two papers). We doubt the veracity of this claim, since in solution phase addition of water to the reaction will complete the Birch reduction and add hydrogen across a double bond. To explore this, K_3:*p*-terphenyl samples were prepared and quenched with water and oxygen. Quenching with wet argon gas quickly yields a white powder. ATR-FTIR of the white powder is show in Figure 3.15 and compared to the ATR-FTIR of neat *p*-terphenyl and wet KOH.

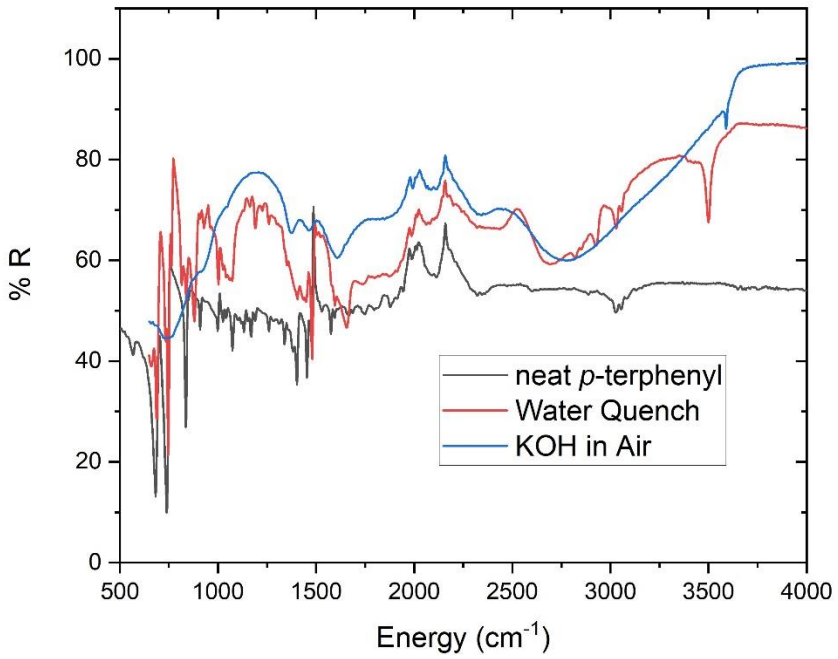

Figure 3.19: ATR-FTIR of K_3:*p*-terphenyl that was quenched with wet argon, compared with the spectra of neat *p*-terphenyl and KOH.

The KOH spectrum shows several broad bands, particularly at 2700 cm^{-1}, which is likely the OH stretch in the hydroxide. This feature is present in the spectrum of quenched material. Focusing on the low frequency spectrum, shown in Figure 3.16, we see that a number of the vibrational bands in neat *p*-terphenyl return upon quenching, however they are shifted to high frequency. For instance, the two bands at 682 cm^{-1} and 780 cm^{-1} both increase in frequency by 5 cm^{-1}. Additionally, the intensity of the band at 836 cm^{-1} does not fully return. We can only conclude that quenching K_3:*p*-terphenyl with a proton source such as water does not produce *p*-terphenyl with 100% conversion. The regiochemistry of birch reductions in solid state reactions has not been studied, therefore we speculate that the quenched material is a mixture of slightly different products.

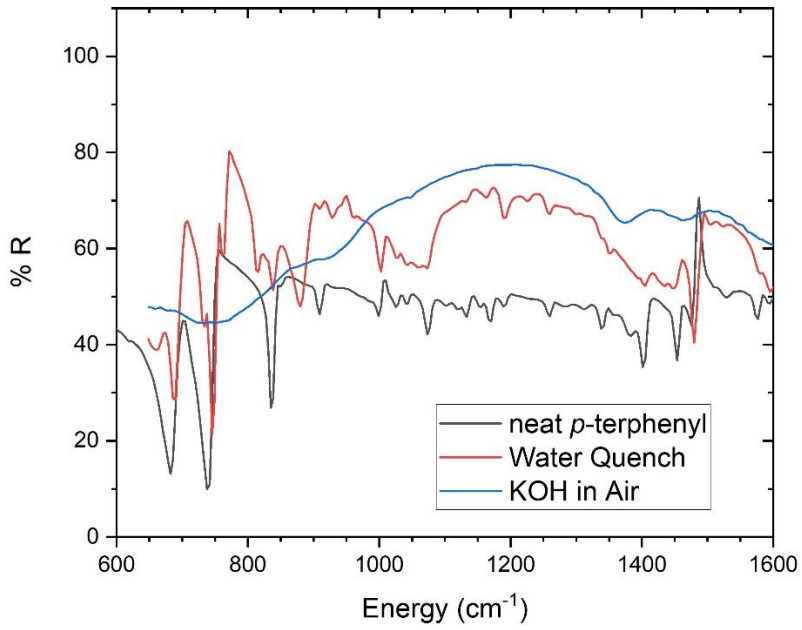

Figure 3.20: ATR-FTIR of K_3:*p*-terphenyl that was quenched with wet argon, zoomed in to below 1600 cm^{-1}, compared with the spectra of neat *p*-terphenyl and KOH.

Quenching of K_3:*p*-terphenyl with oxygen via breathing quality air was slower. After two hours, the material was still gray and not completely white. ATR-FTIR of the quenched material is shown in Figure 3.17 and compared with the spectra of neat *p*-terphneyl and potassium dioxide, KO_2. The spectra of KO_2 and the quenched material both have sharp bands at 3500 cm^{-1}, indicative of the KO stretch. They also both contain the broad band at 2700 cm^{-1}, showing the presence of the KOH in the material.

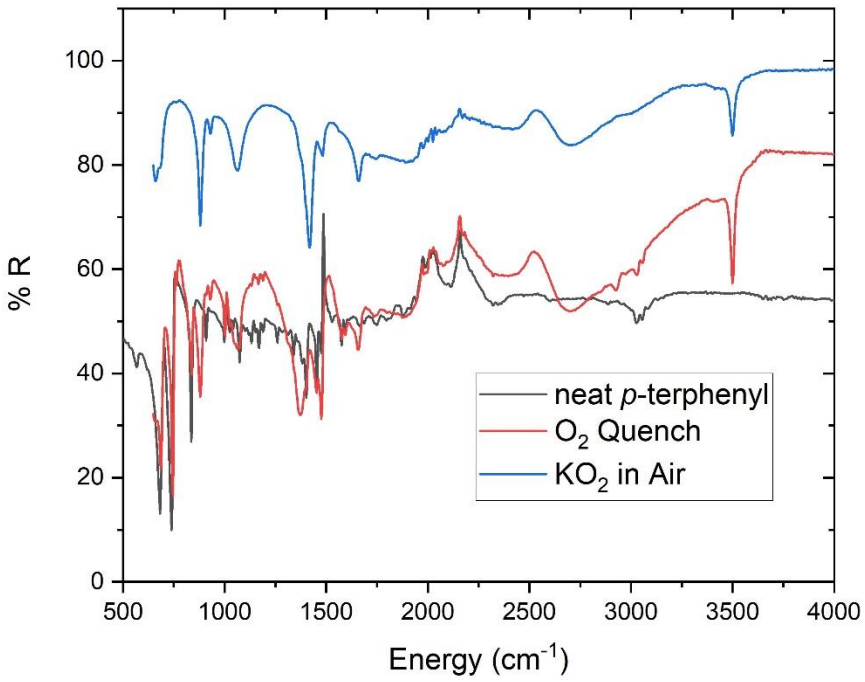

Figure 3.21: ATR-FTIR of K_3:*p*-terphenyl that was quenched with breathing quality air, , compared with the spectra of neat *p*-terphenyl and KO_2.

Figure 3.18 shows the low frequency spectra of the oxygen quenched material. Similar to the water quenched material, what peaks remain from *p*-terphenyl have shifted by 5 cm^{-1}, and the 836 cm^{-1} does not fully return.

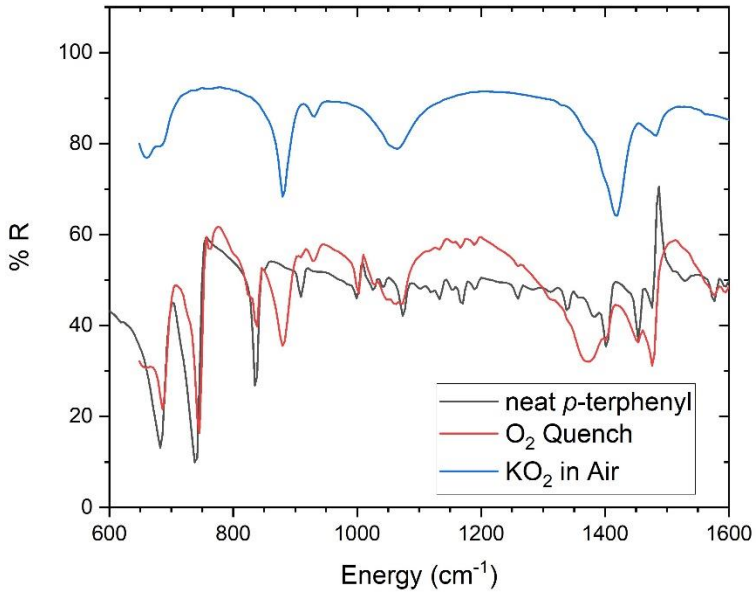

Figure 3.22: ATR-FTIR of K3:p-terphenyl that was quenched with wet argon, zoomed in to below 1600 cm-1, compared with the spectra of neat p-terphenyl and KO_2.

The breathing quality air still contains 10 ppm water. We speculate that since the oxygen quench was considerably slower, it is not the primary way in which the K_3:*p*-terphenyl material degrades in air. Instead, the material preferentially reacts with the small amount of water that remains in the breathing quality air. Either way, the product of degradation in both cases is not *p*-terphenyl.

3.3.6 XRD of K_x:*p*-terphenyl

Measurement of air sensitive samples has been particularly challenging. K_x:*p*-terphenyl often shows signs of degradation during the measurement, turning from black to a gray or white. This makes consistent measurements of samples before they have degraded challenging. Here, we only discuss qualitative interpretations of the XRD patterns of samples that showed no sign of degradation.

Quantitative analysis of these spectra and attempts to solve the crystal structure using Rietveld refinement with rigid body models are underway.

Figure 3.19 shows the XRD pattern of *p*-terphenyl powder. The pattern is nearly identical to the published pattern,[13] however the relative intensity of some of the peaks have changed. This is most likely due to a preferred orientation of the packing of crystal grains in the sample. If the crystallites are flakes, then they are likely to partially orient so that they appear stacked in the powder. This would cause diffraction from certain planes to be overrepresented in the powder and make scatter from those planes appear more intense relative to unpreferred planes.

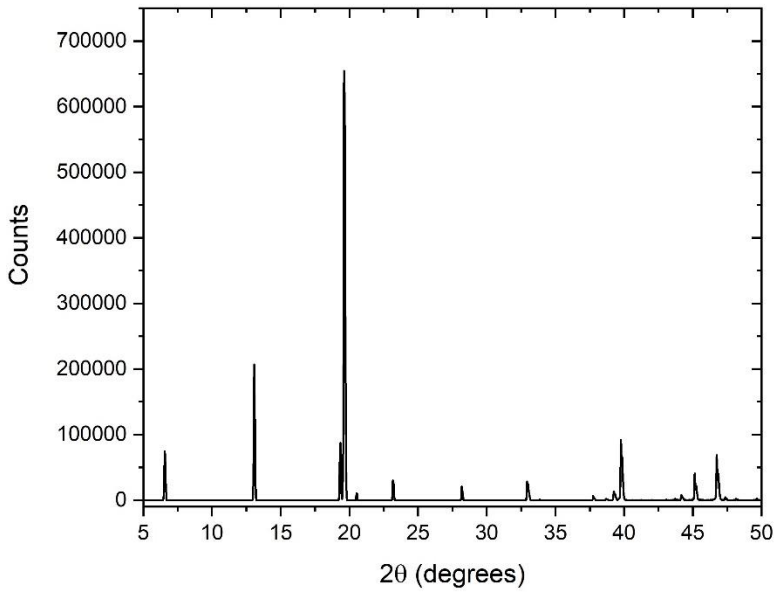

Figure 3.23: XRD pattern of *p*-terphenyl after background subtraction.

Figure 3.20 shows the XRD pattern of a K_3:*p*-terphenyl sample. The low angle background is caused by both the amorphous Kapton windows and an additional broad background apparent in all K_x:*p*-terphenyl samples. This indicates that, while the material shows narrow diffraction peaks at higher angles, a portion

of the material is amorphous. The amorphous background is subtracted from the pattern before quantitative analysis is performed.

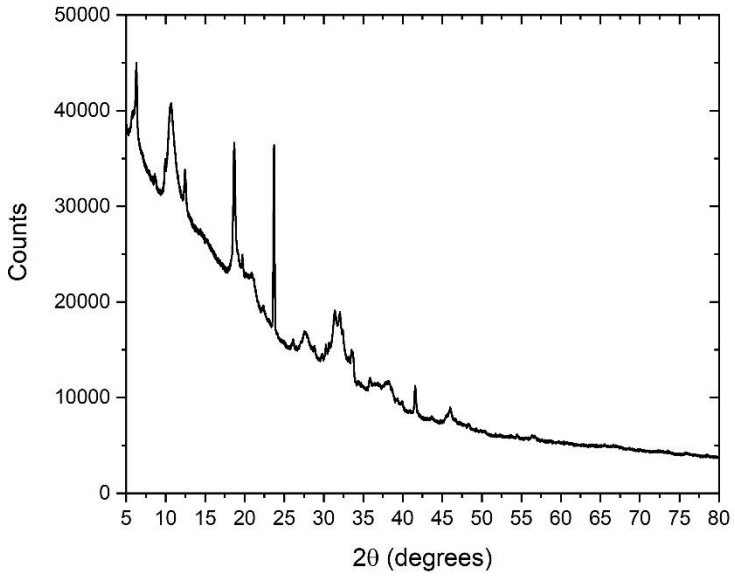

Figure 3.20: XRD pattern of K_3:*p*-terphenyl without background subtraction.

Figure 3.21 shows the XRD pattern of K_2:*p*-terphenyl, $K_{2.5}$:*p*-terphenyl, and K_3:*p*-terphenyl powders. Overall, the patterns are distinct and indicate each material is a unique phase. Notably, they all share a peak at 19° with neat *p*-terphenyl. This could indicate that the K_x:*p*-terphenyl samples all have a neat *p*-terphenyl in them from incomplete reduction of the terphenyl. However, this is contrary to the ATR-FTIR spectra, which reproducibly show that K_3:*p*-terphenyl no longer contains any un-reduced terphenyl. Alternatively, this peak could be a lattice plane that does not change as potassium intercalates in the material. If the doped structure is quasi two-dimensional, then the crystal plane between layers could be conserved as potassium is doped into the material.

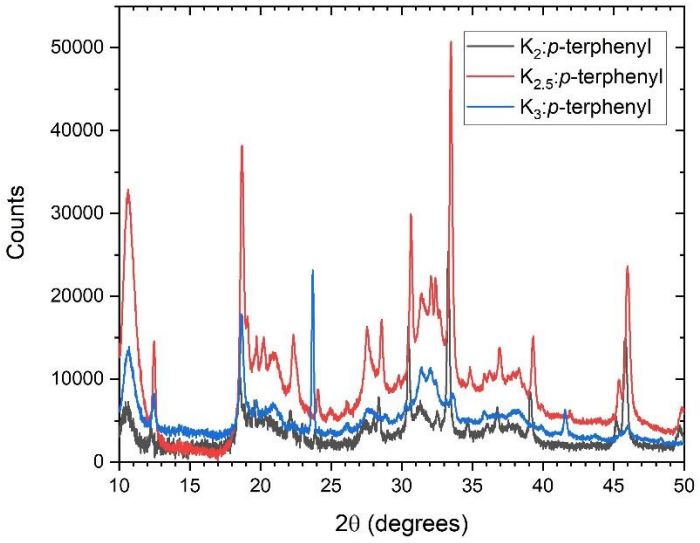

Figure 3.24: XRD pattern of K_2:*p*-terphenyl, $K_{2.5}$:*p*-terphenyl, and K_3:*p*-terphenyl after background subtraction.

The two intense peaks at 30.5° and 34.5° that appear in K_2:*p*-terphenyl and $K_{2.5}$:*p*-terphenyl are consistent with the crystal structure of potassium metal and indicate a pure potassium phase. This is consistent with ATR-FTIR of K_x:*p*-terphenyl at low doping levels, where neutral *p*-terphenyl is still observed. If *p*-terphenyl has not fully reduced, then there must be remaining potassium metal that has precipitated from solution as a distinct phase.

Neither the potassium peaks nor the *p*-terphenyl peaks consistently appear at all doping levels, indicating there are still variations in the material that do not manifest in the ATR-FTIR spectra. This means that, while the *p*-terphenyl consistently reduces to a dianion regardless of doping level, the crystal structure it forms with potassium can change.

Figure 3.22 shows the unnormalized XRD patterns of a K_3:*p*-terphenyl powder compared to a K_3:*p*-terphenyl sample compressed into a pellet. The peak

positions are consistent between each powder pattern, however the relative intensity of peaks are very different. This indicates that there are differences in the preferred orientation of crystallites in the powder and pellet samples. Pressing the material into a pellet seems to improve longevity of the sample during the XRD measurement, however it clearly influences the pattern measured in the experiment. This could mean the powder samples have degraded or there are other differences in the crystal structure of the material.

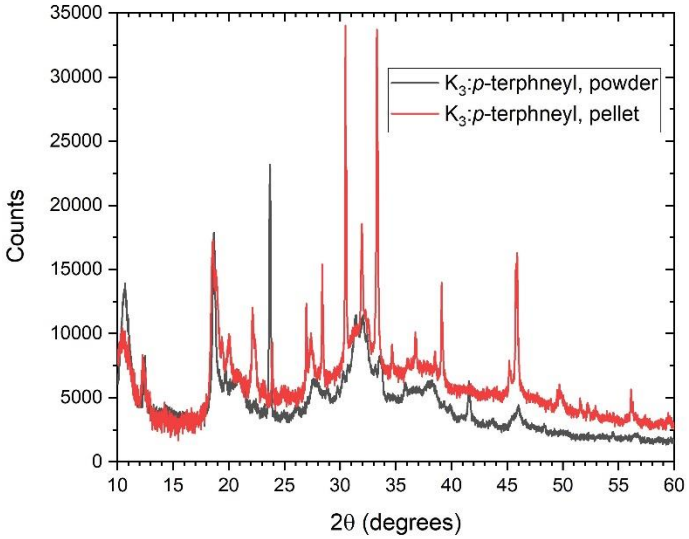

Figure 3.25: XRD pattern comparing a K_3:*p*-terphenyl as a powder with a K_3:*p*-terphenyl pressed into a pellet.

Figure 3.23 shows the XRD pattern of a K_3:*p*-terphenyl sample quenched by exposure to wet argon, breathing quality air, and by opening the air free sample holder to air. The low angle background of the air quench sample is different because of the difference in the refractive index of air compared to argon. As shown in the ATR-FTIR spectra of quenched samples, quenching produces a complicated mixture of products. The peaks seen in the air quenched sample are distinct from

those of the water and oxygen alone. The peak at 32.5° is not seen in any other K_x:*p*-terphenyl samples. Thus, its presence is a good indication of degradation of the sample from permeation of air into the air free sample holder.

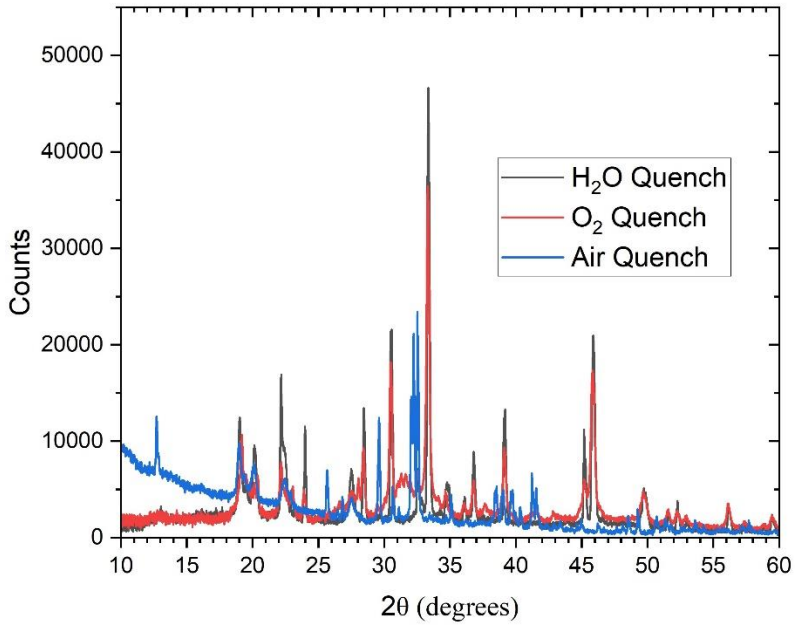

Figure 3.26: XRD pattern of a K_3:*p*-terphenyl sample quenched by various ways.

3.3.7 Conductivity of $K_{2.5}$:*p*-Terphenyl

The measured resistance between the middle electrodes of the $K_{2.5}$:*p*-terphenyl at room temperature was 72 Ω. The electrodes were 0.254 cm long and separated by 0.045 cm. The thickness of the sample was estimated to be 0.01 cm thick. As such, the resistivity of the sample at room temperature was 4 Ω cm. Figure 3.24 shows the resistivity of the sample as a function of temperature, showing that it increases monotonically to 153 Ω cm at 1.8 K. Breaks in the resistivity at 150 K and 50 K are caused by the change in rate of temperature change in the measurement. The sample was held at 1.8 K for 20 minutes, then

heated back to room temperature following the same curve as when decreasing temperature, indicating that the sample did not degrade during the measurement.

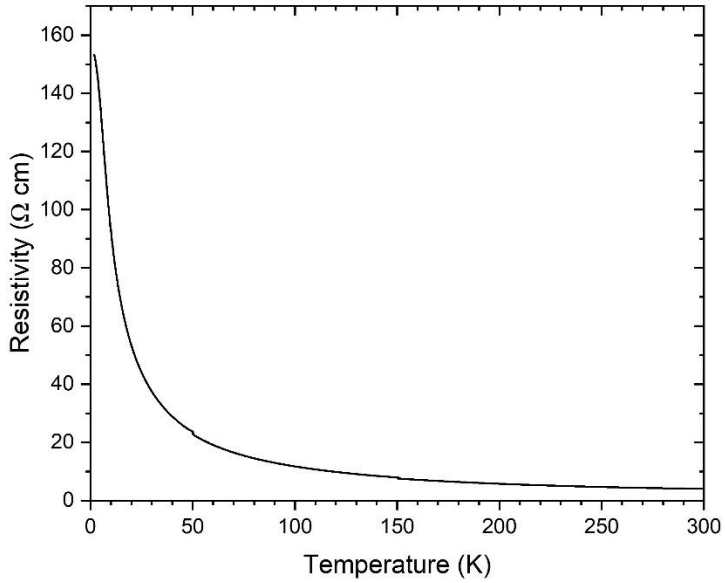

Figure 3.27: Resistivity of a $K_{2.5}$:*p*-terphenyl sample as a function of temperature.

An increase in resistivity with decreasing temperature is indicative of semiconducting and insulating behavior. This is contrary to what is seen in the literature, where samples with comparable resistivities at room temperature showed a decrease in resistivity with temperature, consistent with metallic behavior.[5,6] We attempted to fit the conductivity of the $K_{2.5}$:*p*-terphenyl with a variable range hopping model.[14] In this model, a plot of -lnσ will be linear with $T^{-\alpha}$, where $\alpha = 1/(1 + D)$ and D is the dimensionality of the carrier transport. Additionally, $\alpha = 1$ will show if the conductivity of the material has an Arrhenius activation energy. Figure 3.25 shows the variable range hopping plots for $\alpha = 1$ (Arrhenius), $\alpha = 2$ (one dimensional), $\alpha = 3$ (two dimensional), and $\alpha = 4$ (three dimensional). Figures 3.26 and 3.27 show the low temperature and high

temperature regions of each of the plots in Figure 3.25. The variable range hopping plots in Figures 3.25-3.27 do appear to become more linear with increasing dimensionality, but there are no temperature ranges where the linearity is unambiguous.

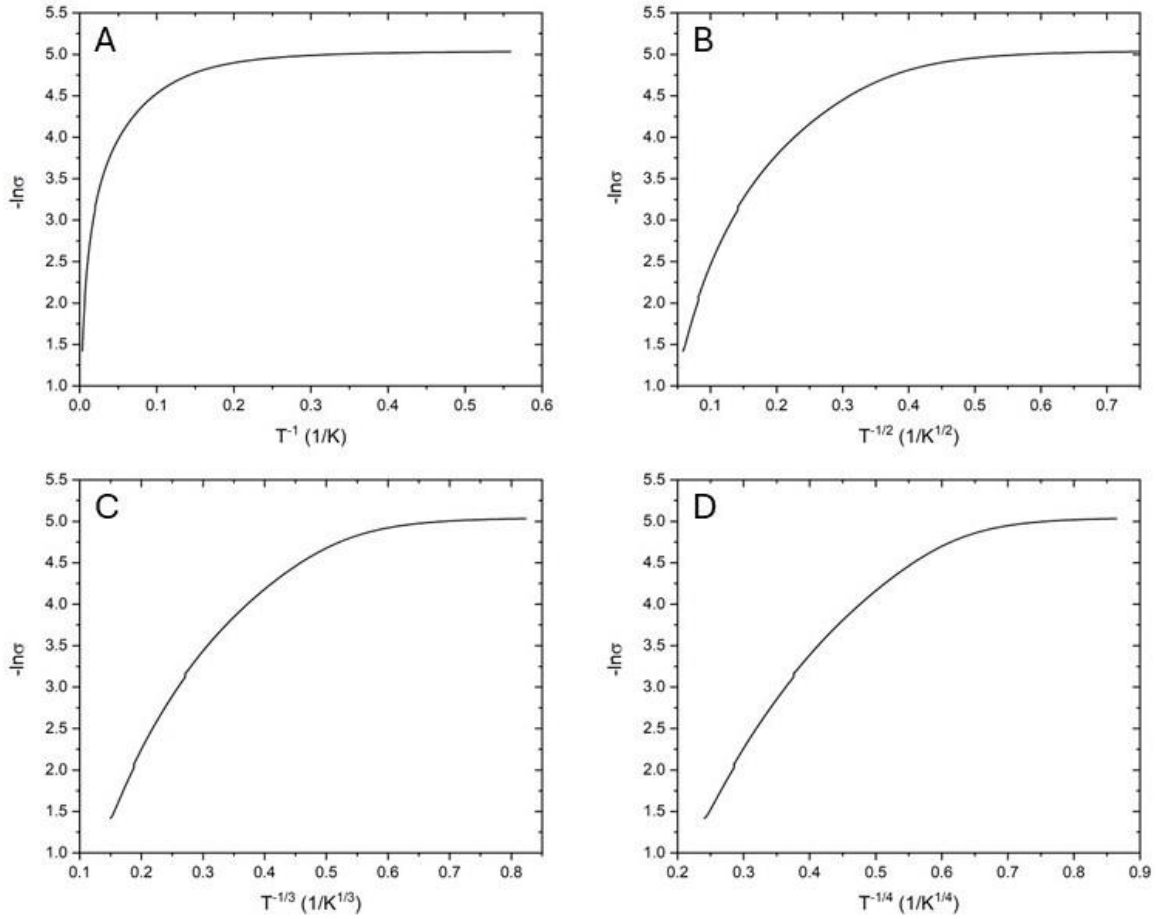

Figure 3.28: Variable range hopping plots of the conductivity of $K_{2.5}$:*p*-terphenyl. A) $\alpha = 1$, B) $\alpha = 2$, C) $\alpha = 3$, D) $\alpha = 4$.

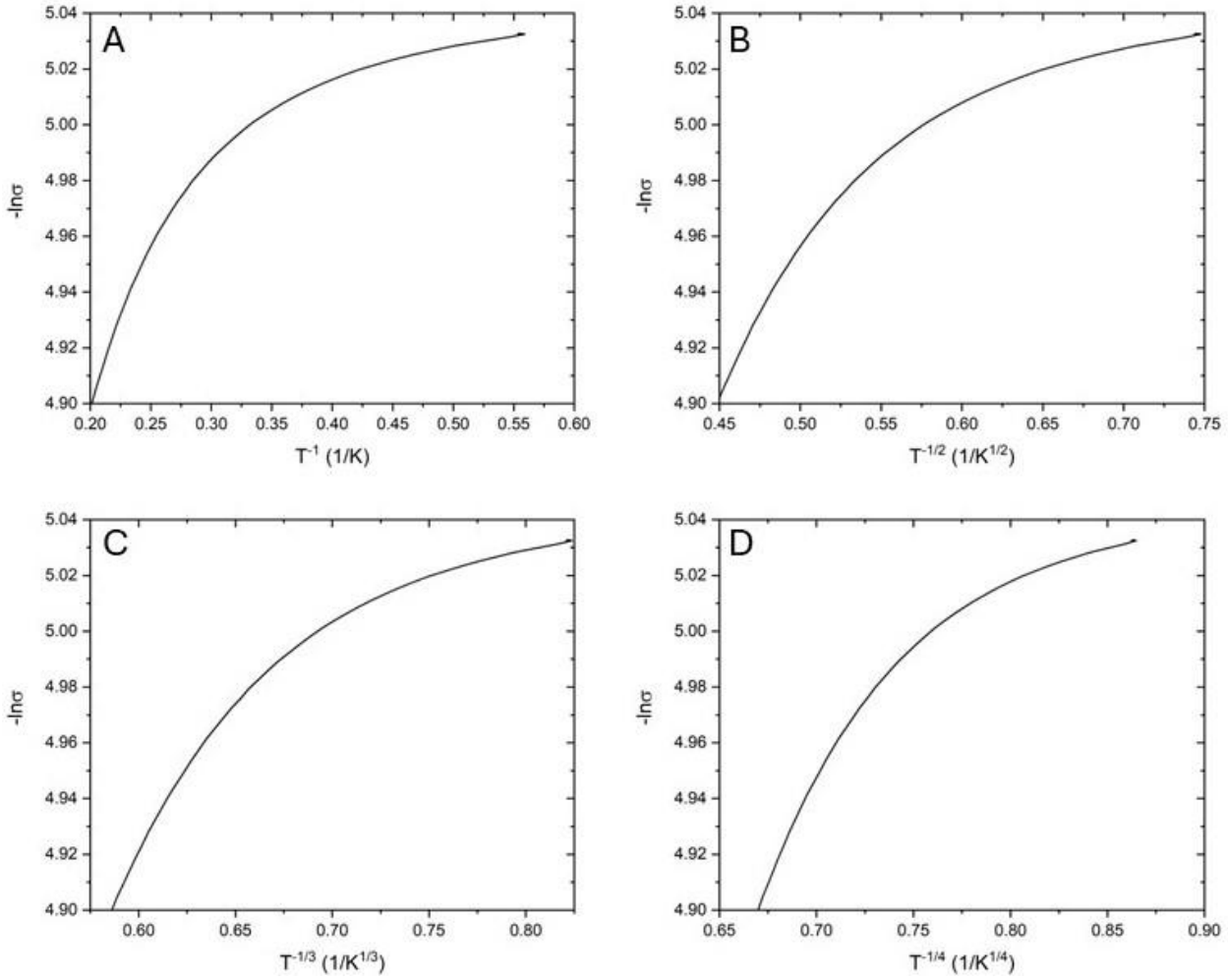

Figure 3.29: Low temperature variable range hopping plots of the conductivity of $K_{2.5}$:p-terphenyl. A) α = 1, B) α = 2, C) α = 3, D) α = 4.

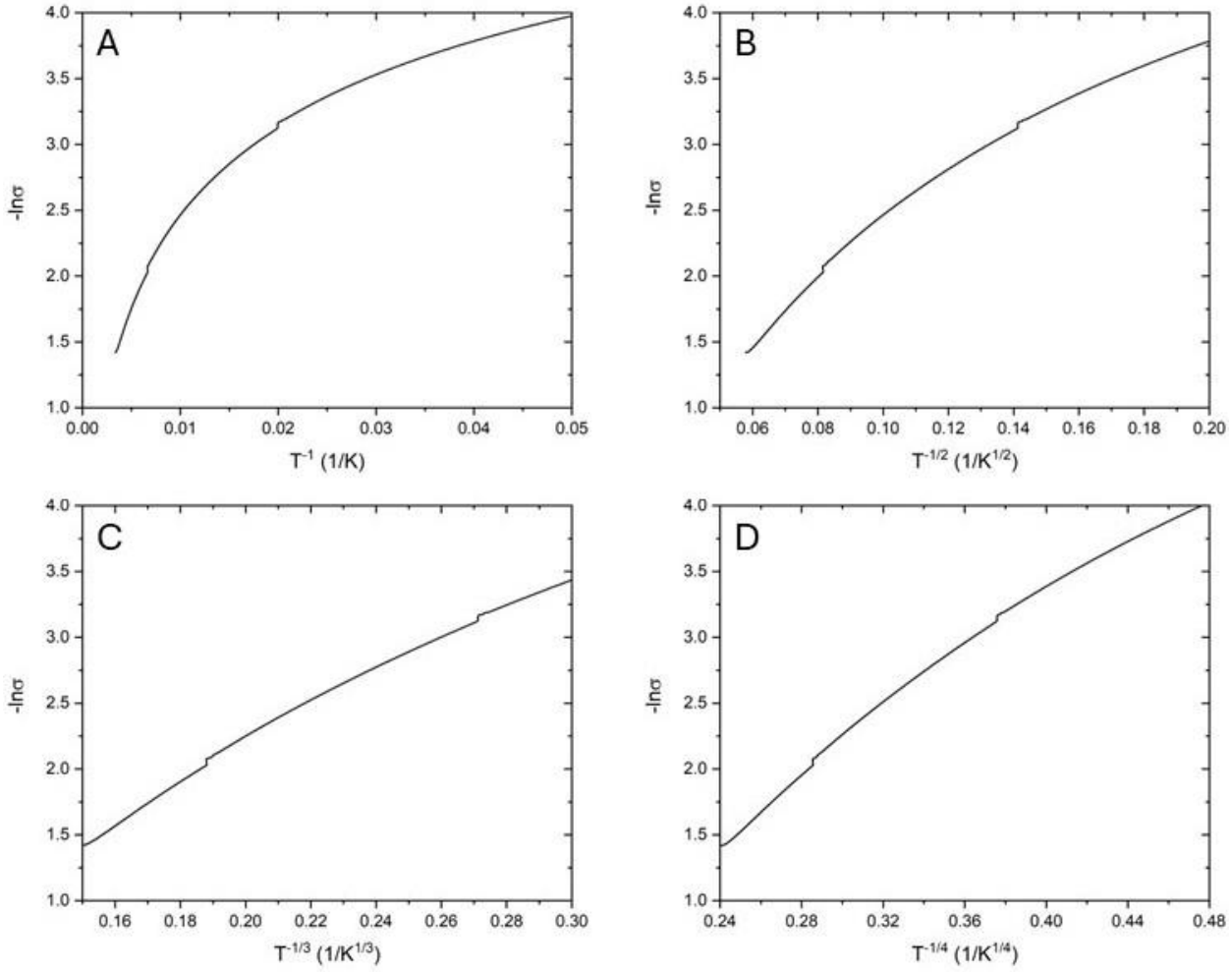

Figure 3.30: High temperature variable range hopping plots of the conductivity of $K_{2.5}$:*p*-terphenyl. A) α = 1, B) α = 2, C) α = 3, D) α = 4.

In contrast, Figure 3.28 shows the conductivity of the $K_{2.5}$:*p*-terphenyl sample vs temperature, which is unambiguously linear except for the range below 7 K and above 285 K, where we have concerns about the rate of temperature change of the instrument since it is near the stop/start portions of the scan. The R^2 of linear fits of this data is greater than 0.9999 over broad temperature ranges and only deviates below 7K and above 285 K. Currently we do not have a model to explain the linear dependence of the conductivity for any class of material.

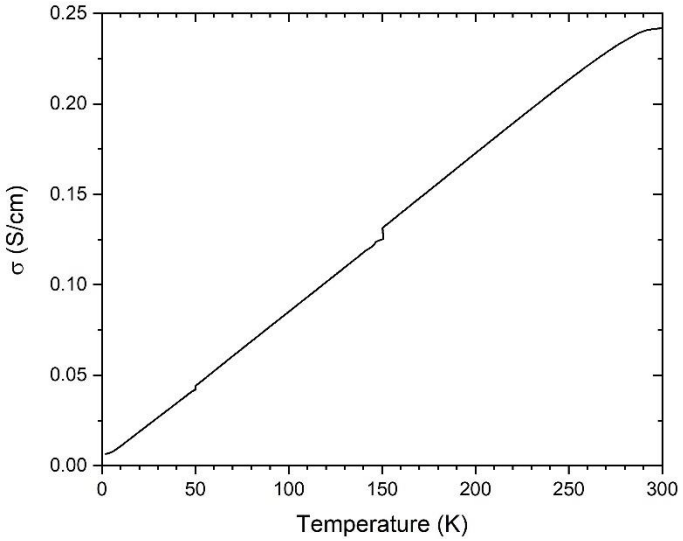

Figure 3.31: Conductivity of a K2.5:p-terphenyl sample as a function of temperature.

3.4 Conclusion

We have demonstrated a new procedure for synthesizing K_x:*p*-terphenyl with varying doping levels that avoids the high temperatures used for vapor grown materials. ATR-FTIR shows the reproducibility of the method and demonstrates the formation of the dianion of *p*-terphenyl at multiple doping levels. Degradation of the material in air does not produce *p*-terphenyl as a product. XRD characterization of the material remains challenging, and quantitative analysis of the patterns is ongoing. Initial conductivity measurements show that $K_{2.5}$:*p*-terphenyl is a semiconductor with an atypical linear trend of conductivity with temperature.

This is an ongoing study, and these results provide a strong starting point for the continued development of this method. Future work will focus on producing K_x:*p*-terphenyl samples for conductivity and quantitative XRD analysis. Efforts can be made to improve the crystallinity of the material by modifying the reaction and

deposition times. Additionally, this method can be applied to additional organic materials of interest to superconductivity, such as quaterphenyl and diphenylanthracene.

References

1. Symons, M. C. R. Solutions of Metals: Solvated Electrons. *Chem. Soc. Rev.* **1976,** *5,* 337-358.

2. Birch, A. J. The Birch Reduction in Organic Synthesis. *Pure & Appl. Chem.* **1996,** *68,* 553-556.

3. Rabideau, P. W. The Metal-Ammonia Reduction of Aromatic Compounds. *Tetrahedron* **1989,** *45,* 1579-1603.

4. Sakamoto, A.; Harada, T.; Tonegawa, N. A New Approach to the Spectral Study of Unstable Radicals and Ions in Solution by the Use of an Inert Gas Glovebox System: Observation and Analysis of the Infrared Spectra of the Radical Anion and Dianion of *p*-Terphneyl. *J. Am. Chem. Soc.* **2008,** *112,* 1180-1187.

5. Carrera, M.; McDonald, J. L.; Untiedt, C.; Garcia-Hernandez, F. M.; Verges, J. A.; Guijarra, A. Characterization of Main Phase in K_x*p*-Terphenyl and Its Largest Congener $K_x$poly(*p*-phenylene): A Report of Their Magnetic and Electric Properties. *J. Chem. Phys. C* **2019,** *123,* 5264-5272.

6. Pinto, N.; Di Nicola, C.; Trapananti, A.; Minicucci, M.; Di Cicco, A.; Marcelli, A.; Bianconi, A.; Marchetti, F.; Pettinari, C.; Perali, A. Potassium-Doped Para-Terphenyl: Structure, Electrical Transport Properties and Possible Signatures of a Superconducting Transition. *Condens. Matter* **2020,** *5,* 78.

7. Peres, L. O.; Spiesser, M.; Froyer, G. Reduction of *p*-Terphenyl, *p*-Quaterphenyl and *p*-Sexiphenyl Using Alkali Metal in Liquid Ammonia: Process and Characterization of the Reduced Compounds. *Synth. Met.* **2005,** *155,* 450-454.

8. Shriver, D. F.; Drezdzon, M. A. *The Manipulation of Air-Sensitive Compounds,* 2nd Ed; John Wiley & Sons: New York, 1986.

9. Neese, F. The ORCA Program System. *Wiley Interdiscip. Rev.: Comput. Mol. Sci.* **2012,** *2,* 73-78.

10. Bremond, E.; Savarese, M.; Su, N. Q.; Perez-Jiminez, A. J.; Xu, X.; Sancho-Garcia, J. C.; Adamo, C. Benchmarking Density Functionals on Structural Parameters of Small-/Medium-Sized Organic Molecules. *J. Chem. Theory Comput.* **2016,** *12,* 459-465.

11. Urban, M. W. *Attenuated Total Reflectance Spectroscopy of Polymers: Theory and Practice,* Polymer Surfaces and Interface Series; American Chemical Society: Washington, DC, 1996.

12. Fox, M. *Optical Properties of Solids,* 2nd Ed.; Oxford Master Series in Condensed Matter Physics; Oxford University Press: New York, 2010.

13. Rice, A. P.; Tham, F. S.; Chronister, E. L. A Temperature Dependent X-ray Study of the Order-Disorder Enantiotropic Phase Transition of *p*-Terphenyl. *J. Chem. Crystallogr.* **2013,** *43,* 14-25.

14. Nardes, A. M.; Kemerink, M.; Janssen, R. A. J.; Anisotropic Hopping Conduction in Spin-Coated PEDOT:PSS Thin Films. *Phys. Rev. B* **2007,** *76,* 085208.

CHAPTER 4

Ultrafast Dynamics of a [2 + 2] Photocycloaddition of an Orthocyclophane

4.1 Introduction

Scheme 4.1 shows the [2 + 2] photocycloaddition of an orthocyclophane, **1**, here called dibenzene, with the photoproduct **2**. The absorption spectrum of dibenzene is shown in Figure 4.1.

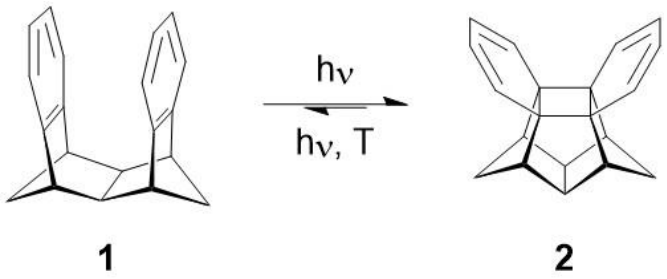

Scheme 4.1: Photocycloaddition of dibenzene, **1**, to the closed photoproduct, **2**.

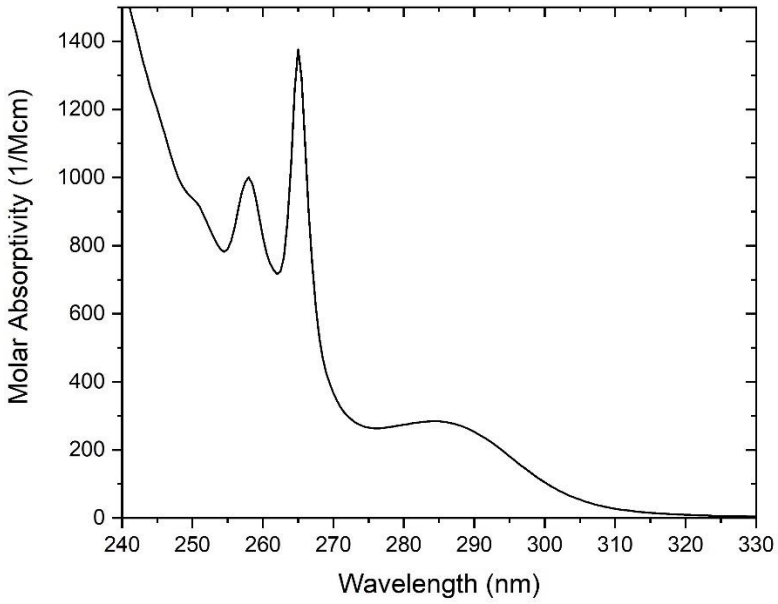

Figure 4.32: UV-Vis absorption spectrum of a solution of **1** in cyclohexane.

Previously, Joern Tonne[1] studied the photochemistry of this reaction for his PhD thesis. He found that the first singlet excited state of dibenzene, reached by

absorbing in the band centered at 285 nm, leads to an excimer-like excited state. Exciting at wavelengths below 265 nm excites to the S_2 state with the excitation localized on one of the benzene rings. When exciting to S_1, most of the excited state population then travels across the S_1 potential energy surface (PES) to the conical intersection that funnels to the ground state PES at a geometry half-way between the concerted reaction of **1** to **2**. The conical intersection is called the pericyclic minimum. From there, excited molecules can either return to the ground state dibenzene or form the photoproduct. At room temperature, the photochemical yield of **1** → **2** is 47% and the yield of **2** → **1** is 45%. At 98 K, the **1** → **2** yield decreases to 30%, indicating a barrier exists on the S_1 surface between the initially excited state and the pericyclic minimum. The absorption spectrum of the photoproduct rises sharply at 320 nm to 3200 1/Mcm and has a broad flat band extending past 250 nm, overlapping with the absorption spectrum of dibenzene and making quantification of these yields challenging.[2]

A small portion of excited dibenzene also fluoresces from the excimer minimum. The fluorescence band is centered at 357 nm with a room temperature quantum yield of 0.3%. At 77 K, the fluorescence quantum yield increases to 5.7%. The excited state lifetime measured by time correlated single photon counting (TCSPC) is 184 ps at room temperature and 28.9 ns at 77 K. Again, this indicates that there is a barrier between the excimer and the pericyclic minimum. Lowering the temperature decreases the probability of crossing over the barrier.

The quantum yield of fluorescence is constant with excitation wavelength when exciting to S_1, however when exciting to S_2, the quantum yield of fluorescence suddenly drops to 0.065%. Simultaneously, the photochemical quantum yield of **1** → **2** increases to 68%. Clearly some additional reaction path is present from the S_2 PES, but how the path manifest was not apparent at the time.

The role that the S_2 surface plays in the photocycloaddition of **1** to **2** is the focus of the present study. We use a novel femtosecond transient absorption experiment with pump and probe spectral regions in the UV that are not accessible with conventional TA experiments. This allows us to explore how the dynamics of the photocycloaddition change from excitation of S_1 to S_2. With this, we can describe a potential mechanism from the S_2 state, which can be explored more fully in future theoretical studies.

4.2 Materials and Methods

4.2.1 Femtosecond Transient Absorption Spectroscopy

The femtosecond transient absorption is described in detail elsewhere,[3] here we describe it briefly and emphasize some notable features of the experiment.

4.2.2 Femtosecond Laser

Femtosecond pulses were generated by a Clark-MXR CPA 2001 Ti:sapphire amplifier generating 850 μJ of 150 fs long pulses at 775 nm with 1 kHz repetition rate. A thin glass plate was used to split off a minimal fraction of the beam which was then directed into an array of neutral density filters and then photodiode, which was used to monitor the noise of the laser. The amplifier was optimized to

minimize the root mean square (RMS) noise. The RMS noise was below 0.6% and the pulse-to-pulse noise was less than 0.3%. The compression of the laser was optimized to maximize the visible output of the noncollinear parametric amplifier (NOPA). A beamsplitter was used to split 250 μJ from the fundamental for the pump beam. 1 μJ was separated from the remaining beam to generate the probe beam.

4.2.3 Pump Beam

Visible pump pulses were generated using a home-built two stage noncollinear optical parametric amplifier (NOPA).[4] The NOPA is a two-stage amplifier that produces 12 μJ of broadband green pulses centered at 520 nm or 580 nm, depending on the desired wavelength. The visible output of the NOPA was compressed using a dual prism compressor with prisms made of fused silica. The compressor contains a retroreflector in the path of the dispersed beam to minimize the footprint of the compressor. Compression can be optimized by adjusting the position of the retroreflector.

After the compressor, the visible pump pulses were frequency doubled in by focusing with spherical mirrors into a 57 μm thick BBO crystal cut at 45°. This was used to generate UV pulses centered at 260 nm and 290 nm, with energies at 400 nJ and 200 nJ, respectively, depending on the desired wavelength.

The pump beam was then routed through a mechanical delay stage and focused into the sample cell. A modular, home built UV autocorrelator was used to measure the pulse length of the UV pump pulses, and the compressor was adjusted

to minimize the pulse length, typically to 40 fs.[5] A beam camera (Ophir Optics) was placed in the sample position and used to optimize the shape and size of the focused pump beam to about a 100 µm by 100 µm circle. The camera was also used to monitor the alignment of the delay stage to minimize the drift of the pump beam to less than 10 µm through the length of the stage.

4.2.4 Probe Beam

The path of the probe beam is long to maintain temporal overlap of the pulses at the sample and the white light supercontinuum was generated as close to the sample as possible to minimize temporal dispersion of the pulse. The supercontinuum was generated by focusing the beam into a 5 mm thick CaF_2 plate in a home built motorized mount. The mount translated the CaF_2 in a circular path to prevent burning of the crystal at a frequency of about 1 Hz. This generated a supercontinuum pulse about 1 ps long and spanning about 285 nm to 720 nm.

To generate a UV supercontiuum probe, the fundamental was first frequency doubled to 388 nm using a BBO crystal. The frequency doubling was performed without focusing the fundamental into the crystal. A set of dichroic mirrors were then used to remove the residual 775 nm fundamental and direct the beam to the CaF_2 plate. This generated a continuum spanning 245 nm to 365 nm.

The probe beam was then split using a 1 OD neutral density filter. The reflected beam was used as the sample probe beam, and the attenuated beam was used as the probe reference. The sample probe beam was focused into the sample cell using spherical mirrors. The beam camera was used to ensure the focus of the

probe was spherical and about 50 µm by 50 µm. The beam was then recollimated with a spherical mirror and directed into a home-built spectrometer. The beam was dispersed with a prism and spectra were collected using a linear CCD array camera (EB Stresing). The reference beam was directed directly into a second identical spectrometer without going through the sample. The line cameras are fast enough to measure the spectrum of every pulse individually, allowing for single pulse referencing to minimize low frequency laser noise.[6]

After alignment of the probe beams, the spectra of a series of interference filters were recorded. These spectra were later used in the post-processing of the data to calibrate the camera pixels to specific wavelengths.

4.2.5 Sample Cell and Measurement

The probe and pump beams were spatially aligned at the focus of the probe beam before the sample was placed in the beam. To do this, a 50 µm pinhole aperture was mounted onto the sample holder and aligned to optimize transmission of the probe beam. Without moving the pinhole, the pump beam was then aligned through it, using a power meter to maximize the transmission of the beam. After alignment, an optical chopper was used to lower the pump repetition rate to 500 Hz. The polarization of the pump beam was set to the magic angle, 54.7°, relative to the probe beam using a broadband UV half-wave plate.

A custom-made flow cell was used to hold the sample. The flow cell had 200 µm path length fused silica windows and a 100 µm sample path length, to minimize the coherent artifact produced by the windows and solvent. This is particularly

important when probing in the UV with a UV pump, as the dominant feature of the coherent artifact is caused by two photon absorption of the windows and solvent. The pump for the flow cell (HNP-Mikrosysteme) uses an extremely low volume, requiring only 3 mL of total volume. The flow cell was purged with solvent 4 times before loading the sample solution.

After loading the sample, the delay stage of the pump beam was scanned to where a transient absorption signal appeared. After signal appears, the alignment of the pump was optimized to maximize the transient signal. T_0 of the experiment was then defined as the middle of the rise of the transient signal at the center wavelength of the probe spectrum.

Samples were run scanning the delay from -10 ps to 1500 ps. 100 data points were taken for each range of data: -10 ps to -1 ps, -1 ps to 1ps, 1 ps to 10 ps, and 100 ps to 1500 ps. Data was collected using single pulse referencing. That is, a sample and reference probe pulse was measured simultaneously and divided. Every other pump pulse was blocked by the optical chopper, so that a reference probe spectrum with the pump on was divided by the probe spectrum with the pump off to measure the change in absorbance. For every time step, this was done for 500 sets of pulses and averaged. Each scan of time steps was repeated 3 times when using the visible supercontinuum probe and 5 times when using the UV supercontinuum probe. After running the scans, the flow cell was purged 4 times with fresh solvent, then transient absorption data was collected from -1 ps to 1 ps of the neat solvent to measure the coherent artifact of the pump and probe overlap.

4.2.6 Sample Preparation

Optics grade cyclohexane (Sigma Aldrich) was used as a solvent. Dibenzene was diluted to 34.5 mM for transient absorption. The UV-Vis absorption spectrum the sample was measured before and after each experiment to ensure no additional photoproducts formed.

4.2.7 Post-Processing

The data were processed in several ways before kinetic analysis was performed. First, each scan was assessed to ensure no scans had significant changes in the noise or signal of the sample, indicating an issue with the laser or degradation of the sample. Scans without issue were averaged. Then, the coherent artifact of the neat solvent spectra was fit to a polynomial to generate a chirp function for the temporal dispersion of the probe pulse. The chirp function was then applied to the sample data so that T_0 was zero for each wavelength of the spectrum. Then, the spectra of interference filters were compared to the known standard spectra of the filters to convert the pixel number to wavelength. Lastly, the data were converted from intensity to optical density.

4.2.8 Data Analysis

Spectral bands in the TA spectra were first fit with multiple exponential decays using Origin Pro. Global Analysis of complete spectral bands was performed using Glotoran.[7]

4.3 Results and Discussion

4.3.1 Excitation to S_1

The TA profile when exciting with a 290 nm pump and visible probe is shown in Figure 4.2. The color scale shows change in optical density (ΔOD), with yellow positive change in absorption and dark blue negative change in absorption. Zero signal is light blue. Wavelengths below 300 nm are obscured by scattering from the pump beam. The coherent artifact caused by nonlinear interactions of the pump and probe pulses can be seen near zero time delay and is particularly intense below 400 nm.[8] Two broad excited state absorption (ESA) bands are present, one below 400 nm that extends into the UV below the probe spectrum, and one spanning the visible between 430 nm and 650 nm. The structure in the spectrum at 640 nm and 670 nm are artifacts of the camera and are present in that region of pixels for all TA spectra.

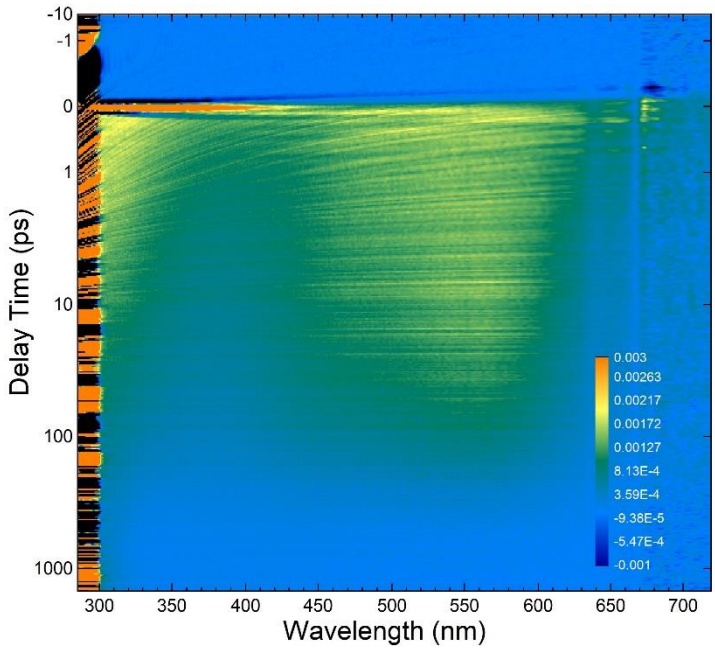

Figure 4.33: Transient Absorption profile of dibenzene in cyclohexane at room temperature with a 290 nm pump and visible probe. The color scale shows optical

density. Light blue is zero ΔOD, dark blue is negative ΔOD, and green to yellow is positive ΔOD.

The visible ESA band was previously seen in picosecond transient absorption measurements of dibenzene and is consistent with S_1 to S_n ESA bands typically seen in the transient absorption of excited dimers (excimers) of benzene solutions.[1] Spectra of the band at different delay times are shown in Figure 4.3.

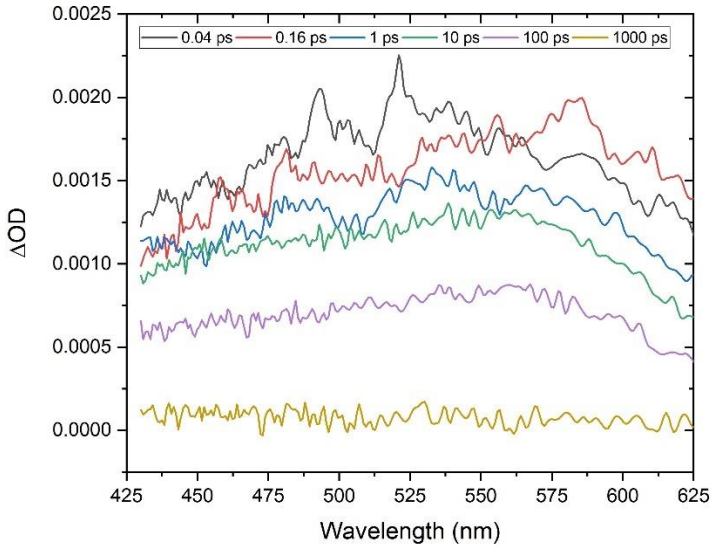

Figure 4.34: TA spectra of the visible ESA band in dibenzene in cyclohexane at various time delays.

The spectrum is particularly noisy at early times, and after the first 0.1 ps the spectrum monotonically decays to a flat baseline. A 540 nm wavelength slice of the band was fit to a multiple exponential decay, shown in Figure 4.4, with three time constants: 0.249 ps, 15.3 ps, and 186 ps. Previous measurements of the excited state lifetime of dibenzene using time correlated single photon counting and picosecond TA spectroscopy found the excited state lifetime of dibenzene to be 184 ps.[1] Therefore, we interpret the 186 ps time constant to correspond to lifetime of the

excimer, limited by fluorescence and internal conversion from the excimer minimum to the ground state of dibenzene. The 0.249 ps time constant is likely corresponds to vibrationally relaxation from the initially excited S_1 state to the relaxed excited state at the excimer. The 15.3 ps time constant could also be vibrational relaxation, however as we'll see later this likely corresponds to the average time for dibenzene to cross the barrier from the excimer minimum to the pericyclic conical intersection. To explore this further, we measured TA spectra with a probe deeper in the UV.

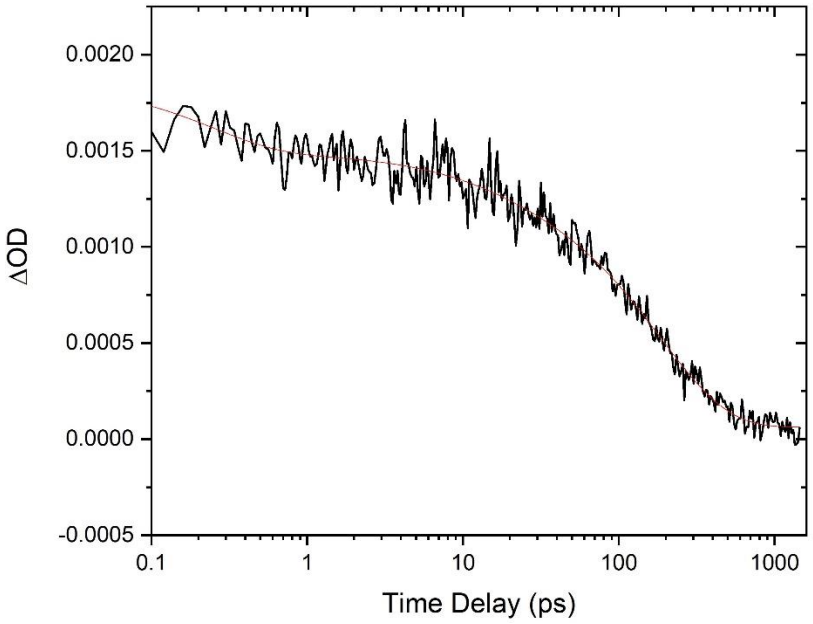

Figure 4.35: TA as a function of delay time of dibenzene at 540 nm of with 290 nm pump. The red curve is a multiexponential fit with time constants: 0.249 ps, 15.3 ps, and 186 ps.

Figure 4.5 shows the transient absorption spectrum of dibenzene excited with a 290 nm pump and probed with a UV probe generated by frequency doubling the laser fundamental before supercontinuum generation. The color scale again has dark blue showing negative ΔOD and green to orange showing positive ΔOD. Zero

ΔOD is light blue. The coherent artifact is ten times more intense than the TA signal from the dibenzene and obscures the first 160 fs of the transient spectrum. Wavelengths below 255 nm are particularly noisy from the low intensity of the probe signal in that region.

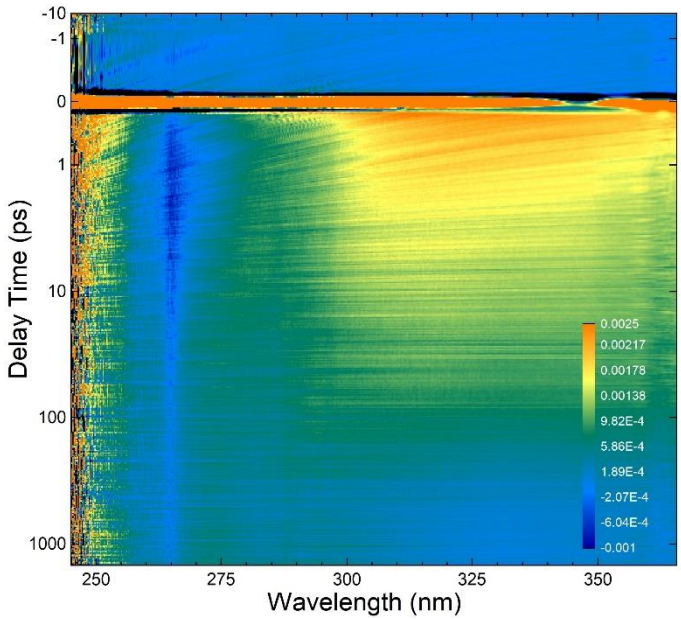

Figure 4.36: TA profile of dibenzene with 290 nm pump and UV probe. The color scale shows the change in optical density of the sample. Zero ΔOD is light blue, positive ΔOD moves from green to orange. Negative ΔOD is dark blue.

In Figure 4.5, the UV ESA band seen in Figure 4.2 extends deeper into the UV until it overlaps with a negative ΔOD signal at 265 nm. This negative signal is the ground state bleach (GSB) from the strong absorption band in dibenzene at the same wavelength. Additionally, a broad, weak positive signal can be seen below 300 nm at long delay times.

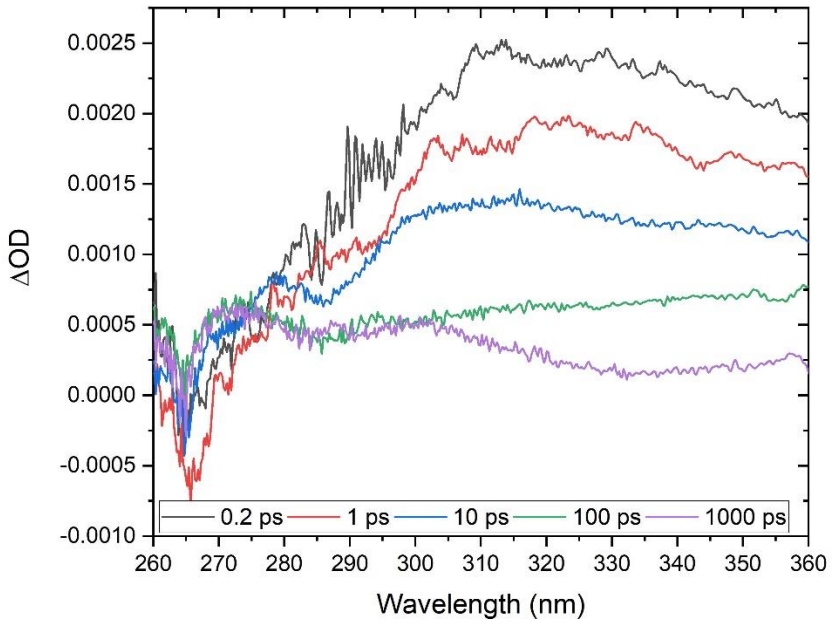

Figure 4.37: Transient absorption spectra at specific delay times of dibenzene with 290 nm pump and UV probe.

The TA spectra at long delay times are illustrated more clearly in Figure 4.6. The 290 nm region of each spectrum is noisy from scattering from the pump beam. The spectrum at 1000 ps is reminiscent of the absorption spectrum of the photoproduct of the cycloaddition reaction. Like an ESA feature, the absorption from the ground state of a species formed by excitation with the pump pulse will also appear as a positive TA signal. Additionally, any dibenzene that converts to the photoproduct will cause a negative GSB signal at long delay times. Since the excimer decays with a 186 ps time constant, the only TA signal present at 1000 ps should be from the photoproduct absorption and the decrease in dibenzene absorption.

Fitting the kinetics of species with overlapping transient bands is not possible with single-line fits alone, therefore we used global analysis of the UV TA

spectrum simultaneously. Figure 4.7 shows the decay associated difference spectra (DADS) of the UV probe data with a four component fit. To remove the influence of the coherent artifact, the fit was performed after cropping out the first 160 fs of the spectrum. The first three time constants, 0.563 ps, 6.74 ps, and 183 ps, are consistent with the three time constants from the single-line fit of the visible ESA band: an initial sub-picosecond vibrational relaxation, an intermediate time constant ~10 ps of the excited state population passing from the excimer minimum to the pericyclic minimum, and a ~180 ps time constant from fluorescence and internal conversion of the excimer back to the dibenzene ground state. The final time constant is labelled infinite because this spectrum decays with an unphysically long time constant, 3500 ps, which is more than twice the longest measured delay time for this experiment, meaning this feature is essentially constant as a function of time.

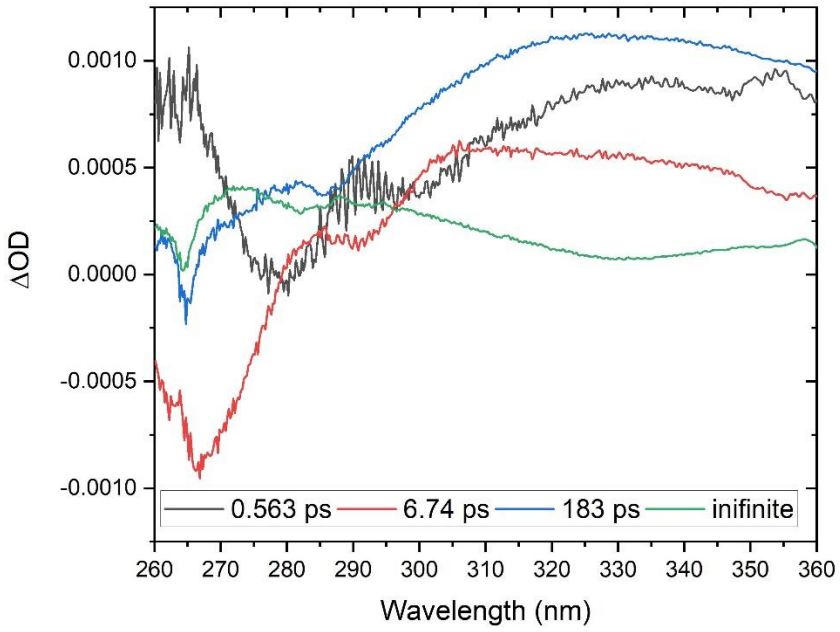

Figure 4.38: Decay Associated Difference Spectra of the TA spectrum of dibenzene with 290 nm pump and UV probe.

The initial fast 0.563 ps DADS has no ground state bleach feature in it at 265 nm, suggesting it is a process that occurs only in the excited state, consistent with vibrational relaxation. It has two broad positive features, showing that the ESA band in the UV TA spectra is actually two bands, one spanning about 290 nm to 400 nm, and the other from about 270 nm, stretching deeper into the UV. The intermediate 6.74 ps DADS shows both the UV ESA band and the majority of the GSB bleach signal. This indicates that the majority of the GSB decays with the 6.74 ps time constant. The DADS with 184 ps time constant also contains the ESA band and a small portion of the GSB signal. Since 45% of dibenzene excited to S_1 returns to the dibenzene ground state, while the fluorescence quantum yield is 0.3%, it is consistent that most the change in the GSB spectrum occurs on the 6.74 ps timescale. Lastly, the DADS with infinite time constant is resembles the

photoproduct absorption spectrum, though it is somewhat distorted by scattering from the pump beam.

Figure 4.8 is a PES diagram that summarizes these dynamics. Arrow A shows the initial sub picosecond vibrational relaxation to the excimer minimum. Arrow B shows crossing over the barrier from the excimer minimum to the pericyclic conical intersection that occurs on a ~10 ps timescale. Arrow B shows the decay of the excimer via fluorescence that occurs with a 180 ps time constant. It is consistent with the PES surface drawn by Joerne Tonne in his thesis[1], however he was not able to resolve the ultrafast dynamics we've observed.

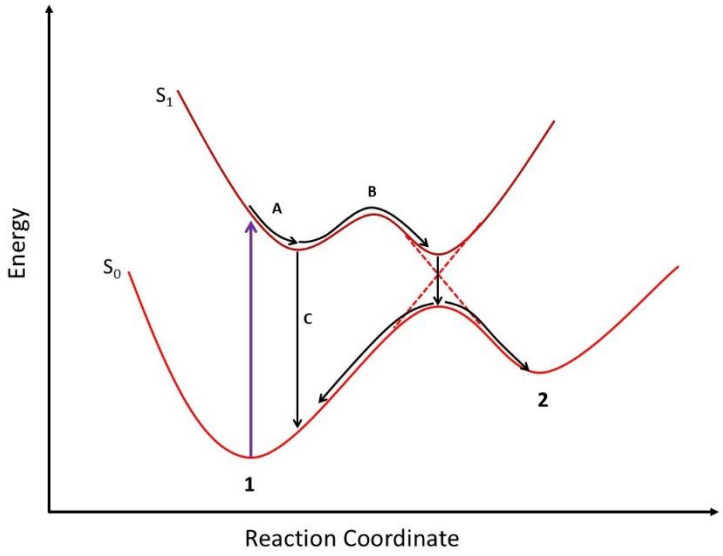

Figure 4.39: Ground and S_1 potential energy surfaces of the dibenzene and its photoproduct.

4.3.2 Excitation to S_2

The TA spectrum of dibenzene excited to the S_2 state with a 260 nm pump and visible probe is shown in Figure 4.9. It has the same ESA features seen when exciting to S_1 and there are no additional ESA bands from the S_2 state. Therefore, the features in the TA spectrum must be from the S_1 state after internal conversion (IC) from S_2.

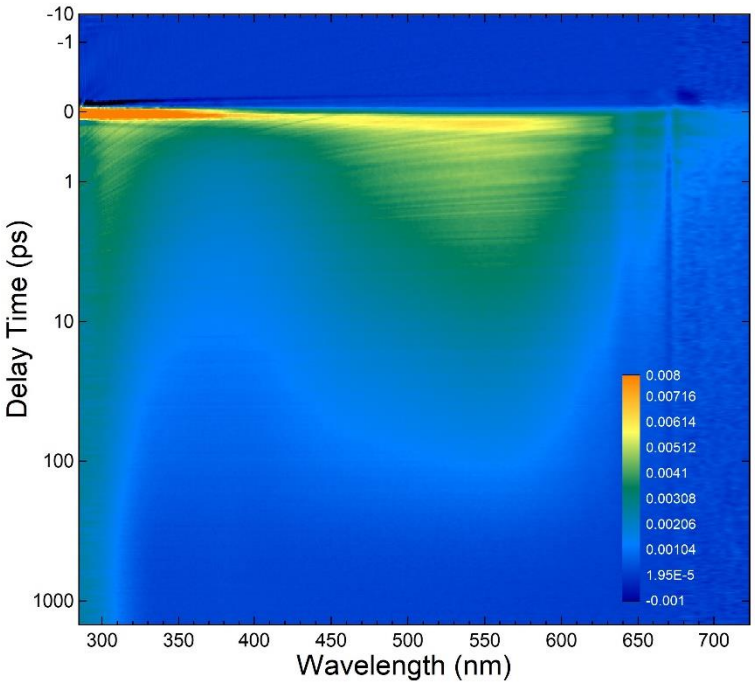

Figure 4.40: TA profile of dibenzene with a 260 nm pump and visible probe. The color scale shows optical density. Blue is zero ΔOD, dark blue is negative ΔOD, and green to orange is positive ΔOD.

Figure 4.10 compares the transient absorption of dibenzene at 540 nm when pumping at 260 nm vs 290 nm. The rise time of the absorption when pumping with 260 nm pulses is considerably longer than when pumping with 290 nm pulses, resulting in the peak absorption being delayed by 120 fs. This indicates that after excitation to S_2, it takes 120 fs to internally convert to the S1 state.

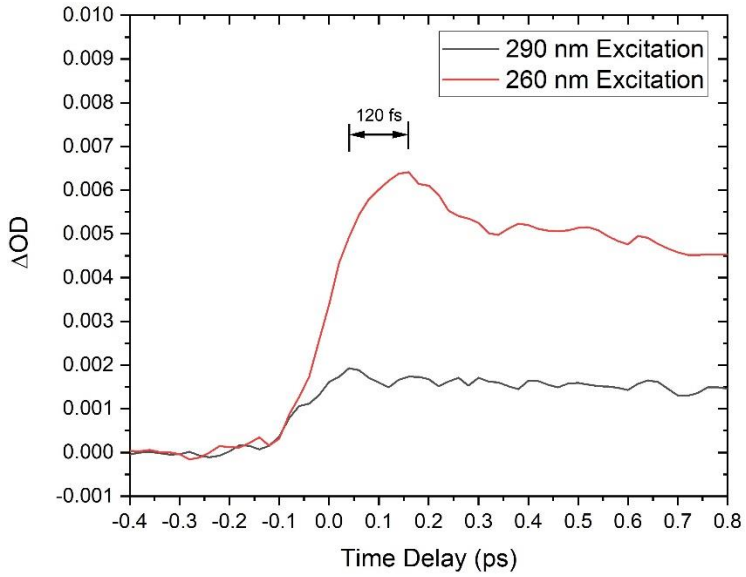

Figure 4.41: Comparison of the TA rise time of the ESA at 540 nm when exciting with 290 nm vs 260 nm.

After IC from S_2 to S_1, the kinetics of the visible ESA band are the same as when exciting directly to S_1. Figure 4.11 shows the fit of the TA at 540 nm with multiple exponential decays when pumping with 260 nm pulses. The trace is fit to a three exponential decay with the time constants 0.396 ps, 6.85 ps, and 156 ps. Just as with excitation directly to S_1, we can interpret these as an initial fast vibrational relaxation, the average time it takes to cross the barrier from the excimer minimum to the pericyclic minimum, and the lifetime of the excimer fluorescence directly to the dibenzene ground state, respectively. The lifetime of the excimer is shorter than when exciting directly to the S_1. This is possibly because IC from S_2 leaves the population higher on the S_1 PES than direct excitation does. This lets it access more and higher energy vibrational modes that improve the Franck-Condon overlap between the S_1 and S_0 states.

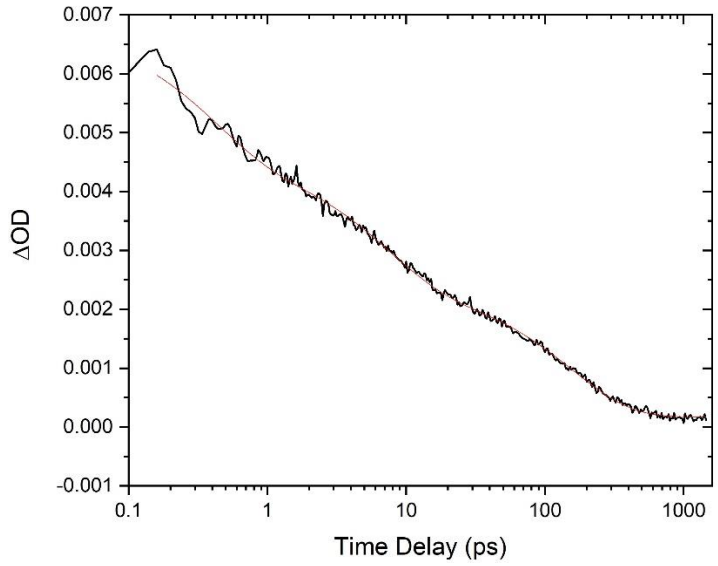

Figure 4.42: Multiple exponential fit of the visible ESA at 540 nm when using 260 nm pump.

Figure 4.12 shows the TA profile of dibenzene with 260 nm pump and UV probe. Superficially it is also very similar to excitation directly to the S_1 state. Again, the coherent artifact obscures the first 0.180 ps of the spectrum. There are also the same ESA bands in the UV, GSB at 265 nm, and positive TA signal at long time delays associated with the photoproduct absorption. Figure 4.13 shows the TA spectra with 260 nm pump and UV probe at different delay times. The early time spectra with 0.2 ps and 1 ps delay times have an additional shoulder between 270 nm and 290 nm not seen when exciting directly to S_1 that was shown in Figure 6. This suggests that the photoproduct forms at early delay times when exciting to S_2, before the ~7 ps it takes to cross over the barrier from the excimer minimum to the pericyclic funnel.

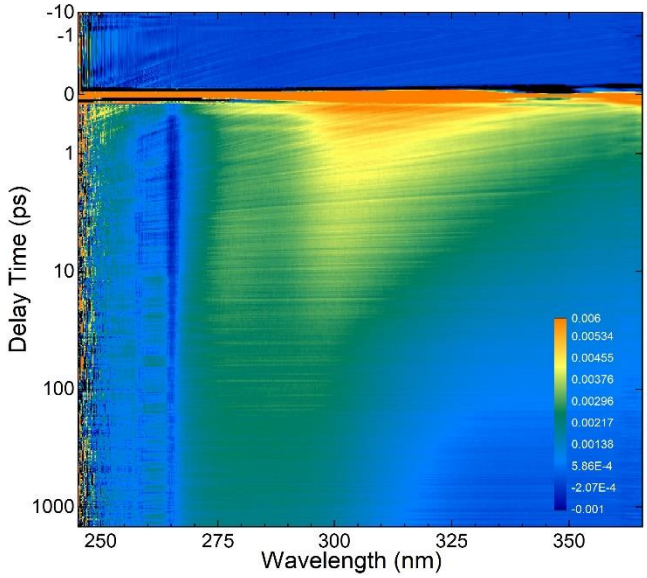

Figure 4.43: TA profile when dibenzene with a 260 nm pump and UV probe. The color scale shows optical density. Blue is zero ΔOD, dark blue is negative ΔOD, and green to orange is positive ΔOD.

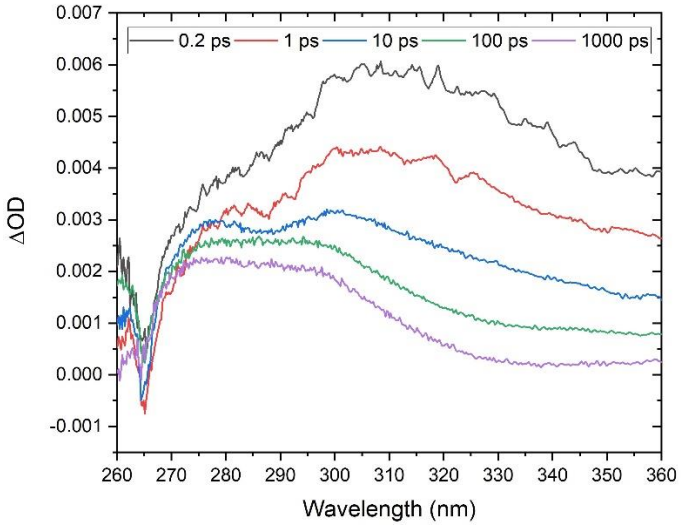

Figure 4.44: TA spectra of dibenzene at different delay times with 260 nm pump and UV probe.

The DADS when exciting to S_2, shown in Figure 4.14, is also similar to the DADS when exciting directly to S_1. There is a broad, fast sub-picosecond decay with

0.432 ps time constant. The intermediate decay with 7.68 ps time constant shows both the UV ESA band and GSB and is associated with the time it takes to cross the barrier from the excimer minimum to the pericyclic minimum. There is an intermediate decay with 138 ps time constant associated with the excited state lifetime of the excimer. Lastly, the infinite time constant associated with the absorption of the photoproduct.

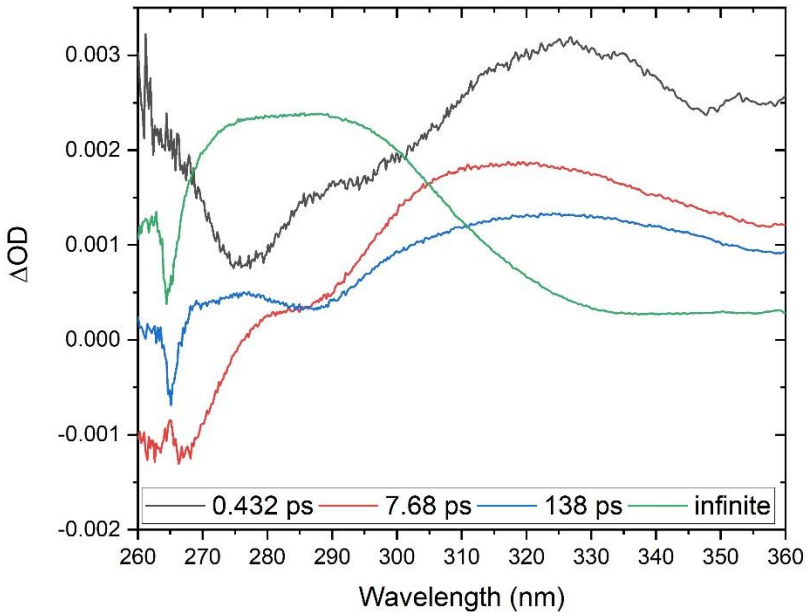

Figure 4.45: Decay associated difference spectra of the TA spectrum of dibenzene when exciting with a 260 nm pump and UV probe.

To explore the formation of the photoproduct at early times, global analysis was performed with a sequential kinetic model. DADS arise from a parallel model, showing the spectral component of the TA spectrum that simultaneously decays with a specific time constant. A sequential model generates evolution associated difference spectra (EADS) that correspond to the spectra of species that form and decay sequentially with that time constant. If a species that forms with a fast time

constant persists through the longer delay times of the experiment (for instance, if it is absorption from the ground state of a photoproduct), the spectrum of that species will be visible in all later EADS.

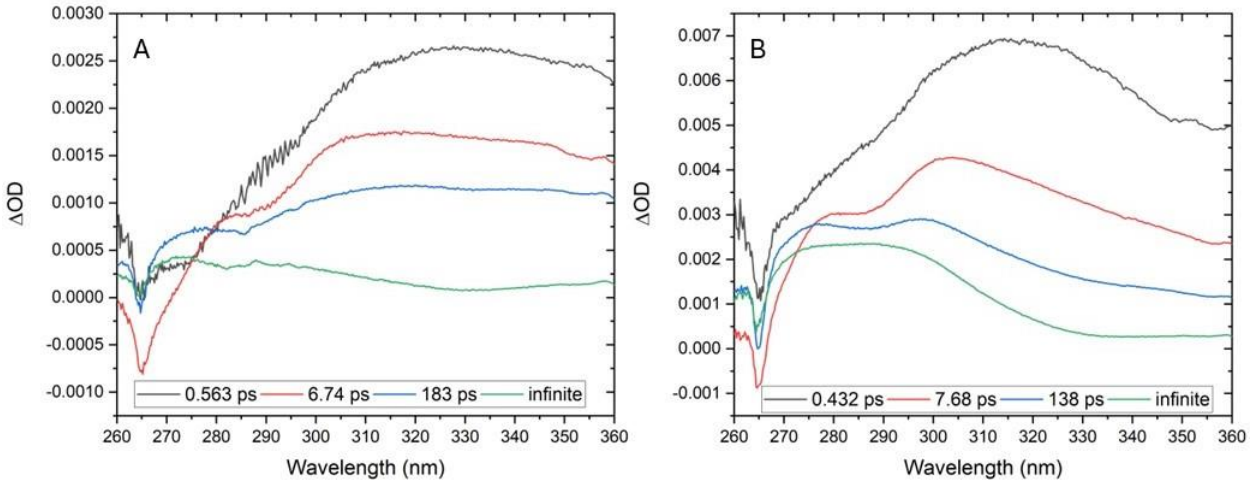

Figure 4.46: Evolution associate difference spectra of the TA spectrum of dibenzene with A) 290 nm pump and B) 260 nm pump.

The EADS of dibenzene with different pump wavelengths are shown in Figure 4.15. With each subsequent EADS, we see additional decay of the UV ESA band and GSB and cumulative formation of the photoproduct. However, the sub-picosecond EADS in Figure 4.15 B for the 260 nm pump has a shoulder between 270 nm and 280 nm that is not present in Figure 4.15 A for the 290 nm pump. The presence of this additional shoulder shows that the photoproduct forms on a sub-picosecond timescale when exciting to S_2 and competes with internal conversion back to the S_1, consistent with what is seen in the qualitative analysis of the early time TA spectra in Figure 4.13.

The formation of the photoproduct on a sub-picosecond timescale is a startling result. Currently, there is no detailed understanding of the excited states

involved in the photocycloaddtion of dibenzene. No high-level quantum chemistry calculations have been performed on dibenzene, the photoproduct, and along the reaction path. However, drawing from the literature of other photocycloadditions, we propose that the ultrafast dynamics arise from coupling of the S_2 state with the D state through a process similar to singlet fission.

It is well known from state correlation diagrams of photocycloadditions that the doubly excited D state correlates through the pericyclic minimum to the product of the photocycloaddtion.[9] Yet, the D state is not directly accessible from the ground state via a single electron excitation.[10] That said, it is also known that the excited states of polyenes and benzene are multiconfigurational in nature, and doubly excited states do contribute to the overall electronic structure.[11,12]

However, models of photocycloadditions show that the D state is a triplet-triplet annihilation state.[13,14] In these earlier papers, the dimerization of H_2 to a cyclic H_4 was used as a model system, and it was shown that in the D state, each H_2 reactant was in a triplet excited state, each of which was coupled into and overall singlet state (Michl 1994). The coupled triplet has also been expanded to describe the D state for the photocycloaddition of pi electron systems.[15] For instance, triplet sensitization experiments show that triplet-triplet annihilation in anthracene can form a dimer formed by photocycloaddition.[16]

Singlet fission is the process where a singly excited chromophore (S_1) couples to an adjacent ground state chromophore (S_0) to form a singly excited coupled triplet state (^{1}TT).[17] To complete the fission, the coupled triplet state then dissociates to

two uncoupled triplets ($T_1 + T_1$). Much work has been done to study singlet fission in several chromophore systems, including rigidly coupled acenes that resemble the bridge seen in dibenzene.[18] To the best of our knowledge, singlet fission has never been observed in benzene.

We propose that the ultrafast photocycloaddition of dibenzene occurs through a singlet fission like process. When exciting to S_2, some amount of the population internally converts down to S_1 and photochemically is identical to direct excitation to the S_1 state. The remaining population in S_2 undergoes the first step of singlet fission to the coupled triplet state ^{1}TT that is the D state in the photocycloaddition. The D state is correlated to the photoproduct and travel down the surface yields the photoproduct in sub-picosecond timescales. This process would be the first instance of a singlet fission-like process occurring with a benzene dimer. The PES of this process is illustrated in Figure 4.16.

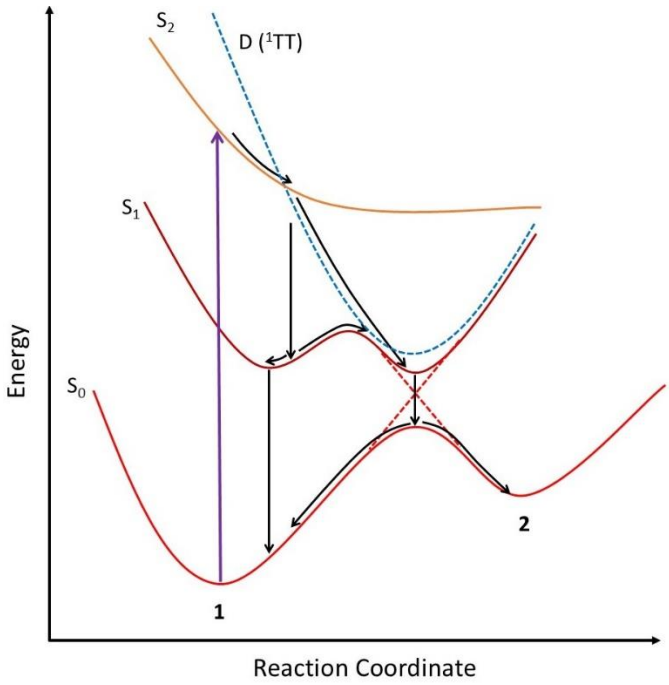

Figure 4.47: Potential energy surfaces of the proposed mechanism for photocycloaddition from S_2.

4.4 Conclusion

The dynamics of the photocycloaddition of dibenzene has been studied by ultrafast transient absorption spectroscopy. When exciting directly to S_1, dibenzene rapidly forms an excimer. The dibenzene can then cross over the barrier to the pericyclic funnel and undergo the photocycloaddition. When exciting to S_2, the dibenzene can internally convert to S_1 and undergo the usual dynamics, or it can form the photoproduct directly on a sub-picosecond timescale. We propose that this process happens through a singlet fission like mechanism, where the S_2 state converts to a coupled triplet state that is correlated to the photoproduct.

To fully understand this mechanism, multiconfigurational computational chemistry calculations should be performed at multiple steps along the reaction

pathway. These would elucidate which configurations contribute to the S_2 state, how the state couples to a doubly excited state, and the energies of these states along the reaction path.

References

1. Tonne, J. The Mechanism of an Unusual Benzo/Benzo Photocycloaddition Reaction. Ph.D. Thesis, Albert Ludwig University of Freiburg, Germany, 2001.

2. Tonne, J.; Prinzback, H.; Michl, J. Double Actinometry for Rigorous Evaluation of Quantum Yields of Clean Photoreversible Photochemical Reactions. *Photochem. Photobiol. Sci.* **2002,** *1,* 105-110.

3. Megerle, U.; Pugliesi, I.; Schriever, C.; Sailer, C. F.; Riedle, E. Sub-50 fs Broadband Absorption Spectroscopy with Tunable Excitation: Putting the Analysis of Ultrafast Molecular Dynamics on Solid Ground. *Appl. Phys. B* **2009,** *96,* 215-231.

4. Riedle, E.; Beutter, M.; Lochbrunner, S.; Piel, J.; Schenkl, S.; Sporlein, S.; Zinth, W. Generation of 10 to 50 fs Pulses Tunable Through All of the Visible and NIR. *Appl. Phys. B* **2000,** *71,* 457-465.

5. Homann, C.; Krebs, N.; Riedle, E. Convenient Pulse Length Measurement of Sub-20-fs Pulses Down to the Deep UV via Two-Photon Absorption in Bulk Material. *Appl. Phys. B* **2011,** *104,* 783.791.

6. Bradler, M.; Riedle, E. Temporal and Spectral Correlations in Bulk Continua and Improved Use in Transient Spectroscopy. *J. Opt. Soc. Am. B* **2014,** *31,* 1465-1475.

7. Snellenburg, J. J.; Laptenok, S. P.; Seger, R.; Mullen, K. M.; van Stokkum, I. H. M. Glotoran: A Java-Based Graphical User Interface for the R Package TIMP. *J. Stat. Soft.* **2012,** *49,* 1-22.

8. Lorenc, M.; Ziolek, M.; Naskrecki, R.; Karolczak, J.; Kubicki, J.; Maciejewski, A. Artifacts in Femtosecond Transient Absorption Spectroscopy. *Appl. Phys. B* **2002,** *74,* 19-27.

9. Michl, J.; Bonacic-Koutecky, V. *Electronic Aspects of Organic Photochemistry;* John Wiley & Sons, Inc.: New York, 1990.

10. do Casal, M. T.; Toldo, J. M.; Barbatti, M.; Plasser, F. Classification of Doubly Excited Molecular Electronic States. *Chem. Sci.* **2023,** *14,* 4012-4026.

11. Schulten, K.; Karplus, M. On the Origin of a Low-Lying Forbidden Transition in Polyenes and Related Molecules. *Chem. Phys. Lett.* **1972,** *14,* 305-309.

12. Roos, B. O.; Andersson, K.; Fulsher, M. P. Towards an Accurate Molecular Theory for Excited States: The Benzene Model. *Chem. Phys. Lett.* **1992,** *192,* 5-13.

13. Michl, J. The Role of Biradicaloid Geometries in Organic Photochemistry. *Photochem. Photobiol.* **1977,** *25,* 141-154.

14. Klessinger, M.; Michl, J. *Excited States and Photochemistry of Organic Molecules;* VCH Publishers, Inc.: New York, 1995.

15. Caldwell, R. A.; Creed, D. Exciplex Intermediates in [2 + 2] Photocycloadditions. *Acc. Chem. Res.* **1980,** *13,* 45-50.

16. Charlton, J. L.; Dabestani, R.; Saltiel, J. Role of Triplet-Triplet Annihilation in Anthracene Dimerization. *J. Am. Chem. Soc.* **1983,** *105,* 3473-3476.

17. Smith, M. B.; Michl, J. Singlet Fission. *Chem. Rev.* **2010,** *110,* 6891-6936.

18. Gilligan, A. T.; Miller, E. G.; Samakia, T.; Danrauer, N. H. Using Structurally Well-Defined Norbornyl-Bridged Acene Dimers to Map a Mechanistic Landscape for Correlated Triplet Formation in Singlet Fission. *J. Am. Chem. Soc.* **2019,** *141,* 5961-5971.

CHAPTER 5

Conclusion

We have explored the potential of using solvent based deposition of K_x:*p*-terphenyl. Initial methods with tetrahydrofuran as the solvent had little control over the specific doping stoichiometry. The scale of the reaction was also inherently limited because it used optical spectroscopy to assess its progress. Additionally, it appeared to produce a material with a distinct potassium metal phase. This motivated us to work with liquid ammonia, a solvent that can dissolve potassium directly without the use of a potassium mirror. It also motivated developing new techniques for performing other physical characterization such as conductivity measurements and powder x-ray diffraction.

After a considerable amount of work with liquid ammonia, a procedure was developed that reproducibly synthesizes films of K_x:*p*-terphenyl. Spectroscopic characterization of this material suggests that at low doping levels, a considerable amount of neutral *p*-terphenyl remains. The dianion appears to be the dominant anion that forms in the film. Neutral *p*-terphenyl persists until 3 molar equivalents of potassium are used for the reaction. Degradation of K_x:*p*-terphenyl does not appear result in the reformation of *p*-terphenyl, contrary to what is assumed in the literature.

XRD analysis of the material is complicated by the difficulty of the measurement and complexity of the material. Quantitative modelling of the diffraction patterns is ongoing. Conductivity measurements of a $K_{2.5}$:*p*-terphenyl

film as a function of temperature shows a linear trend atypical of semiconducting materials. These results show that this technique is a promising method for producing K_x:*p*-terphenyl materials for superconductivity. Now that this method has been established, effort can be made to improve the crystallinity of the material by controlling the reaction and deposition temperature and time. Work continues.

We have also demonstrated the sub-picosecond formation of a [2 + 2] photocycloaddition product from the second excited state. This result can be interpreted as a singlet fission like process from S_2 to the ^{1}TT doubly excited state, which is correlated with the pericyclic minimum. To explore this mechanism further, multiconfigurational quantum chemistry calculations should be performed on the reaction path.

BIBLIOGRAPHY

Chapter 1

1. Castellan, G. W. *Physical Chemistry,* 3rd Ed.; Addison-Wesley Publishing Company: Reading, MA, 1983.

2. Madelung, O. *Introduction to Solid-State Theory*, Cardona, M.; Fulde, P.; Queisser, H.-J. Eds.; Springer Series in Solid-State Sciences; Springer-Verlag: New York, 1981.

3. Hill, R. M. Variable-Range Hopping. *Phys. Stat. Sol.* **1976,** *34,* 601-613.

4. Nardes, A. M.; Kemerink, M.; Janssen, R. A. J.; Anisotropic Hopping Conduction in Spin-Coated PEDOT:PSS Thin Films. *Phys. Rev. B* **2007,** *76,* 085208.

5. Lin, T. T.; Young, S. L.; Kung, C. Y.; Chen, H. Z.; Kao, M. C.; Chang, M. C.; Ou, C. R. Variable-Range Hopping and Thermal Activation Conduction of Y-Doped ZnO Nanocrystalline Films. *IEEE TNANO.* **2014,** *13,* 425-430.

6. Annett, J. F. *Superconductivity, Superfluids, and Condensates*, Oxford Master Series in Condensed Matter Physics; Oxford University Press: New York, 2004.

7. Tinkham, M. *Introduction to Superconductivity,* 2nd Ed.; International Series in Pure and Applied Physics; McGraw-Hill, Inc.: New York, 1996.

8. Kittel, C. *Introduction to Solid State Physics*, 5th Ed. John Wiley & Sons, Inc.: New York, 1976.

9. Onnes, H. K. Further Experiments with Liquid Helium C. On the Change of Electric Resistance of Pure Metals at Very Low Temperatures etc. IV. The

Resistance of Pure Mercury at Helium Temperatures. *Proceedings,* **1911,** *13,* 1274-1276.

10. Bednorz, J. G.; Muller, K. A. Possible High T_c Superconductivity in the Ba-La-Cu-O System. *Z. Phys. B – Condensed Matter* **1986,** *64,* 189-193.

11. Little, W. A. Possibility of Synthesizing an Organic Superconductor. *Phys. Rev.* **1964,** *134,* A1416-A1424.

12. Jerome, D.; Mazaud, A.; Ribault, M. Superconductivity in a Synthetic Organic Conductor $(TMTSF)_2PF_6$. *J. Physique – LETTRES* **1980,** *41,* L-95-L-98.

13. Xiang, X.-D.; Hou, J. G.; Briceno, G.; Vareka, W. A.; Mostovoy, R.; Zettl, A.; Crespi, V. H.; Cohen, M. L. Synthesis and Electrical Transport of Sing Crystal K_3C_{60}. *Science* **1992,** *256,* 1190-1191.

14. Hebard, A. F. Superconductivity in Doped Fullerenes. *Phys. Today* **1992,** *45,* 26-32.

15. Emery, N.; Herold, C.; d'Astuto, M.; Garcia, V.;Bellin, Ch.; Mareche, J. F.; Lagrange, P.; Loupias, G. Superconductivity in Bulk CaC_6. *Phys. Rev. Lett.* **2005,** *95,* 087003.

16. Mitsuhashi, R.; Suzuki, Y.; Yamanari, Y.; Mitamura, H.; Kambe, T.; Ikeda, N.; Okamoto, H.; Fujiwara, A.; Yamaji, M.; Kawasaki, N.; Maniwa, Y.; Kubozono, Y. Superconductivity in Alkali-Metal-Doped Picene. *Nat. Lett.* **2010,** *464,* 76-79.

17. Wang, R.-S.; Gao, Y.; Huang, Z.-B.; Chen, X.-J. Superconductivity Above 120 Kelvin in a Chain Link Molecule. arXiv:1703.06641, **2017.**

18. Wang, R.-S.; Gao, Y.; Huang, Z.-B.; Chen, X.-J. Superconductivity in *p*-Terphenyl. arXiv:1703.05803, **2017.**

19. Wang, R.-S.; Gao, Y.; Huang, Z.-B.; Chen, X.-J. Superconductivity at 43 K in a Single C-C Bond Linked Terphenyl. arXiv:1703.05804, **2017.**

20. Li, H.; Zhou, X.; Parham, S.; Nummy, T.; Griffith, J.; Gordon, K. N.; Chronister, E. L.; Dessau, D. S. Spectroscopic Evidence of Low-Energy Gaps Persisting Up To 120 K in Surface-Doped *p*-Terphenyl Crystals. *Phys. Rev. B* **2019,** *100,* 064511.

21. Zhong, G.-H.; Wang, X.-H.; Wang, R.-S.; Han, J.-X.; Zhang, C.; Chen, X.-J.; Lin, H.-Q. Structural and Bonding Characteristics of Potassium-Doped *p*-Terphenyl Superconductors. *J. Phys. Chem. C* **2018,** *122,* 3801-3808.

22. Yan, X.-W.; Huang, Z.; Gao, M.; Zhang, C. Stable Structural Phase of Potassium-Doped *p*-Terphenyl and Its Semiconducting State. *J. Phys. Chem. C* **2018,** *122,* 27648-27655.

23. Carrera, M.; McDonald, J. L.; Untiedt, C.; Garcia-Hernandez, F. M.; Verges, J. A.; Guijarra, A. Characterization of Main Phase in K_x*p*-Terphenyl and Its Largest Congener $K_x$poly(*p*-phenylene): A Report of Their Magnetic and Electric Properties. *J. Chem. Phys. C* **2019,** *123,* 5264-5272.

24. Pinto, N.; Di Nicola, C.; Trapananti, A.; Minicucci, M.; Di Cicco, A.; Marcelli, A.; Bianconi, A.; Marchetti, F.; Pettinari, C.; Perali, A. Potassium-Doped Para-Terphenyl: Structure, Electrical Transport Properties and Possible Signatures of a Superconducting Transition. *Condens. Matter* **2020,** *5,* 78.

25. He, Q.; Marsik, P.; Le Mardele, F.; Xu, B.; Sharma, M.; Pinto, N.; Perali, A.; Di Nicola, C.; Pettinari, C.; Baeriswyl, D.; Bernhard, C. Infrared Ellipsometry Study of the Charge Dynamics in K_3*p*-Terphenyl. *Phys. Rev. B* **2023,** *107,* 094520.

26. Anslyn, E. V.; Dougherty, D. A. *Modern Physical Organic Chemistry,* University Science Books: Sausalito, CA, 2006.

27. Hoffmann, R.; Woodward, R. B. The Conservation of Orbital Symmetry. *Acc. Chem Res.* **1968,** *1,* 17-22.

28. Vollmer, J. J.; Servis, K. L. Woodward-Hoffmann Rules: Cycloaddition Reactions. *J. Chem. Ed.* **1970,** *47,* 491-500.

29. Michl, J.; Bonacic-Koutecky, V. *Electronic Aspects of Organic Photochemistry;* John Wiley & Sons, Inc.: New York, 1990.

30. Fita, P.; Luzina, E.; Dziembowska, T.; Radzewicz, Cz.; Grabowska, A. Chemistry, Photophysics, and Ultrafast Kinetics of Two Structurally Related Schiff Bases Containing the Naphthalene and Quinoline Ring. *J. Chem. Phys.* **2006,** *125,* 184508.

31. Snellenburg, J. J.; Laptenok, S. P.; Seger, R.; Mullen, K. M.; van Stokkum, I. H. M. Glotoran: A Java-Based Graphical User Interface for the R Package TIMP. *J. Stat. Soft.* **2012,** *49,* 1-22.

Chapter 2

1. Sakamoto, A.; Harada, T.; Tonegawa, N. A New Approach to the Spectral Study of Unstable Radicals and Ions in Solution by the Use of an Inert Gas

Glovebox System: Observation and Analysis of the Infrared Spectra of the Radical Anion and Dianion of *p*-Terphneyl. *J. Am. Chem. Soc.* **2008,** *112,* 1180-1187.

2. Harris, D. C.; *Quantitative Chemical Analysis,* 7th Ed.; W. H. Freeman and Company: New York, 2007.

3. Williams, D. B. G.; Lawton, M. Drying of Organic Solvents: Quantitative Evaluation of the Efficiency of Several Desiccants. *J. Org. Chem.* **2010,** *75,* 8351-8354.

4. Carrera, M.; McDonald, J. L.; Untiedt, C.; Garcia-Hernandez, F. M.; Verges, J. A.; Guijarra, A. Characterization of Main Phase in K_x*p*-Terphenyl and Its Largest Congener $K_x$poly(*p*-phenylene): A Report of Their Magnetic and Electric Properties. *J. Chem. Phys. C* **2019,** *123,* 5264-5272.

5. Pinto, N.; Di Nicola, C.; Trapananti, A.; Minicucci, M.; Di Cicco, A.; Marcelli, A.; Bianconi, A.; Marchetti, F.; Pettinari, C.; Perali, A. Potassium-Doped Para-Terphenyl: Structure, Electrical Transport Properties and Possible Signatures of a Superconducting Transition. *Condens. Matter* **2020,** *5,* 78.

6. Zhong, G.-H.; Wang, X.-H.; Wang, R.-S.; Han, J.-X.; Zhang, C.; Chen, X.-J.; Lin, H.-Q. Structural and Bonding Characteristics of Potassium-Doped *p*-Terphenyl Superconductors. *J. Phys. Chem. C* **2018,** *122,* 3801-3808.

7. Yan, X.-W.; Huang, Z.; Gao, M.; Zhang, C. Stable Structural Phase of Potassium-Doped *p*-Terphenyl and Its Semiconducting State. *J. Phys. Chem. C* **2018,** *122,* 27648-27655.

Chapter 3

1. Symons, M. C. R. Solutions of Metals: Solvated Electrons. *Chem. Soc. Rev.* **1976,** *5,* 337-358.

2. Birch, A. J. The Birch Reduction in Organic Synthesis. *Pure & Appl. Chem.* **1996,** *68,* 553-556.

3. Rabideau, P. W. The Metal-Ammonia Reduction of Aromatic Compounds. *Tetrahedron* **1989,** *45,* 1579-1603.

4. Sakamoto, A.; Harada, T.; Tonegawa, N. A New Approach to the Spectral Study of Unstable Radicals and Ions in Solution by the Use of an Inert Gas Glovebox System: Observation and Analysis of the Infrared Spectra of the Radical Anion and Dianion of *p*-Terphneyl. *J. Am. Chem. Soc.* **2008,** *112,* 1180-1187.

5. Carrera, M.; McDonald, J. L.; Untiedt, C.; Garcia-Hernandez, F. M.; Verges, J. A.; Guijarra, A. Characterization of Main Phase in K_x*p*-Terphenyl and Its Largest Congener $K_x$poly(*p*-phenylene): A Report of Their Magnetic and Electric Properties. *J. Chem. Phys. C* **2019,** *123,* 5264-5272.

6. Pinto, N.; Di Nicola, C.; Trapananti, A.; Minicucci, M.; Di Cicco, A.; Marcelli, A.; Bianconi, A.; Marchetti, F.; Pettinari, C.; Perali, A. Potassium-Doped Para-Terphenyl: Structure, Electrical Transport Properties and Possible Signatures of a Superconducting Transition. *Condens. Matter* **2020,** *5,* 78.

7. Peres, L. O.; Spiesser, M.; Froyer, G. Reduction of *p*-Terphenyl, *p*-Quaterphenyl and *p*-Sexiphenyl Using Alkali Metal in Liquid Ammonia: Process and Characterization of the Reduced Compounds. *Synth. Met.* **2005,** *155,* 450-454.

8. Shriver, D. F.; Drezdzon, M. A. *The Manipulation of Air-Sensitive Compounds,* 2nd Ed; John Wiley & Sons: New York, 1986.

9. Neese, F. The ORCA Program System. *Wiley Interdiscip. Rev.: Comput. Mol. Sci.* **2012,** *2,* 73-78.

10. Bremond, E.; Savarese, M.; Su, N. Q.; Perez-Jiminez, A. J.; Xu, X.; Sancho-Garcia, J. C.; Adamo, C. Benchmarking Density Functionals on Structural Parameters of Small-/Medium-Sized Organic Molecules. *J. Chem. Theory Comput.* **2016,** *12,* 459-465.

11. Urban, M. W. *Attenuated Total Reflectance Spectroscopy of Polymers: Theory and Practice,* Polymer Surfaces and Interface Series; American Chemical Society: Washington, DC, 1996.

12. Fox, M. *Optical Properties of Solids,* 2nd Ed.; Oxford Master Series in Condensed Matter Physics; Oxford University Press: New York, 2010.

13. Rice, A. P.; Tham, F. S.; Chronister, E. L. A Temperature Dependent X-ray Study of the Order-Disorder Enantiotropic Phase Transition of *p*-Terphenyl. *J. Chem. Crystallogr.* **2013,** *43,* 14-25.

14. Nardes, A. M.; Kemerink, M.; Janssen, R. A. J.; Anisotropic Hopping Conduction in Spin-Coated PEDOT:PSS Thin Films. *Phys. Rev. B* **2007,** *76,* 085208

Chapter 4

1. Tonne, J. The Mechanism of an Unusual Benzo/Benzo Photocycloaddition Reaction. Ph.D. Thesis, Albert Ludwig University of Freiburg, Germany, 2001.

2. Tonne, J.; Prinzback, H.; Michl, J. Double Actinometry for Rigorous Evaluation of Quantum Yields of Clean Photoreversible Photochemical Reactions. *Photochem. Photobiol. Sci.* **2002,** *1,* 105-110.

3. Megerle, U.; Pugliesi, I.; Schriever, C.; Sailer, C. F.; Riedle, E. Sub-50 fs Broadband Absorption Spectroscopy with Tunable Excitation: Putting the Analysis of Ultrafast Molecular Dynamics on Solid Ground. *Appl. Phys. B* **2009,** *96,* 215-231.

4. Riedle, E.; Beutter, M.; Lochbrunner, S.; Piel, J.; Schenkl, S.; Sporlein, S.; Zinth, W. Generation of 10 to 50 fs Pulses Tunable Through All of the Visible and NIR. *Appl. Phys. B* **2000,** *71,* 457-465.

5. Homann, C.; Krebs, N.; Riedle, E. Convenient Pulse Length Measurement of Sub-20-fs Pulses Down to the Deep UV via Two-Photon Absorption in Bulk Material. *Appl. Phys. B* **2011,** *104,* 783.791.

6. Bradler, M.; Riedle, E. Temporal and Spectral Correlations in Bulk Continua and Improved Use in Transient Spectroscopy. *J. Opt. Soc. Am. B* **2014,** *31,* 1465-1475.

7. Snellenburg, J. J.; Laptenok, S. P.; Seger, R.; Mullen, K. M.; van Stokkum, I. H. M. Glotoran: A Java-Based Graphical User Interface for the R Package TIMP. *J. Stat. Soft.* **2012,** *49,* 1-22.

8. Lorenc, M.; Ziolek, M.; Naskrecki, R.; Karolczak, J.; Kubicki, J.; Maciejewski, A. Artifacts in Femtosecond Transient Absorption Spectroscopy. *Appl. Phys. B* **2002,** *74,* 19-27.

9. Michl, J.; Bonacic-Koutecky, V. *Electronic Aspects of Organic Photochemistry;* John Wiley & Sons, Inc.: New York, 1990.

10. do Casal, M. T.; Toldo, J. M.; Barbatti, M.; Plasser, F. Classification of Doubly Excited Molecular Electronic States. *Chem. Sci.* **2023,** *14,* 4012-4026.

11. Schulten, K.; Karplus, M. On the Origin of a Low-Lying Forbidden Transition in Polyenes and Related Molecules. *Chem. Phys. Lett.* **1972,** *14,* 305-309.

12. Roos, B. O.; Andersson, K.; Fulsher, M. P. Towards an Accurate Molecular Theory for Excited States: The Benzene Model. *Chem. Phys. Lett.* **1992,** *192,* 5-13.

13. Michl, J. The Role of Biradicaloid Geometries in Organic Photochemistry. *Photochem. Photobiol.* **1977,** *25,* 141-154.

14. Klessinger, M.; Michl, J. *Excited States and Photochemistry of Organic Molecules;* VCH Publishers, Inc.: New York, 1995.

15. Caldwell, R. A.; Creed, D. Exciplex Intermediates in [2 + 2] Photocycloadditions. *Acc. Chem. Res.* **1980,** *13,* 45-50.

16. Charlton, J. L.; Dabestani, R.; Saltiel, J. Role of Triplet-Triplet Annihilation in Anthracene Dimerization. *J. Am. Chem. Soc.* **1983,** *105,* 3473-3476.

17. Smith, M. B.; Michl, J. Singlet Fission. *Chem. Rev.* **2010,** *110,* 6891-6936.

18. Gilligan, A. T.; Miller, E. G.; Samakia, T.; Danrauer, N. H. Using Structurally Well-Defined Norbornyl-Bridged Acene Dimers to Map a Mechanistic Landscape for Correlated Triplet Formation in Singlet Fission. *J. Am. Chem. Soc.* **2019,** *141,* 5961-5971.